



Goldberg, Graham Robert (2021) *Spectral bandwidth enhancement in gallium nitride superluminescent light emitting diodes*. PhD thesis.

<http://theses.gla.ac.uk/82076/>

Copyright and moral rights for this work are retained by the author

A copy can be downloaded for personal non-commercial research or study, without prior permission or charge

This work cannot be reproduced or quoted extensively from without first obtaining permission in writing from the author

The content must not be changed in any way or sold commercially in any format or medium without the formal permission of the author

When referring to this work, full bibliographic details including the author, title, awarding institution and date of the thesis must be given

Enlighten: Theses
<https://theses.gla.ac.uk/>
research-enlighten@glasgow.ac.uk

Spectral Bandwidth Enhancement in Gallium Nitride Superluminescent Light Emitting Diodes

Graham Robert Goldberg



University of Glasgow

**Submitted in fulfilment of the requirements for the
Degree of Doctor of Philosophy to the Electronics
and Nanoscale Engineering Department, School of
Engineering, University of Glasgow**

**Supervisor: Professor Richard Hogg
Second Supervisor: Doctor David Childs**

March 2021

Abstract

This thesis is concerned with the design and development of short wavelength, $\sim 400\text{nm}$, superluminescent light emitting diodes (SLEDs). The enhancement of spectral bandwidth through the use of multiple passive and active contacts allows the spectral bandwidth to be increased beyond that possible with a single active contact. Such devices may find application in biomedical imaging applications such as optical coherence tomography (OCT). Thus far limited research has been conducted into short wavelength devices for OCT due to immaturity of development of suitable materials and their associated narrow bandwidths. Prior to this work gallium nitride (GaN) SLEDs have been reported with bandwidths of $\sim 5\text{nm}$, which at 400nm offers an axial resolution in the region of $10\mu\text{m}$. This thesis describes and explains the research conducted towards the objective of achieving broader bandwidth.

Initially, an experimental setup capable of characterising shorter wavelength devices was constructed, and a comprehensive review of the literature and current state of the art is presented. An OCT setup was then constructed, allowing for direct measurement of device resolution and comparison to values obtained using both the point spread function and from theory. Non-contact metrology using a GaN SLED was then carried out for the first time. For a two contact SLED the role of bias conditions and their effect on the absorber section and device emission bandwidth was then examined, after which three section GaN SLEDs were developed, allowing for different current injection levels to be applied to the active regions. Optimal drive conditions for the two active contacts, along with a short-circuited absorber section, allowed a spectral bandwidth of $\sim 20\text{nm}$ to be obtained. Device resolution was again analysed under the new conditions, yielding $3.3\mu\text{m}$, and compared to the Rayleigh criterion. This offered a system resolution limit value. Once successfully developed, short wavelength GaN SLEDs with a broad bandwidth could sufficiently increase axial resolution to allow detailed imaging of the cornea and its respective layers, early detection of skin cancers, and imaging teeth in non-ionising dental applications. Future routes to developing even broader bandwidth devices, and hence higher resolution sources, are discussed.

Contents

Abstract	iii
Acknowledgements	vi
List of Publications	vii
List of Figures	ix
Author's Declaration	xii
Chapter One – Introduction and Background	1
1.1 Introduction to Thesis	1
1.1.1 Overview of Thesis	1
1.1.2 Summary of Thesis	1
1.2 Outline of Chapters	3
1.2.1 Outline of Chapter One	3
1.2.2 Outline of Chapter Two	4
1.2.3 Outline of Chapter Three	4
1.2.4 Outline of Chapter Four	5
1.2.5 Outline of Chapter Five	5
1.3 Background	6
1.4 Conventional Superluminescent Light Emitting Diodes	10
1.5 Optical Coherence Tomography	11
1.6 Resolution	13
1.7 Short Wavelength Applications	17
1.8 Short Wavelength Diode Lasers – Gallium Nitride	19
1.9 Gallium Nitride SLEDs	26
1.10 Gaps in Knowledge	27
References	28
Chapter Two – FIB Modified Commercial Laser Diodes: Concept Proof	38
2.1 Introduction to Chapter	38
2.2 Outline of Chapter	39
2.3 Design of Experimental Setup	40
2.4 Characterisation of Commercial GaN Laser Diodes	43
2.5 Commercial GaN Laser Diode Contact Segmentation	46

2.6 Point Spread Function	51
2.7 Optical Coherence Tomography	53
2.8 Summary	57
2.9 Further Work	58
References	59
Chapter Three – The Effect of Absorbers on GaN SLED Performance	67
3.1 Introduction to Chapter	67
3.2 Outline of Chapter	68
3.3 Fabrication Steps for Gallium Nitride SLEDs	69
3.4 Characterisation of Fabricated GaN Laser Diodes	87
3.5 Post FIB Modification	92
3.6 Open-Circuit GaN SLED	96
3.7 Short-Circuit GaN SLED	99
3.8 Point Spread Function	103
3.9 Summary	106
3.10 Further Work	106
References	108
Chapter Four – Multi-Contact GaN SLEDs for Bandwidth Enhancement	111
4.1 Introduction to Chapter	111
4.2 Outline of Chapter	113
4.3 Multi-Section GaN SLED	114
4.4 Open-Circuit Multi-Section GaN SLED	116
4.5 Short-Circuit Multi-Section GaN SLED	117
4.6 Bandwidth Discussion	118
4.7 Varying Current in Sections	120
4.8 Rayleigh Criterion	124
4.9 Summary	125
4.10 Further Work	126
References	128
Chapter Five – Summary and Future Work	133
5.1 Summary	133
5.2 Further Work	135
References	137

Acknowledgements

This thesis is dedicated to the memory of Hannah Monchar, Norma Sneed and Doreen Jones, without whom this would not have been possible.

I would first like to extend my deepest thanks and appreciation to Professor Richard Hogg for both giving me the opportunity to pursue a Ph.D., and your patience and support while I completed it. David Childs, Pavlo Ivanov, Nasser Babazadeh, Nobuhiko Ozaki, and Kenneth Kennedy, I am very grateful for your guidance and meaningful insights on everything from semiconductor theory to device fabrication and characterisation techniques.

Additionally, I would like to thank my colleagues and fellow researchers, who were always willing to take the time to have a discussion with me about my work, offer your opinions and advice on the approach I was taking, even if it was not so relatable to your own research. In particular, thanks go to Richard Taylor, Justin Sperling, Sarah Henry, Iain Butler and Soroush Sobhani. I would also like to thank Jeevan Mehat and Scott Cummings for their thoughts, Niall Ullah and Conor Boyle for our conversations on the trains to and from Edinburgh, as well as David Macdonald and David Reeves for your assistance with my data.

To my family, especially my parents Mike and Nicky, brother Peter, and Grandma Zena, I would like to thank you for always being there for me, raising me and generating the interest I have in further learning. Your unwavering belief that I would achieve this qualification helped to keep me motivated on the days when I was not so sure. Finally, to my girlfriend Carol Mackillop, for your understanding and all of your encouragement over the years and long hours, thank you.

"Let no feeling of discouragement prey upon you, and in the end you are sure to succeed." – Abraham Lincoln

List of Publications

Journal Papers

Graham R. Goldberg, Aleksandr Boldin, Sophia M. L. Andersson, Pavlo Ivanov, Nobuhiko Ozaki, Richard J. E. Taylor, David T. D. Childs, Kristian M. Groom, Kenneth L. Kennedy and Richard A. Hogg, "Gallium Nitride Superluminescent Light Emitting Diodes for Optical Coherence Tomography Applications," in IEEE Journal of Selected Topics in Quantum Electronics, Vol. 23, No. 6, pp. 1-11, Article No. 2000511, November 2017.

Graham R. Goldberg, Dae-Hyun Kim, Richard J. E. Taylor, David T. D. Childs, Pavlo Ivanov, Nobuhiko Ozaki, Kenneth L. Kennedy, Kristian M. Groom, Yukihiro Harada and Richard A. Hogg, "Bandwidth Enhancement in an InGaN/GaN Three-section Superluminescent Diode for Optical Coherence Tomography", Applied Physics Letters, Volume 117, Issue 6, August 2020.

Conference Proceedings

Graham R. Goldberg, Pavlo Ivanov, Nobuhiko Ozaki, David T. D. Childs, Kristian M. Groom, Kenneth L. Kennedy, and Richard A. Hogg "Gallium Nitride Light Sources for Optical Coherence Tomography", Proceedings of SPIE 10104, Gallium Nitride Materials and Devices XII, 101041X, February 2017.

Conference Posters

Graham R. Goldberg, Pavlo Ivanov, Nobuhiko Ozaki, David T. D. Childs, Kristian M. Groom, Kenneth L. Kennedy, and Richard A. Hogg, “Gallium Nitride Super-Luminescent Light Emitting Diodes for Optical Coherence Tomography Applications”, International Semiconductor Laser Conference (ISLC), Kobe, Japan, 12-15 September 2016, ISBN 9784885523069.

List of Figures

Chapter One – Introduction and Background

Figure 1-1 Photons and charge carrier interactions	6
Figure 1-2 P-i-N diode and associated band structure	7
Figure 1-3 A laser resonant cavity showing facet reflections	8
Figure 1-4 Schematics of methods to reduce feedback in lasers	9
Figure 1-5 Schematic of a time domain optical coherence tomography setup	12
Figure 1-6 Schematic of a Fourier domain optical coherence tomography setup	13
Figure 1-7 Predicted values of axial and lateral resolution	14
Figure 1-8 Eye cross-section showing component parts and transmission	15
Figure 1-9 Ray diagrams of spectrophotometer and spectroreflectometer	16
Figure 1-10 Transmittance for cornea and lens varying wavelength	17
Figure 1-11 OCT image of the cornea highlighting the layer structure	18
Figure 1-12 Schematic diagram of a Mg-doped MIS GaN diode	21
Figure 1-13 Cross-sectional diagram of GaN with an AlN buffer layer	22
Figure 1-14 Cross-section of GaN double heterostructure LED and laser	24
Figure 1-15 Schematic diagram of GaN SLED and 200mW GaN SLED	27

Chapter Two

Figure 2-1 Emission spectra experimental setup schematic and ray diagram	41
Figure 2-2 SEM images of one of the commercial laser diodes	43
Figure 2-3 GaN laser diode characterisation at low current densities	44
Figure 2-4 GaN laser diode characterisation at high current densities	45
Figure 2-5 Focused ion beam schematic and magnified view	47
Figure 2-6 SEM images of GaN SLEDs during the FIB milling process	48
Figure 2-7 SEM images of commercial laser diode following segmentation	49
Figure 2-8 GaN laser diode characterisation following segmentation	49
Figure 2-9 GaN laser diode FWHM and predicted axial resolution	50
Figure 2-10 GaN laser diode PSF and predicted axial resolution	51
Figure 2-11 GaN laser diode predicted axial resolution alternate equation	52
Figure 2-12 OCT experimental setup schematic and ray diagram	54

Figure 2-13 Interferograms for various current densities	56
Figure 2-14 Metrology of a glass microscope slide	57
Chapter Three	
Figure 3-1 GaN wafer following cleave and clean	71
Figure 3-2 Following deposition of BPRS 200	72
Figure 3-3 Following development of BPRS 200	73
Figure 3-4 Following deposition of Ni and Au	74
Figure 3-5 Following removal of photoresist	75
Figure 3-6 Following deposition of SiO ₂	76
Figure 3-7 Following deposition of SPR 350	77
Figure 3-8 Following development of SPR 350	78
Figure 3-9 Following dry etch	79
Figure 3-10 Following removal of SPR 350 and SiO ₂	80
Figure 3-11 Following deposition of SiO ₂	81
Figure 3-12 Following deposition of BPRS 200	82
Figure 3-13 Following development of BPRS 200	83
Figure 3-14 Following dry etch	84
Figure 3-15 Following deposition of Ti, Au, and removal of BPRS 200	85
Figure 3-16 Following thinning of substrate and deposition of Ti and Au	86
Figure 3-17 SEM images of several of the fabricated GaN laser diodes	87
Figure 3-18 5µm GaN SLED characterisation	89
Figure 3-19 10µm GaN laser diode characterisation	90
Figure 3-20 15µm GaN laser diode characterisation	91
Figure 3-21 5µm GaN SLED characterisation following 1 st segmentation	93
Figure 3-22 10µm GaN SLED characterisation following 1 st segmentation	95
Figure 3-23 5µm GaN SLED characterisation rear O/C	96
Figure 3-24 10µm GaN SLED characterisation rear O/C	97
Figure 3-25 GaN SLEDs FWHM both and rear O/C	98
Figure 3-26 5µm GaN SLED characterisation rear S/C	99
Figure 3-27 10µm GaN SLED characterisation rear S/C	100
Figure 3-28 GaN SLEDs FWHM both, rear O/C, rear S/C	101
Figure 3-29 GaN SLEDs λ_0 both, rear O/C, rear S/C	102
Figure 3-30 GaN SLEDs PSF rear O/C, rear S/C	103
Figure 3-31 5µm GaN SLED PSF and axial resolution rear O/C, rear S/C	105

Chapter Four

Figure 4-1 Schematic diagram and emission spectra of a GaAs SLED	112
Figure 4-2 Schematic band diagrams of InGaN/GaN-based QWs	113
Figure 4-3 5 μ m GaN SLED characterisation following 2 nd segmentation	115
Figure 4-4 5 μ m GaN SLED characterisation rear O/C	116
Figure 4-5 5 μ m GaN SLED characterisation rear S/C	118
Figure 4-6 5 μ m GaN SLED FWHM and λ_0 front 1/3, rear O/C, rear S/C	119
Figure 4-7 5 μ m GaN SLED characterisation sharing 4J rear O/C	121
Figure 4-8 5 μ m GaN SLED characterisation varying 'b' rear O/C	122
Figure 4-9 5 μ m GaN SLED characterisation varying 'b' rear S/C	123
Figure 4-10 5 μ m GaN SLED PSF and Rayleigh criterion	124

Author's Declaration

I declare that, except where explicit reference is made to the contribution of others, this thesis is the result of my own work and has not been submitted for any other degree at the University of Glasgow or any other institution.

Chapter One - Introduction and Background

1.1 Introduction to Thesis

1.1.1 Overview of Thesis

This thesis is concerned with the design and development of short wavelength, $\sim 400\text{nm}$, superluminescent light emitting diodes (SLEDs) for biomedical imaging applications such as optical coherence tomography (OCT) [01-08]. Short wavelengths are desirable because the axial resolution is proportional to the wavelength squared, increasing significantly as the wavelength decreases. Thus far limited research has been conducted into short wavelength devices for OCT due to immaturity of development of suitable materials like gallium nitride (GaN) and their associated narrow bandwidths. As axial resolution is inversely proportional to bandwidth, to increase the resolution, steps must be taken to increase the bandwidth. A short wavelength GaN SLED with a broad bandwidth could sufficiently increase the axial resolution to allow detailed imaging of the cornea and its respective layers [09-11].

1.1.2 Summary of Thesis

A typical semiconductor laser [12,13] features a resonant cavity formed by creating a waveguide along the length of the device. This is terminated at both ends by flat, mirror-like, facets perpendicular to the waveguide and parallel to one another. Injected current generates photons of light that are confined within the waveguide yet able to propagate along its length, generating further photons through stimulated emission. When these photons are incident on one of the facets a large percentage are reflected and propagate in the opposite direction back along the waveguide. This is termed optical feedback and causes the

production of a series of standing waves, or modes, with their wavelengths determined by the length of the resonant cavity as well as the bandgap of the material. As the losses of the device are overcome and lasing occurs, one or more of the modes become dominant and a narrow spectral bandwidth lasing peak is observed, which is orders of magnitude larger than adjacent modes. SLEDs [14-19] are laser devices where the feedback has been reduced enough to inhibit lasing, or remove it altogether. This means that photons generated inside the waveguide propagate along its length generating further photons through stimulated emission, as with the typical semiconductor laser described above. However, when these photons are incident on one of the facets, they are, ideally, all emitted from the device instead of being reflected in the opposite direction back along the waveguide. Gain in a SLED is achieved from this single pass through the waveguide. Feedback can be reduced by employing one or more techniques [20-28]. It is common to see several of these methods utilised in a typical SLED to maintain a broad bandwidth, while achieving the directionality and high powers observed in typical lasers.

Prior to this work GaN SLEDs [29-36] have been reported with bandwidths of $\sim 5\text{nm}$, which at 400nm offers an axial resolution of $10\mu\text{m}$. To achieve a similar resolution with conventional OCT light sources of $800\text{-}1300\text{nm}$, bandwidths of between $25\text{-}100\text{nm}$ would be required depending on the emission wavelength chosen. As some layers of the cornea are less than $10\mu\text{m}$ thick [11], at least $1\mu\text{m}$ axial resolution would be required to image these layers using OCT. Although 150nm bandwidths at 890nm have been reported by Cucu *et al.*, [37] resolution was $3\mu\text{m}$ and bandwidth would need to increase to 400nm to offer sub- $1\mu\text{m}$ axial resolution. For 400nm wavelengths, $3\mu\text{m}$ resolution is achieved with $\sim 20\text{nm}$ bandwidth and sub- $1\mu\text{m}$ resolution is achieved at 50nm bandwidth, demonstrating a clear advantage in lowering the central wavelength and researching methods to increase the bandwidth.

This thesis describes and explains the research conducted towards the objective of achieving broad bandwidth emission from GaN SLEDs. Initially, an experimental setup capable of characterising shorter wavelength devices was constructed, alongside a comprehensive review of the literature and current state of the art. Commercially available laser diodes were purchased and measured against their datasheets before the feasibility of absorber sections

as methods of reducing optical feedback were explored and investigated in both these devices and those fabricated internally. An OCT setup was then constructed, allowing for direct measurement of device resolution and comparison to values obtained using both the point spread function and from theory. Metrology using a GaN SLED was then carried out for the first time. The application of bias conditions to the absorber section and their effect on emission bandwidth was then examined, after which multi-section GaN SLEDs were developed, allowing for different current injection levels to be applied to the active region. Device resolution was again analysed in the new conditions and compared to the Rayleigh criterion. An outline of the work performed in each chapter is described below.

1.2 Outline of Chapters

1.2.1 Outline of Chapter One

Section 1.3 introduces the theory behind semiconductor lasers, illustrating and explaining the three main radiative processes that can take place and what must be overcome for lasing to occur. Section 1.4 describes conventional SLEDs and highlights the differences between their structure and that of typical semiconductor lasers. Section 1.5 provides an in-depth introduction to OCT, outlining the different methods of performing the measurement and examining the advantages and disadvantages of each. The equation for system resolution in terms of source wavelength and bandwidth is then disclosed in section 1.6, further expanding on the current state of the art and analysing the transmittance of core components of the eye, before discussing the structure of the cornea in section 1.7.

The history and development of GaN devices is covered at length in section 1.8, describing how various obstacles to their development were overcome and their mass production was enabled. Finally, the progress so far in GaN SLEDs and their current figures of merit are disclosed in section 1.9. This links to section 1.5 by showing the existing device technology and the needed improvements before a short wavelength device would be suitable for OCT.

Finally, section 1.10 outlines and highlights relevant gaps in knowledge focused on during this research.

1.2.2 Outline of Chapter Two

Section 2.3 describes the experimental setup and examines its suitability for conducting short wavelength measurements. Section 2.4 characterises several commercially available 405nm GaN laser diodes, demonstrating their performance below, approaching, and above lasing threshold, highlighting the uniformity of key parameters, and agreeing the results with device datasheets. Section 2.5 repeats elements of the characterisation carried out in section 2.4 following the use of a focused ion beam (FIB) system to modify a number of the laser diodes to produce SLEDs, to ensure minimal damage to the devices. The differences in device behaviours are analysed, and the feasibility of an absorber section within a GaN SLED is investigated. Section 2.6 introduces the point spread function, discussing its merit as a measure of resolution, and comparing values produced using this method to those calculated using first principles and theory. Section 2.7 describes the construction and operation of an OCT experimental setup, with practical measurements of resolution obtained before the first demonstration of metrology with a GaN SLED.

This forms part of the work published in my IEEE Journal of Selected Topics in Quantum Electronics paper.

1.2.3 Outline of Chapter Three

Section 3.3 describes the fabrication process performed to produce the GaN laser diodes and SLEDs from a 2 quantum well (QW) GaN substrate. Section 3.4 characterises a number of GaN laser diodes fabricated internally, with similar lengths but varying ridge widths. Section 3.5 repeats elements of the characterisation carried out in section 3.4 following the use of a

FIB system to modify a number of the laser diodes to produce SLEDs, to ensure minimal damage to the devices. Section 3.6 examines the case when the absorber section of the SLED is operated in open-circuit, and section 3.7 when it is operated in short-circuit. Section 3.8 reintroduces the point spread function and discusses the resolution of the devices.

This forms part of the work published in my IEEE Journal of Selected Topics in Quantum Electronics paper.

1.2.4 Outline of Chapter Four

Section 4.3 characterises of the 5 μ m GaN SLED after the use of a FIB system to modify the device to produce three sections, with the front 1/3 is active and the rear 2/3 open-circuit. Section 4.4 repeats elements of the characterisation carried out in section 4.3 with the front 2/3 driven and the rear 1/3 open-circuit. Section 4.5 repeats elements of the characterisation carried out in sections 4.3 and 4.4 with the front 2/3 driven and the rear 1/3 short-circuit. Section 4.6 investigates the effect each case has on the central wavelength of the emission spectra and the associated bandwidth. Section 4.7 examines the effect varying the current density to each section has on the SLED bandwidth. Section 4.8 introduces the Rayleigh criterion and discusses the resolution limit of the SLED tested.

This work forms the work published in my Applied Physics Letter.

1.2.5 Outline of Chapter Five

Section 5.1 summarises the findings from Chapters Three and Four. Section 5.2 discusses proposed further works that are apparent following these findings.

1.3 Background

Absorption, spontaneous emission, and stimulated emission are radiative processes that take place between photons and charge carriers and are depicted in Figures 1-1a), b), and c), respectively. In a semiconductor with energy levels E_V and E_C , where E_V is the valence band and E_C is the conduction band, photons of energy $E_C - E_V$ can be absorbed or emitted, where $E = h\nu$, with h being Planck's constant and ν the frequency of the photon [12].

In Figure 1-1a) a photon of energy $E_C - E_V$ is absorbed by the material, promoting an electron from the valence band to the conduction band, leaving a hole in the valence band. This transition is called absorption or stimulated absorption. Due to the instability of the electron in an excited state, at some time later the electron de-excites, returning to the valence band and emitting a photon of energy $E_C - E_V$ with random phase and direction. This process is termed spontaneous emission and is shown in Figure 1-1b). In the event the electron is already in an excited state when the passing photon is incident on the material, as illustrated in Figure 1-1c), the photon's interaction can stimulate the electron to return to the valence band and emit another photon of energy $E_C - E_V$, with the same phase and direction as the incident photon. This is called stimulated emission. For this to become the dominant form of emission, as in light amplification by stimulated emission of radiation devices; it requires more than 50% of the carriers to be present in the conduction band than the valence band, assuming no internal loss, a condition known as population inversion [12,13].

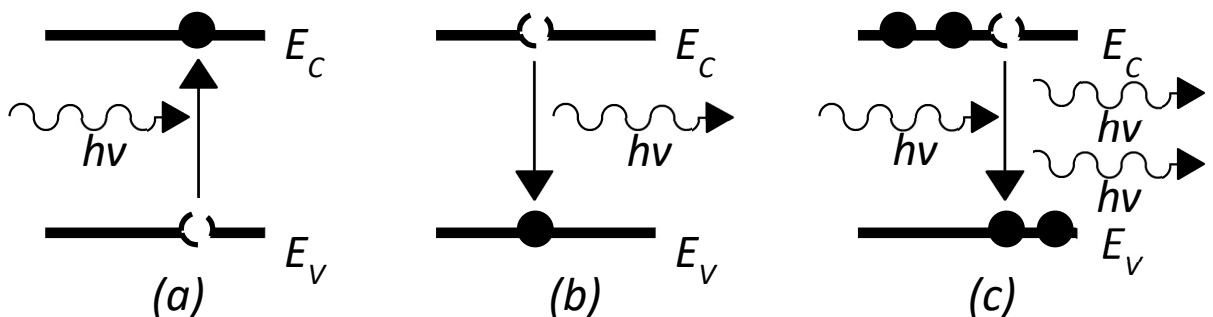


Figure 1-1 Photons and charge carrier interactions showing a) absorption b) spontaneous emission and c) stimulated emission - dots are electrons and circles are holes

Consider a basic p-i-n diode such as the one shown schematically in Figure 1-2. When a forward voltage is applied across the device, electrons and holes flow in to the intrinsic, or active, region from the n and p regions, respectively. Here the electrons and holes recombine, producing photons through spontaneous emission, the primary mechanism of light radiation found in light emitting diodes (LEDs). The current flowing through the device ensures a constant supply of carriers for recombination. Although the primary mechanism of light radiation in lasers is stimulated emission, it is not enough to simply achieve population inversion, optical feedback must be incorporated to produce a large photon density, as a mechanism for the gain stimulated emission produces to overcome any losses.

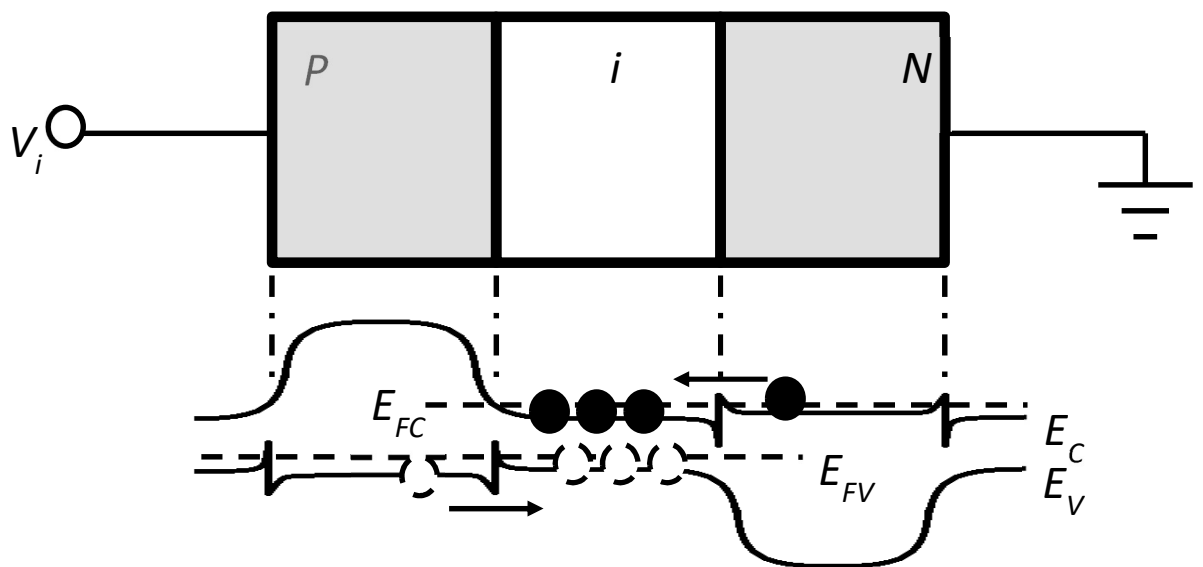


Figure 1-2 P-i-N diode and associated band structure

One way of establishing optical feedback in the above device would be to create a resonant cavity by cleaving facets. When photons are incident on one of the facets a large percentage are reflected and propagate in the opposite direction back along the waveguide. This is quite typical for semiconductor lasers, as the refractive index between the crystal and air results in around 15-35% reflection, meaning they act as mirrors. In addition, the difference in bandgap between the intrinsic region and the p and n cladding forms a waveguide along the length of the device. Figure 1-3 depicts the p-i-n diode from Figure 1-2 with the inclusion of cleaved facets, R_1 and R_2 .

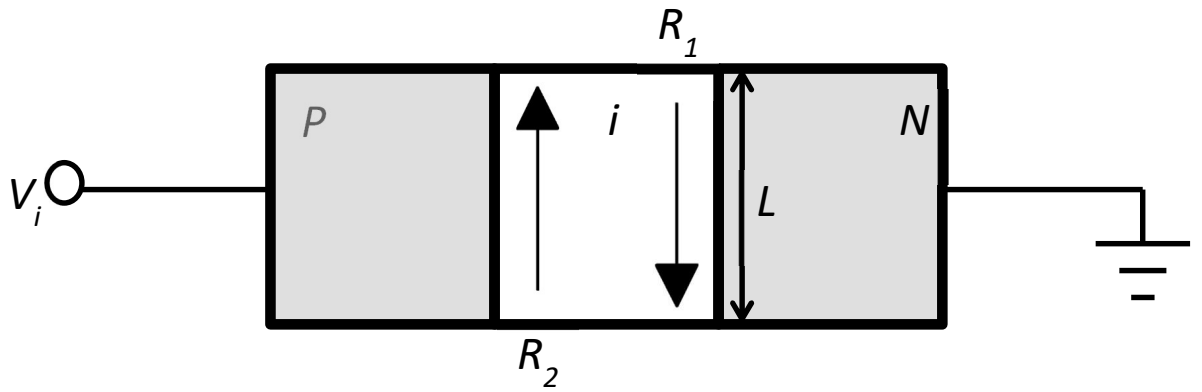


Figure 1-3 A laser resonant cavity showing facet reflections

To achieve lasing, the gain must be greater than the external, or mirror, loss and the internal loss from absorption and scattering, *etc.* The threshold gain coefficient, g_{th} , can be calculated by considering the above resonant cavity, length L , and facets with reflectivities R_1 and R_2 . At the lasing threshold, the gain equals loss, giving Equation 1-1, with α being the absorption, or loss, coefficient [12]:

$$g_{th} = \alpha_i + \alpha_m = \alpha_i + \frac{1}{2L} \ln \frac{1}{R_1 R_2} \quad \text{Equation 1-1}$$

where α_i is the internal loss and α_m is the mirror loss, that together make up α the absorption coefficient. Lasers require both feedback and gain in order to lase [13]. If this feedback were to be removed, the laser becomes a SLED. SLEDs are laser devices where the feedback has been reduced enough to inhibit lasing, or removed altogether. This means that photons generated inside the waveguide propagate along its length generating further photons through stimulated emission, as with the typical laser described above. However, when these photons are incident on one of the facets, they are, ideally, all emitted from the device instead of being reflected in the opposite direction back along the waveguide. Gain in a SLED is achieved from this single pass along the waveguide.

Feedback can be reduced by employing one or more of the following techniques [20-28], illustrated in Figure 1-4a) to e):

- Apply anti-reflective coatings to one or both facets, a)
- Change the angle of one or both facets away from 90° to the waveguide, b)
- Change the angle of the waveguide away from 90° to the facets, c)
- Incorporate an absorbing section into the waveguide, d)
- Change the waveguide from straight to curved, e)

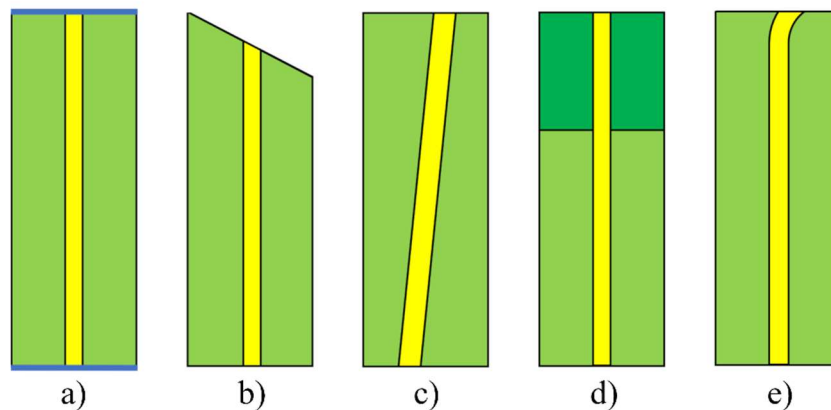


Figure 1-4 Schematics of methods to reduce feedback in lasers

Anti-reflective coatings minimise the reflectivity of the facets, maximising the likelihood that an incident photon will be emitted from the waveguide. By changing the angles of the facets or the waveguide, the reflectivity is reduced as with an anti-reflective coating, but there is an added advantage that any if any photons are reflected they are likely to escape through the sidewall and not resonate inside the cavity. If the waveguide shape is modified from a straight line to a curved, or j shape, the losses inside the waveguide are increased and the gain must reach a higher value to achieve lasing. An absorbing section is an electrically isolated but optically connected section of the waveguide, typically placed at the rear of the device. This is designed to absorb photons travelling away from the front facet and prevent them passing through the waveguide again. It is common to see several of these methods utilised in a typical SLED to offer high power, directional light beams like those observed

in lasers, coupled with incoherent, broadband emission observed in LEDs [12]. The high power, directional light beam, is due the amplified spontaneous emission (ASE) as the light passes once through the waveguide, while the lack of resonant cavity allows broadband emission light emission instead of the multi-mode or single-mode emission seen in lasers. Applications for SLEDs include OCT [01-08], fibre optic gyroscopes (FOGs) [14] and pico-projection [15]. As discussed in sections 1.4 and 1.9, this work will focus on SLEDs, examine their applications and current state of the art, before detailing the areas warranting further research. [12,16,17]. Although termed light emitting diode, SLEDs have the same epitaxial structure as an edge emitting, or in-plane, laser. This was demonstrated by Lee *et al.*, in 1973 when they produced the first SLED [18]. With no data from other SLEDs with which to compare their devices, they fabricated lasers alongside their SLEDs to allow them to characterise the material and the device behaviour.

1.4 Conventional Superluminescent Light Emitting Diodes

As introduced earlier, in order to produce high performance SLEDs, the optical feedback must be suppressed or removed. This can be achieved by tilting one or both of the facets, tilting or bending the waveguide [15], or applying an anti-reflection coating so the light escapes after a single pass through the waveguide [18,19]. The effect of increasing the magnitude of the angle of the facets relative to the waveguide was examined by Zhang *et al.*, [20]. It was demonstrated that as the angle was increased from 0° , where it is perpendicular to the waveguide, facet reflectivity decreased until the critical angle was approached, $\sim 16.8^\circ$, when the light was subject to total internal reflection. For the gallium arsenide (GaAs) devices used, 15° was found to be the optimum angle to reduce reflectivity and produce a broadband SLED. Another way to suppress optical feedback is with the incorporation of an absorber into a multi-section device [21,22]. This is designed to absorb light reflected from the front facet and prevent laser oscillation [23]. The limiting factor of these devices was shown to be that the optical output power could “burn through” the absorbing section at relatively low powers, $\sim 3\text{mW}$, resulting in lasing as oscillation was no longer suppressed [24]. This was overcome by applying an anti-reflection coating to the front facet, which increased the power before “burn through” to $\sim 14\text{mW}$, as well as by grounding

the absorber [25-27]. Connecting the absorber to ground prevented the accumulation of carriers in the absorber, thereby preventing “burn through” until powers of at least $\sim 30\text{mW}$ [28]. Combining all three of these design features to form a multi-section device with a bent waveguide, tilted facet, and an absorber section, offers the advantage of increased output powers as well as greater control over the spectral shape [21,22,27]. Such devices will be discussed in more detail in Chapter Four of this thesis.

Section 1.5 details the background and history of OCT, introducing light sources utilised, the main methods of performing the measurement, and the advantages and disadvantages of each. Current wavelengths utilised by OCT light sources are discussed in section 1.6 before showing how axial resolution of the system changes with source wavelength and bandwidth, providing the motivation behind moving to shorter wavelengths. Section 1.7 shows the structure of the cornea, providing details of its composition and layer thickness, before going on to figures of merit.

1.5 Optical Coherence Tomography

First demonstrated in 1991 by Huang *et al.*, [01] time domain OCT (TDOCT) is a technique that takes advantage of low coherence interferometry to allow non-invasive imaging of living tissue, most notably the eye. Shown schematically in Figure 1-5, light from an incoherent broadband light source such as a SLED is passed through a beam splitter, after which it is used to illuminate the sample under test and a reference mirror, before both beams are reflected on to a single detector. An interference pattern is formed on the detector when light from the sample and the reference mirror are within one coherence length of each other, reaching a maximum when the distance travelled by the light incident on the sample is equal to that travelled by the light incident on the reference mirror. If the sample contains several layers, mechanically moving the reference mirror allows each corresponding maxima to be found, with each analysed interference pattern providing one reflectivity profile of the sample in terms of depth in the Z direction, known as an A-scan. However, this image only has the dimensions of the spot size of the beam. By adding an additional mirror, allowing

scanning in the X and Y direction, a series of adjacent A-scans can be used together to form a cross-sectional tomograph known as a B-scan image. Another approach to this method is *en face* TDOCT, which sets the reference mirror at a given depth, scanning in the X or Y-direction and obtaining a T-scan. If after each T-scan the reference mirror is moved as it would be after each A-scan, a B-scan will be produced from multiple T-scans, in real time.

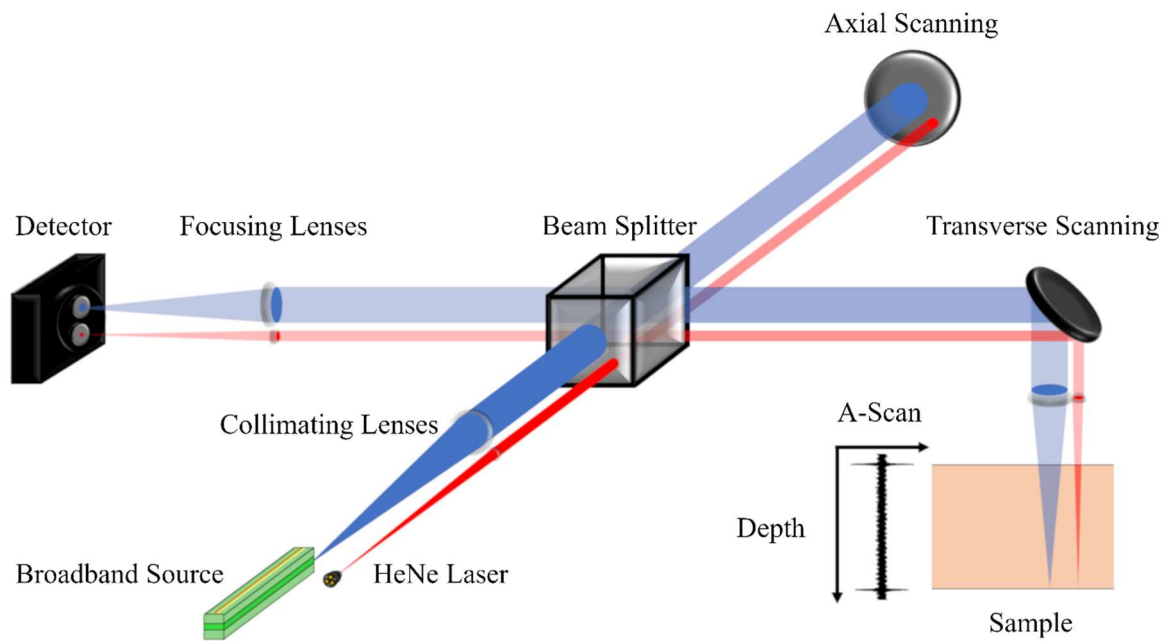


Figure 1-5 Schematic of a time domain optical coherence tomography setup

Fourier domain OCT (FDOCT) is the other widely used method of OCT and can be conducted using swept source OCT (SSOCT) or spectral domain OCT (SDOCT). As SSOCT uses a tuneable laser instead of a broadband light source, it will not be discussed further in this report. In SDOCT, after the interference pattern has been generated as described above for TDOCT, it is passed through a spectrometer before it reaches the detector, which is a charge-coupled device (CCD) instead of a photodiode. A diffraction grating separates the interference pattern into a spectrum that allows the reflectivity profile and depth information to be ascertained using a Fourier transform, with each frequency referring to a discrete depth within the sample. This removes the requirement for the moving mirror seen in TDOCT, greatly improving the imaging speed, as one scan takes enough data for a full B-scan image and even a 3-D image; in addition to doubling the resolution from $10\mu\text{m}$ in TDOCT to $5\mu\text{m}$

in FDOCT. This greatly improves the signal to noise ratio compared to TDOCT, which requires multiple scans. A schematic of a FDOCT setup can be seen in Figure 1-6 [02-04].

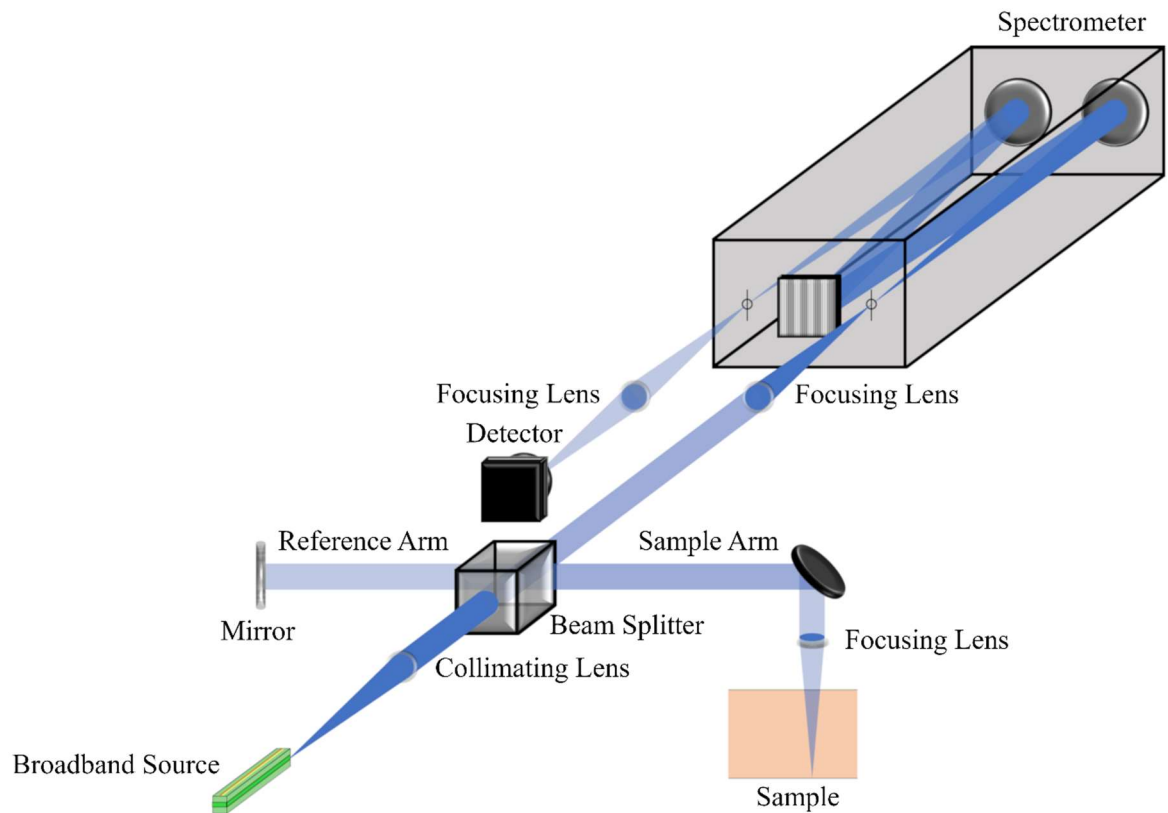


Figure 1-6 Schematic of a Fourier domain optical coherence tomography setup

1.6 Resolution

For OCT systems, axial resolution and lateral resolution are independent of one another, with axial resolution being the limit of the system to detect two objects in depth, or the Z direction. Figure 1-7a) plots the predicted axial resolution as a function of wavelength for increasing values of full width at half maximum (FWHM), or bandwidth, for an ideal light source with Gaussian distribution [12,13,17]. This is calculated from Equation 1-2:

$$l_c = \frac{2 \ln(2)}{\pi} \times \frac{\lambda_0^2}{\Delta\lambda} \quad \text{Equation 1-2}$$

where l_c is the coherence length, or axial resolution, λ_0 is the central wavelength of the light emission and $\Delta\lambda$ is the FWHM. From both Figure 1-7a) and Equation 1-2, as λ_0 increases, the magnitude of the predicted axial resolution also increases. If $\Delta\lambda$ decreases, the effect would also be to increase the magnitude of the predicted axial resolution, thereby lowering the performance of the optical system. Lateral resolution is the limit of the system to detect two objects in plane, or the X and Y direction, as a result of the beam spot size. Figure 1-7b) plots the predicted lateral resolution as a function of wavelength for increasing values of numerical aperture (NA) [03,05,06]. This is calculated from Equation 1-3:

$$r = \frac{\lambda_0}{2n \sin \theta} = \frac{\lambda_0}{2NA} \quad \text{Equation 1-3}$$

where r is the lateral resolution, λ_0 is the central wavelength of the light emission, n is the refractive index of the media and θ is the half angle of the light beam that enters the objective. From both Figure 1-7b) and Equation 1-3, as λ_0 increases, the magnitude of the predicted lateral resolution also increases. If NA decreases, the effect would also be to increase the magnitude of the predicted lateral resolution, thereby lowering the performance of the optical system. Although lateral resolution would likely see an enhancement with a shorter central wavelength, it is not the focus of this research and is not discussed further in this document.

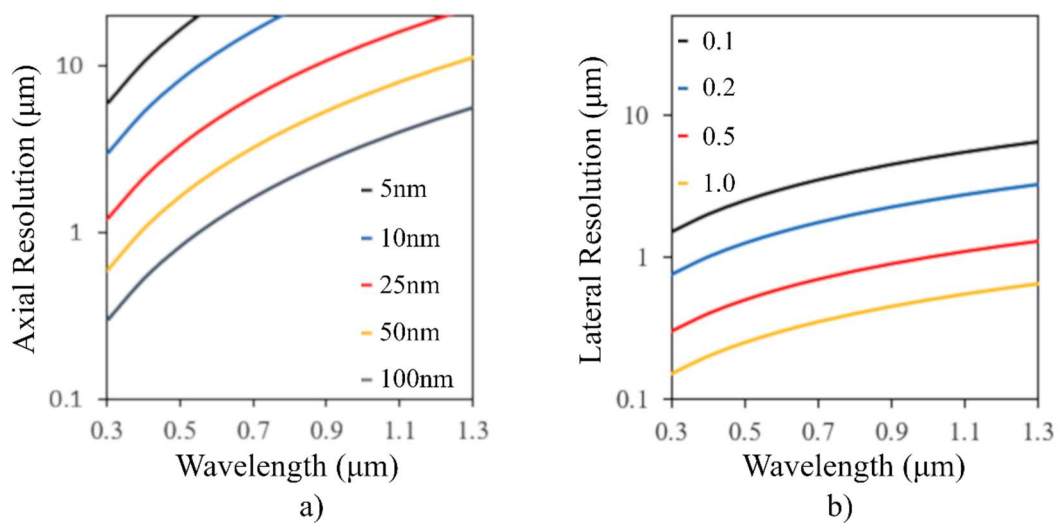


Figure 1-7 Predicted values of a) axial and b) lateral resolution for a light emitter for increasing values of a) full width at half maximum and b) numerical aperture

OCT tends to utilise the 850, 1050, and 1300nm wavelengths because 1050nm has zero dispersion in water [05], making it useful to image the aqueous tissues in the eye; whilst 1300nm has minimal scattering and absorption in skin cells [02]. Although 1050nm is largely bespoke to OCT, 850 and 1300nm are likely used due to the higher level of maturity in optical device research at these wavelengths due to their historical use in data storage and optical communications applications [06,07]. As the coherence length of the light source, l_c , is directly related to the axial resolution, as shown in Equation 1-1, operation at these longer wavelengths compromises the resolution of the system [08].

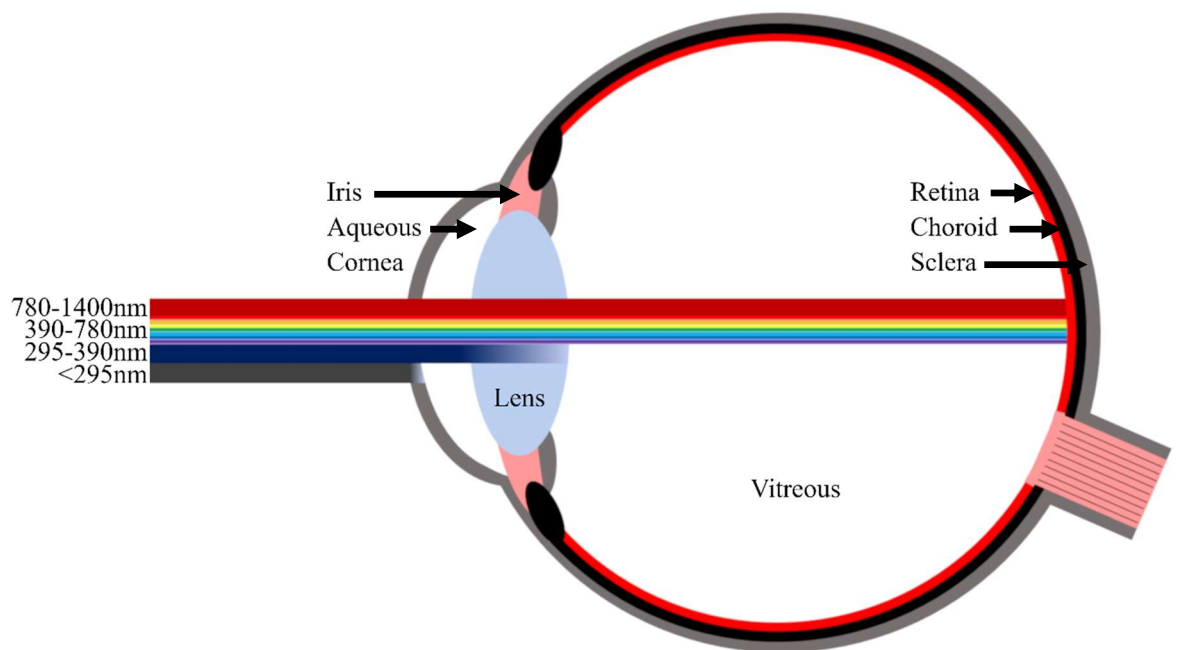


Figure 1-8 Eye cross-section showing component parts and wavelength transmission

As described in section 1.5, OCT can be used to image the eye. However, different parts of the eye are affected by different wavelengths of light in different ways; light can travel through the eye uninhibited, also known as direct transmittance, it can be reflected, scattered, or absorbed by one or several parts of the eye [09]. Figure 1-8 is a cross-section of the eye that illustrates the parts of the eye affected by different wavelengths of light, from the short ultraviolet to the near infrared. Work by Boettner and Wolter [10] examines experimentally how the eye and its component parts behave when exposed to wavelengths of light ranging from 220 to 2800nm. Their procedure involved carefully dissecting nine human eyes into

the aqueous humour, cornea, lens, and vitreous humour, before measuring direct and total transmittance using a spectrophotometer and a spectroreflectometer, respectively, using the setups shown schematically in Figure 1-9.

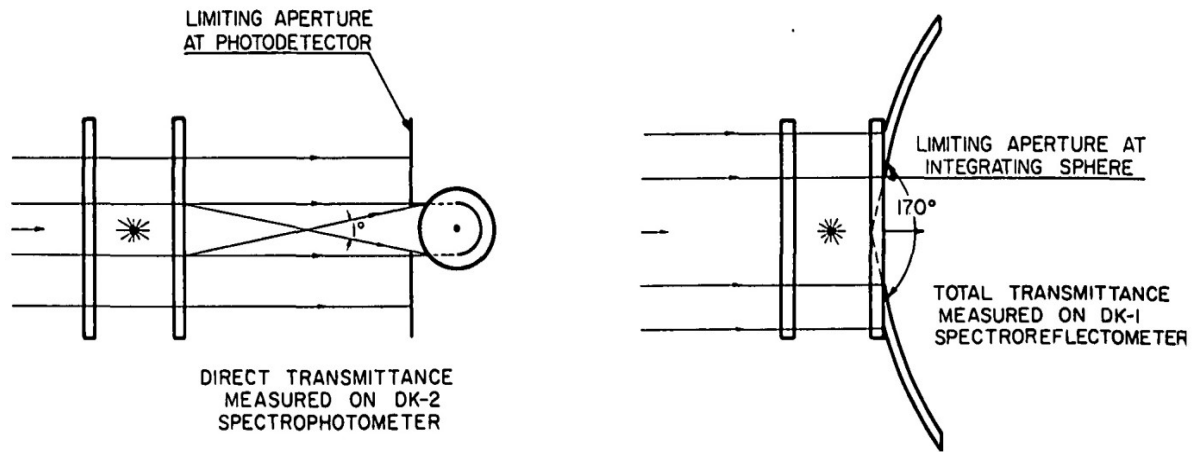


Figure 1-9 Ray diagrams of spectrophotometer and spectroreflectometer [10]

Direct transmittance was measured by positioning a photodetector behind the sample being illuminated, using a limiting aperture to restrict the light incident on the photodetector to within 1° normal to the sample. The output from the photodetector was compared with that from a reference beam operating concurrently, with the ratio of the two giving the percentage transmittance. The total transmittance, however, was measured using an integrating sphere placed behind the sample under test, with a large aperture that allowed light up to 170° from the sample to enter it. The light incident on the sphere wall was imaged by a photodetector, providing a reading of the direct and forward scattered light. Figures 1-10a) and b) illustrate the result of these measurements when conducted on the cornea and the lens, respectively.

As can be seen, the cornea will transmit wavelengths from 300 to 2500nm, with the total transmittance being greater than 80% between 400 and 1400nm. The two reductions in corneal transmittance visible at 1400 and 1900nm are due to water absorption bands present at these wavelengths. The effect of water absorption bands were visible in the transmission curves for every part of every eye that was tested. Unlike the cornea, the lens shows a much narrower band of transmission, between 400 and 1400nm. This is partly due to an absorption

band present at $\sim 350\text{nm}$ and partly due to the reduction in transmission of shorter wavelengths of light as eyes age. Short wavelength OCT would be possible on both sections.

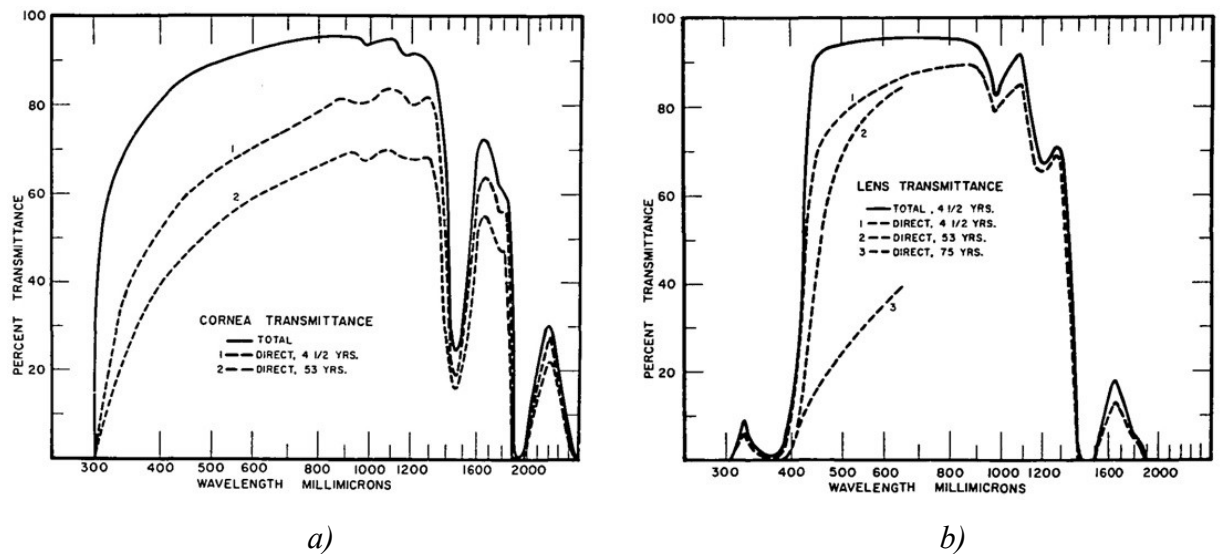


Figure 1-10 Transmittance for a) cornea and b) lens varying wavelength [10]

1.7 Short Wavelength Applications

The cornea consists of the epithelium, endothelium, and stroma, which morphologically are separated into five layers:

- Squamous epithelium, $50\mu\text{m}$ thick
- Bowman's layer, $10\mu\text{m}$ thick
- Collagenous stroma, $500\mu\text{m}$ thick
- Descemet's membrane, $8\text{-}10\mu\text{m}$
- Endothelium, $4\text{-}6\mu\text{m}$ thick

Figure 1-11 shows an OCT image of the cornea, with these five layers labelled. As some layers of the cornea are less than $10\mu\text{m}$ thick, sub- $1\mu\text{m}$ resolution is needed [11].

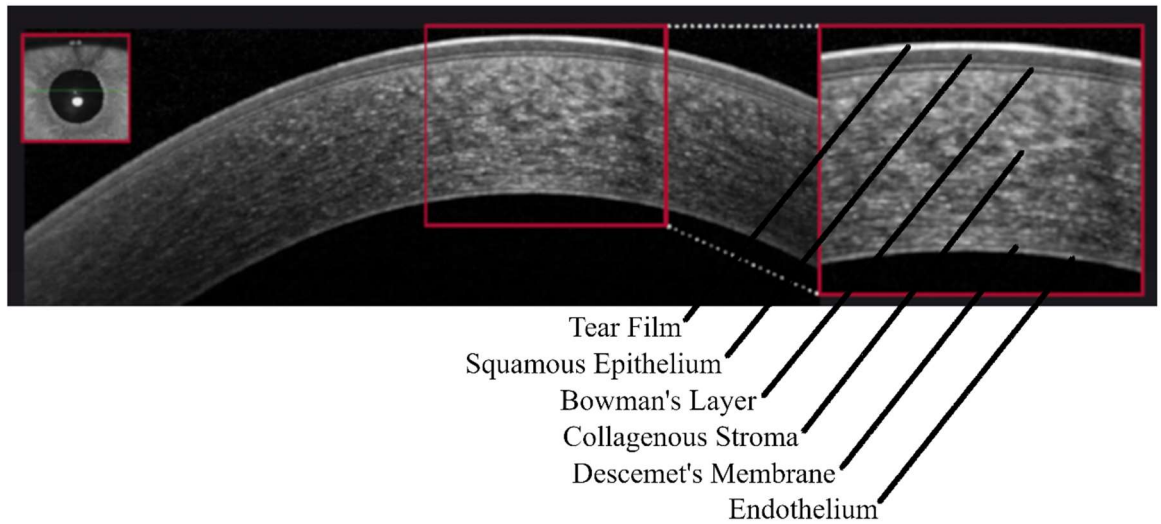


Figure 1-11 OCT image of the cornea highlighting the layer structure [38]

From Equation 1-2, it can be determined that increasing the bandwidth would have an effect on the axial resolution, but not as much as the lowering central wavelength. This is confirmed theoretically by Drexler [05] when resolution as a function of bandwidth for two SLEDs with 800 and 1300nm wavelengths is examined. It is shown that for an 800nm source with a bandwidth of 180nm, resolution of 1.6 μ m could be achieved. However, with the same bandwidth a source emitting at 1300nm would have a resolution of 4.1 μ m. Experimentally, Cucu *et al.*, [37] were able to achieve 3 μ m resolution with a SLED emitting at 890nm and a bandwidth of 150nm. For 400nm wavelengths, 3 μ m resolution is achieved with \sim 20nm bandwidth and sub-1 μ m resolution is achieved at 50nm bandwidth, demonstrating a clear advantage in lowering the central wavelength.

With 405nm the standard for Blu-Ray and other high density storage media, initial work could be carried out using these commercially available devices, with a view to using more bespoke devices operating at wavelengths below 400nm to further increase the system resolution. For a device operating at 405nm with 50nm bandwidth, sub-1 μ m resolution can be achieved. As discussed in section 1.9, GaN SLEDs emitting at \sim 400nm have been reported with bandwidths up to \sim 5nm as most research involving these devices is focused on high power applications such as pico-projection. An increase in bandwidth by 5-15nm would bring the resolution in line with longer wavelengths and enable short wavelength devices to be considered in OCT applications. This highlights the need for short wavelength,

broad bandwidth devices and is further discussed in sections 1.8 and 1.9. Such devices will be the focus of this research, with a comprehensive literature review to determine the current state of the art carried in section 1.9.

As the criteria to produce a high quality SLED is very similar to that to produce a high quality laser and, most importantly, high quality crystal is required in order to provide high gain; this means that the history of GaN SLEDs is intrinsically linked to the history of GaN lasers.

1.8 Short Wavelength Diode Lasers - Gallium Nitride

Light emitting GaN devices were first discussed in literature in 1971 [39], when Pankove *et al.*, reported blue [40] and green [41] LEDs, and Dingle *et al.* [42] reported stimulated emission, although research into GaN and its two crystal structures dates back to 1938 [43]. Work on GaN in the 1970s stemmed from the Radio Corporation of America's (RCA) desire to produce televisions that utilised LED technology. To accomplish this, red, green, and blue LEDs were required to produce a full-colour image. This presented a problem as the blue LEDs available at the time were made from silicon carbide (SiC), a II-VI indirect bandgap material unsuitable due to its low brightness and low reliability [44]. In May 1968, James Tietjen, the then director of materials research at RCA, charged Herbert Maruska with the task of producing blue LEDs using GaN, a III-V direct bandgap material [45]. Using halide vapour phase epitaxy (HVPE), the method by which Maruska had previously been growing gallium arsenide phosphide (GaAsP) LEDs, attempts were made to grow GaN. Gaseous gallium chloride (GaCl) and ammonia (NH₃) were fed in to the HVPE reactor and mixed above the substrate material.

Sapphire was chosen as the substrate as it is unreactive with ammonia, and parallel research in RCA labs meant that there was an abundance of sapphire wafers available. After some initial problems with growth temperature [46], the first single crystal films were grown [47].

It was then discerned that two factors limited the production of light emitting devices:

- Production of p-type doped GaN
- Growth of high quality material

Zinc (Zn), magnesium (Mg), mercury (Hg), silicon (Si), and germanium (Ge) were investigated as potential dopants, but success was limited. Zn and Mg increased the resistivity, ρ , to more than $1 \times 10^7 \Omega \text{m}^{-1}$, in addition to being present as deep acceptors. Hg was not incorporated in large enough concentrations to dope the material effectively, and although Si was incorporated as a shallow acceptor, the material remained n-type. Only Ge produced p-type GaN, but reproduction and uniformity were not able to be achieved. Unable to produce p-type GaN, Pankove *et al.*, fabricated Zn doped i-N, or metal insulator semiconductor (MIS), diodes [39-41] that emitted 475nm blue and 530nm green light, respectively. The difference in wavelength was determined by the Zn vapour pressure, which controlled the concentration of Zn in the intrinsic region, with higher pressure giving green light and lower pressure giving blue. However, these devices required a potential difference of 60-100V and the green LED was reportedly highly sensitive to changes in temperature.

In 1972, Mg was re-examined as a potential dopant as Maruska *et al.*, attempted to obtain shorter wavelengths. [48,49]. Luminescence at 425nm was achieved through Mg doping, but this required a bias of 160V. By changing the contacts to an Ohmic indium (In) amalgam as depicted in Figure 1-12 and annealing for 60 seconds at 400°C, this bias reduced to 10-20V with a comparable performance to the Zn doped MIS diodes [50,51]. Work by Ilegems and Dingle [52] confirmed Mg was a suitable dopant, however Ilegems and Montgomery claimed p-type GaN was unlikely to be achieved with the standard of crystal growth currently available [53]. Maruska *et al.*, and Pankove *et al.*, investigated the mechanism of light emission in the MIS diodes, attributing the luminescence to impact ionisation localised at cathode [54-56]. Due to the low efficiency of the devices, with the highest external quantum efficiency (EQE) achieved in the Mg doped devices being 0.005%, the project was terminated by RCA in 1974 [57,58].

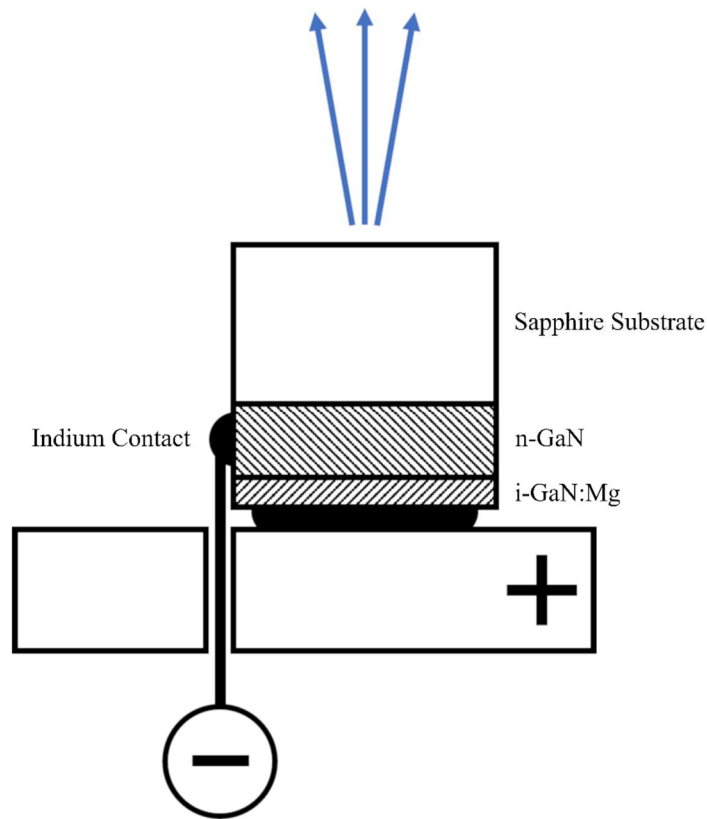


Figure 1-12 Schematic diagram of a Mg-doped metal insulator semiconductor GaN diode

The development of metal organic vapour phase epitaxy (MOVPE) [59,60] and molecular beam epitaxy (MBE) [61] brought about improvements in growth quality and helped to reignite interest in GaN, with Yoshida *et al.*, growing GaN by MBE in 1982 [62]. It was shown that by first growing a layer of aluminium nitride (AlN) on sapphire prior to GaN the Hall mobility and luminescence were greatly improved, with the Hall mobility rising from $\sim 200\text{cm}^2/\text{Vs}$ [44] to $500\text{cm}^2/\text{Vs}$ at 77K [62,63] as well as the Hall mobility becoming independent of the film thickness. Although discussed in earlier literature, this was the first time the 13.9% lattice mismatch and difference in thermal expansion coefficients between GaN and sapphire were investigated as some of the causes of lower crystal quality [62].

These findings were first confirmed by Amano *et al.*, [63] when GaN films with AlN buffer layers were grown using MOVPE, then by Hiramatsu *et al.*, [64] and Murakami *et al.*, [65] as the AlN buffer layer growth mechanisms were researched further. Figure 1-13 shows a cross sectional sketch of one of these GaN films, with AlN growing in high density series of columns from the sapphire substrate.

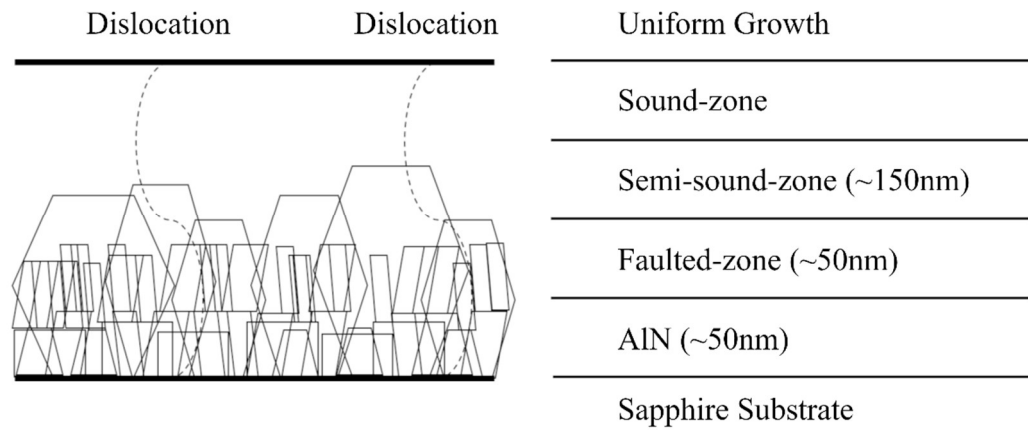


Figure 1-13 Cross-sectional diagram of GaN with an AlN buffer layer - Adapted from [64]

This is due to its crystallisation at the high GaN growth temperatures of $\sim 1000^{\circ}\text{C}$ and lattice mismatch of $\sim 13\%$ with sapphire. Once the desired deposition has been reached, GaN is grown on top of the AlN buffer layer. This forms a layer with a high number of faults, labelled below as the faulted zone. After $\sim 50\text{nm}$ the GaN crystals increase in size, forming progressively larger trapezoid structures on top of the original columns in an area of fewer faults termed the semi sound zone. Finally, the trapezoids coalesce after $\sim 150\text{nm}$ in the sound zone, resulting in high quality GaN growth with drastically lower defect densities.

By placing the main reactant gas flow in parallel to the substrate surface and a secondary gas flow of nitrogen (N_2) and hydrogen (H_2) perpendicular to the main gas flow to direct the reactant gas on to the substrate, Shuji Nakamura was able to grow GaN films on sapphire substrates using a GaN buffer layer instead of the AlN buffer layer [66]. This modification to the MOVPE reactor design, called the two-flow system [67], increased the Hall mobility to $1500\text{cm}^2/\text{Vs}$ at 77K and reduced the carrier concentration to $8 \times 10^{15}/\text{cm}^3$ from $5 \times 10^{16}/\text{cm}^3$. The effect of varying the buffer layer thickness from $10\text{-}120\text{nm}$ was also investigated by Nakamura, with 20nm offering the lowest carrier concentration and therefore producing the fewest n-type impurities.

These advances in crystal growth techniques produced the highest quality GaN to date [64,66], but production of p-type material had still not been achieved, restricting GaN to use

in MIS diodes [54]. However, when Zn doped GaN was examined under an electron microscope by Amano *et al.*, [68] they observed that its luminescence significantly increased. The luminescent intensity of the Zn doped material was then investigated for varying electron beam (EB) irradiation times at both 12K and room temperature (RT), with the results compared to those obtained under the same conditions for un-doped GaN. It was shown that luminescent intensity only increased under irradiation with Zn doped GaN, increasing with EB irradiation time and temperature. Terming the technique low energy electron beam irradiation (LEEBI), Amano *et al.*, [69] were able to use this method to increase the luminescence in Zn and Mg doped GaN, using the latter to produce the first GaN p-n junction LED, emitting in the ultraviolet (UV) portion of the spectrum at 370nm. This LED exhibited a much lower resistance than the MIS GaN LED devices described previously, showing a forward voltage $\sim 6V$ at 2mA [54], as well as much improved emission intensity. Utilising the same technique, Nakamura *et al.* reported visible LEDs operating at 430nm [70,71] and 411nm [72] soon after, with peak output powers of $42\mu W$ [70,71] and $90\mu W$ [72], 6-12 times greater than the commercial SiC LEDs available at the time, and EQEs of 0.15-0.18%, 36 times greater than that achieved by Maruska *et al.* in 1974 [54]. The forward voltage had also been lowered to 4V at 20mA, with this improvement attributed to the lower resistivity, $2\Omega cm$, in the GaN buffer layer [66], compared with $12\Omega cm$ in the AlN buffer layer [65].

However, one of the drawbacks of LEEBI is that only the surface of the material and a thin layer beneath it becomes p-type, as the incident electrons do not penetrate very far into the sample, $\sim 0.8\mu m$ at 15kV. It was discovered that thermal annealing in an N_2 environment produced the same reduction in resistivity and production of p-type GaN as LEEBI, but for the entire depth of the sample [73]. Further research showed that the sample resistivity reached a maximum value of $10^6\Omega cm$ when it was thermally annealed in NH_3 and a minimum value of $2\Omega cm$ when thermally annealed in N_2 , with these processes being reversible [74]. This demonstrated that the NH_3 was causing the high resistivity exhibited in p-type GaN. Although various hypotheses were considered with regards to the reasons behind this, it was concluded the dissociation of NH_3 into its constituent parts passivated the surface of the substrate in a similar manner to that seen on silicon [75]. During growth, these hydrogen atoms diffuse from the substrate surface into the GaN material, passivating the donors by bonding to the defects and passivating the acceptors by forming neutral ZnH and

MgH complexes. Whereas in the N_2 environment, there is no hydrogen with which the acceptors can form neutral complexes, or, in the case where the sample has already been exposed to an NH_3 environment, the increased temperature releases hydrogen from the neutral complexes, lowering the resistivity by reversing the passivation of acceptors [73].

The techniques to improve GaN crystal quality discussed earlier in this report were applied to the growth of indium gallium nitride (InGaN), which was grown between p-type and n-type GaN to produce the first double-heterostructure (DH) blue LED with the schematic shown in Figure 1-14a) [76-78]. DH devices provide a means of carrier confinement important for high power, high efficiency semiconductor optical devices, particularly lasers and SLEDs. The DH LED exhibited an output power of $125\mu W$ at 20mA, around three times greater than the output power of the homostructure GaN LED [71] with an EQE of 0.22%. It was also more than twice the power and EQE of a similar zinc selenide (ZnSe) DH LED, a II-VI direct bandgap semiconductor material being investigated as an alternative to GaN [79-81] that Xie *et al.*, reported output powers of $60\mu W$ at 20mA and an EQE of 0.1% [80].

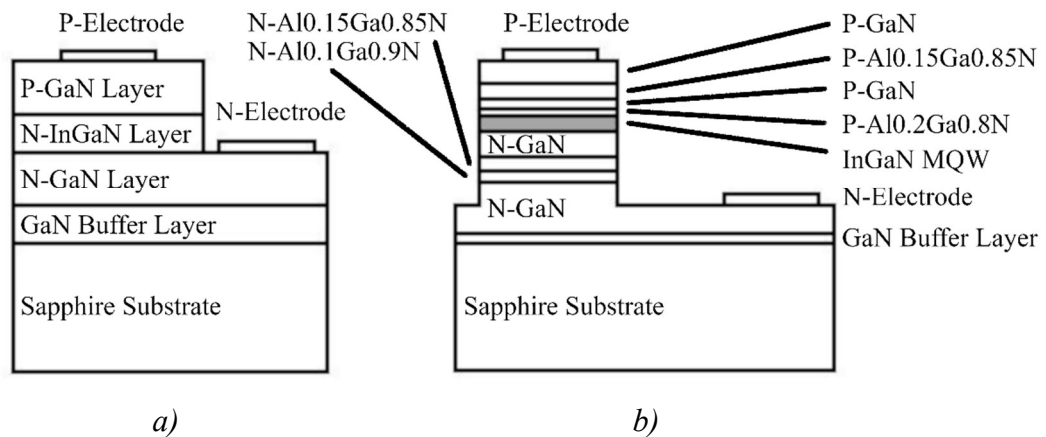


Figure 1-14 Cross-section of GaN double heterostructure (a) LED and (b) laser

Nakamura *et al.*, [72,82,83] investigated different growth conditions, different dopants, and dopant levels, particularly for the InGaN layer; reporting changes in emission wavelength and improvements in output power and EQE. This culminated in the disclosure of blue DH LEDs with 5mW output powers at 450nm and green DH LEDs with 3mW output powers at

520nm, with EQEs of 9.1% and 6.3%, respectively [83], making commercial production and applications viable for III-V nitride LEDs. Focus then shifted from spontaneous to stimulated emission devices, as groups worked to produce a GaN DH device. Stimulated emission in GaN by pulsed current injection was achieved in 1995 for the first time by Akasaki *et al.*, [85] with GaN laser diodes then demonstrated by Nakamura *et al.*, in 1996 with etched [77] and cleaved facets [86]. The schematic structure of the laser diode is shown in Figure 1-14b), which had a threshold current of 1.7A, threshold current density of 4kAcm^{-2} , central wavelength of 417nm, 1.6nm bandwidth and output power of 215mW at 2.3A. This led to ridge-geometry devices [87] and continuous wave (CW) operation at 233K [88] and 300K, room temperature [89], with device lifetimes improved from 27 hours to 10,000 hours [90-93].

With thin film GaN research mature enough to repeatedly grow reliable single quantum well (SQW) and multiple quantum well (MQW) devices, there was a greater focus on developing lattice matched native GaN substrates to replace sapphire [93] and SiC [94]. This offered the potential advantages of defect densities lower than 10^8cm^{-2} and reducing or removing the bowing observed due to the stress from the lattice mismatch [58,95]. The main methods of producing GaN substrates are HVPE [96-98], high pressure, high temperature (HPHT) [99-102], and ammonothermal [103,104]; although lesser used methods such as sublimation [105] and sodium (Na) flux [106] have also been demonstrated. HVPE was discussed earlier in this section, as well as various approaches to improve crystal quality [46,47,63,66,107].

To obtain a pure GaN substrate, growth is conducted using the aforementioned techniques on a foreign substrate to produce a thick GaN layer, which is then delaminated by mechanical polishing and lapping [97,108], heat treatment [109] or laser induced lift off [110]. High growth rates make this an attractive option, and with the development of dislocation elimination by the epitaxial growth with inverse pyramidal pits (DEEP), threading dislocations can be reduced to 10^3cm^{-2} [95]. However, the GaN is often still bowed as the stress from growth on a foreign substrate is not removed after delamination. HPHT takes advantage of an increased input nitrogen pressure, $\sim 15\text{kbar}$, to reduce both the melting point and temperature at which Ga dissociates from its precursors, $\sim 1780\text{K}$ [100-102]. Whilst offering defect densities of 10^2cm^{-2} , crystal growth is slow with maximum diameters limited

to an inch or less. [111]. Ammonothermal growth uses an autoclave which has two distinct sections operating under two different temperatures to grow GaN on native seeds. GaN is dissolved in one high temperature section, travelling by convection to a second, lower temperature, section of the autoclave where it crystallises [103,104]. With dislocation densities reported of 10^3cm^{-2} , this is comparable to HVPE but with lower growth temperatures of 780-800K. However, the growth rate is still low and HVPE the more mature technique. [112,113].

1.9 Gallium Nitride SLEDs

With a large percentage of the total research into nitride light emitters spent investigating methods to improve device lifetime and reduce the central wavelength [90-93], limited effort was made to fabricate other optoelectronic devices based on nitrides, so the first GaN SLED was not reported until 2009 by Feltin *et al.*, [29]. The SLED operates in the same manner as the GaAs, InP and non-GaN SLEDs described in section 1.4, however optical feedback is removed through the use of tilted facets only, no AR coatings or bent waveguides [18-28]. With a central wavelength of 420nm and a bandwidth of $\sim 5\text{nm}$, a peak output power of 100mW at 630mA was demonstrated under pulsed operation [29]. These characteristics were improved upon the following year, with CW operation achieved thanks to improved thermal management, and ripple reduction due to the use of AR coating on the facets [30]. The bandwidth, however, remained at $\sim 5\text{nm}$, a result matched by Holc *et al.*, [31].

Figure 1-15a) shows a similar GaN SLED design used by the previous groups [29-31]. By modifying the shape of the waveguide from linear to the tapered design in Figure 1-15b), as well as separating it from the facet by a distance of $5\mu\text{m}$, Ohno *et al.*, were able to achieve optical output powers of up to 200mW [32]. The tapered waveguide design minimises the propagation loss, as well as reducing the optical density at the front facet, and the separation of the waveguide from the front facet reduces reflectivity to 10^{-8} . 200mW optical output power was also obtained by Kafar *et al.*, [33] with a so-called j shape waveguide, of which

half is curved and half is linear [34,35]. This is one of the several ways identified in section 1.3 of suppressing lasing [36].

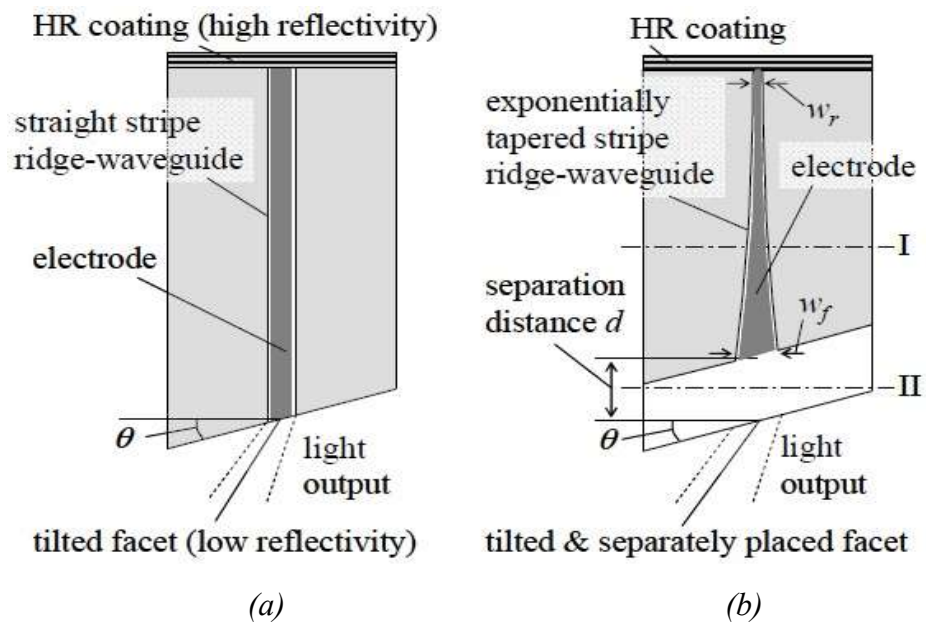


Figure 1-15 Schematic diagram of (a) GaN SLED and (b) 200mW GaN SLED [32]

Described in the introduction to this report and in sections 1.6, 1.7, and 1.8, the resolution to image the individual layers of the cornea using OCT is sub- $1\mu\text{m}$. For a 400nm light source, this would require a bandwidth of $\sim 50\text{nm}$.

1.10 Gaps in Knowledge

As discussed throughout this chapter, limited work has been conducted on OCT using short wavelength broadband sources such as GaN SLEDs, with the majority of research looking at high-power applications such as pico-projection. As such, there has been limited work on the use of SLEDs incorporating biased absorber sections to suppress lasing and offer spectral bandwidth control. Finally, multi-section GaN SLEDs have yet to be investigated.

References

- [01] D Huang, E A Swanson, C P Lin, J S Schuman, W G Stinson, W Chang, M R Hee, T Flotte, K Gregory, C A Puliavito and J G Fujimoto, "Optical Coherence Tomography", *Science*, **254**, Number 5035, pp1178-1181, November 1991.
- [02] A F Fercher, W Drexler, C K Hitzenberger and T Lasser, "Optical Coherence Tomography - Principles and Applications", *Reports on Progress in Physics*, **66**, Number 2, pp 239-303, February 2003.
- [03] J M Schmitt, "Optical Coherence Tomography (OCT) - A Review", *IEEE Journal of Selected Topics in Quantum Electronics*, **5**, Number 4, pp1205-1215, August 1999.
- [04] A Gh Podoleanu, "Optical Coherence Tomography", *Journal of Microscopy*, **247**, Number 3, pp209-219, September 2012.
- [05] W Drexler, "Ultrahigh-resolution Optical Coherence Tomography", *Journal of Biomedical Optics*, **9**, Number 1, pp47-74, February 2004.
- [06] J Crisp, "Introduction to Fiber Optics", 2nd Edition, Biddles Ltd, Chapter 3, pp19-20, 2001.
- [07] M Azadeh, "Fiber Optics Engineering", Springer, Chapter 5, pp126-155, 2009.
- [08] W Drexler, J G Fujimoto, "Optical Coherence Tomography - Technology and Applications", Springer, 2008, pp126.
- [09] M Rozanowska, B Rozanowski, M Boulton, "Light Induced Damage to the Retina - Current Understanding of the Mechanisms and Unresolved Questions", *Photochemistry and Photobiology*, **88**, Number 6, pp1303-1308, December 2012.
- [10] E A Boettner and J R Wolter, "Transmission of the Ocular Media", *Investigative Ophthalmology and Visual Science*, **1**, Number 6, pp 776-783, December 1962.
- [11] J W Ruberti, A S Roy and C J Roberts, "Corneal Structure and Function", *Annual Review of Biomedical Engineering*, **13**, pp269-295, August 2011.
- [12] L A Coldren, S W Corzine and M L Masanovic, "Diode Lasers and Photonic Integrated Circuits", 2nd Edition, Wiley, 2012.
- [13] W T Silfvast, "Laser Fundamentals", 2nd Edition, Cambridge University Press, Chapter 9, pp290-319, 2004.
- [14] W K Burns, C L Chen and R P Moeller, "Fiber-Optic Gyroscopes with Broad-Band Sources", *Journal of Lightwave Technology*, **1**, Number 1, pp98-105, March 1983.

- [15] U T Schwarz, F Kopp, T Weig, C Eichler and U Strauss, "Superluminescent Light Emitting Diodes of 100mW Output Power for Pico-Projection", Conference on Lasers and Electro-Optics Pacific Rim (CLEO-PR), pp1-2, June 2013.
- [16] G E Stillman and C M Wolfe, "Physical Properties of Semiconductors", Prentice Hall, 1989.
- [17] M Fox, "Optical Properties of Solids", 2nd Edition, Oxford, 2010.
- [18] T P Lee, C A Burrus Jr and B I Miller, "A Stripe Geometry Double-Heterostructure Amplified-Spontaneous-Emission (Superluminescent) Diode", Journal of Quantum Electronics, **9**, Number 8, pp820-828, August 1973.
- [19] G A Alphonse, D B Gilbert, M G Harvey and M Ettenberg, "High-Power Superluminescent Diodes", Journal of Quantum Electronics, **24**, Number 12, pp2454-2457, December 1988.
- [20] Z Y Zhang, I J Luxmoore, C Y Jin, H Y Liu, Q Jiang, K M Groom, D T Childs, M Hopkinson, A G Cullis and R A Hogg, "Effect of Facet Angle on Effective Facet Reflectivity and Operating Characteristics of Quantum Dot Edge Emitting Lasers and Superluminescent Light Emitting Diodes", Applied Physics Letters, **91**, pp081112-1-3, August 2007.
- [21] P D L Judson, K M Groom, D T D Childs, M Hopkinson and R A Hogg, "Multi-Section Quantum Dot Superluminescent Diodes for Spectral Shape Engineering", IET Optoelectronics, **3**, Number 2, pp100-104, November 2008.
- [22] R A Hogg, P D L Greenwood, D T D Childs, N Krstajic, K Kennedy, K M Groom, M Hugues, M Hopkinson, L E Smith, S J Matcher, M Bonesi, S Macneil and R Smallwood, "GaAs Based Quantum Dot Superluminescent Diodes for Optical Coherence Tomography of Skin Tissue", International Conference on Computers and Devices for Communication, pp1-6, December 2009.
- [23] N S K Kwong, K Y Lau, N Bar-Chaim, I Ury and K J Lee, "High-Power, High Efficiency Window Buried Heterostructure GaAlAs Superluminescent Diode with Integrated Absorber", Applied Physics Letters, **51**, Number 23, pp1879-1881, December 1987.
- [24] S A Safin, A T Semenov, V R Shidlovski, N A Zhuchkov and Y V Kurnyavko, "High-Power 0.82 μ m Superluminescent Diodes with Extremely Low Fabry-Perot Modulation Depth", Electronics Letters, **28**, Number 2, pp127-129, January 1992.
- [25] A T Semenov, V R Shidlovski, S A Safin, V P Konyaev and M V Zverkov, "Superluminescent Diodes for Visible (670nm) Spectral Range Based on

- AlGaInP/GaInP Heterostructures with Tapered Grounded Absorber", *Electronics Letters*, **29**, Number 6, pp530-532, March 1993.
- [26] A T Semenov, V K Batovrin, I A Garmash, V R Shidlovsky, M V Shramenko and S D Yakubovich, "(GaAl)As SQW Superluminescent Diodes with Extremely Low Coherence Length", *Electronics Letters*, **31**, Number 4, pp314-315, February 1995.
- [27] A T Semenov, V R Shidlovski, D A Jackson, R Willsch and W Ecke, "Spectral Control in Multisection AlGaAs SQW Superluminescent Diodes at 800nm", *Electronics Letters*, **32**, Number 3, pp255-256, February, 1996.
- [28] N S K Kwong, K Y Lau and N Bar-Chaim, "High-Power High-Efficiency GaAlAs Superluminescent Diodes with an Internal Absorber for Lasing Suppression", *Journal of Quantum Electronics*, **25**, Number 4, pp696-704, April 1989.
- [29] E Feltin, A Castiglia, G Cosendey, L Sulmoni, J F Carlin, N Grandjean, Rossetti, J Dorsaz, V Laino, M Duelk and C Velez, "Broadband Blue Superluminescent Light-Emitting Diodes Based on GaN", *Applied Physics Letters*, **95**, pp081107-1-3, August 2009.
- [30] M Rossetti, J Dorsaz, R Rezzonico, M Duelk, C Velez, E Feltin, A Castiglia, G Cosendey, J F Carlin and N Grandjean, "High Power Blue-Violet Superluminescent Light Emitting Diodes with InGaN Quantum Wells", *Applied Physics Express*, **3**, pp061002-1-3, 2010.
- [31] K Holc, L Marona, R Czernecki, M Bockowski, T Suski, S Najda and P Perlin, "Temperature Dependence of Superluminescence in InGaN-Based Superluminescent Light Emitting Diode Structures", *Journal of Applied Physics*, **108**, pp013110-1-4, 2010.
- [32] H Ohno, K Orita, M Kawaguchi, K Yamanaka and S Takigawa, "200mW GaN-Based Superluminescent Diode with a Novel Waveguide Structure", *IEEE Photonics Conference*, pp505-506, October 2011.
- [33] A Kafar, S Stanczyk, G Targowski, T Oto, I Makarowa, P Wisinieski, T Suski and P Perlin, "High-Optical-Power InGaN Superluminescent Diodes with "j-shape" Waveguide", *Applied Physics Express*, **6**, pp092102-1-4, 2013.
- [34] F Kopp, T Lermer, C Eichler and U Strauss, "Cyan Superluminescent Light-Emitting Diode Based on InGaN Quantum Wells", *Applied Physics Express*, **5**, pp082105-1-3, 2012.
- [35] F Kopp, C Eichler, A Lell, S Tautz, J Ristic, B Stojetz, C Hoss, T Weig, U T Schwarz and U Strauss, "Blue Superluminescent Light-Emitting Diodes with Output Power

- Above 100mW for Picoprojection", Japanese Journal of Applied Physics, **52**, pp08JH07-1-5, 2013.
- [36] A Kafar, S Stanczyk, S Grzanka, R Czernecki, M Leszczynski, T Suski and P Perlin, "Cavity Suppression in Nitride Based Superluminescent Diodes", Journal of Applied Physics, **111**, pp083106-1-6, 2012.
- [37] R G Cucu, A Gh Podoleanu, J A Rogers, J Pedro and R B Rosen, "Combined Confocal Scanning Ophthalmoscopy/en face T-scan Based Ultrahigh Resolution OCT of the Human Retina in vivo", Optics Letters, **31**, Number 11, pp1684-1686, 2006.
- [38] <https://www.spectralis-eyehealthcheck.co.uk/examinations/examinations-of-the-anterior-segment-of-the-eye/>
- [39] J I Pankove, E A Miller, D Richman and J E Berkeyheiser, "Electroluminescence in GaN", Journal of Luminescence, **4**, Number 1, pp63-66, July 2002.
- [40] J I Pankove, E A Miller and J E Berkeyheiser, "GaN Blue Light Emitting Diodes", Journal of Luminescence, **5**, Number 1, pp84-86, March 1972.
- [41] J I Pankove, E A Miller and J E Berkeyheiser, Electron Devices Meeting, **17**, pp78, 1971.
- [42] R Dingle, K L Shaklee, R F Leheny and R B Zetterstrom, "Stimulated Emission and Laser Action in Gallium Nitride", Applied Physics Letters, **19**, Number 1, pp5-7, July 1971.
- [43] R Juza and H Hahn, "Über die Kristallstrukturen von Cu₃N, GaN und InN Metallamide und Metallnitride", Zeitschrift für Anorganische und Allgemeine Chemie, **239**, pp282-287, 1938.
- [44] H Mokoc, S Strite, G B Gao, M E Lin, B Sverdlov and M Burns, "Large-Band-Gap SiC, III-V Nitride and II-VI ZnSe-Based Semiconductor Device Technologies", Journal of Applied Physics, **76**, Number 3, pp1363-1398, August 1994.
- [45] S Nakamura, "III-V Nitride Based Light Emitting Devices", Solid State Communications, **102**, Number 2-3, pp237-248, 1997.
- [46] M R Lorenz and B B Binkowski, "Preparation, Stability and Luminescence of Gallium Nitride", Journal of the Electrochemical Society, **109**, Number 1, pp24-26, January 1962.
- [47] H P Maruska and J J Tietjen, "The Preparation and Properties of Vapor-Deposited Single-Crystal-Line GaN", Applied Physics Letters, **15**, Number 10, pp327-329, November 1969.

- [48] H P Maruska and D A Stevenson, "Violet Luminescence of Mg-Doped GaN", *Applied Physics Letters*, **22**, Number 6, pp303-305, March 1973.
- [49] H P Maruska, W C Rhines and D A Stevenson, "Preparation of Mg-Doped GaN Diodes Exhibiting Violet Electroluminescence", *Materials Research Bulletin*, **7**, Number 8, pp777-781, August 1972.
- [50] E F Schubert, "Light-Emitting Diodes", pp20-30, Second Edition, Cambridge, 2006.
- [51] O Lagerstadt and B Monemar, "Luminescence in Epitaxial GaN: Cd", *Journal of Applied Physics*, **45**, Number 5, 1974.
- [52] M Ilegems and R Dingle, "Luminescence of Be and Mg-Doped GaN", *Journal of Applied Physics*, **44**, Number 9, pp4234-4235, September 1973.
- [53] M Ilegems and H C Montgomery, "Electrical Properties of n-Type Vapor-Grown Gallium Nitride", *Journal of Physics and Chemistry of Solids*, **34**, Number 5, pp885-895, May 1973.
- [54] H P Maruska and D A Stevenson, "Mechanism of Light Production in Metal-Insulator-Semiconductor Diodes, GaN:Mg Violet Light-Emitting Diodes", *Solid State Electronics*, **17**, pp1171-1179, May 1974.
- [55] H P Maruska, L J Anderson and D A Stevenson, "Microstructural Observations on Gallium Nitride Light-Emitting Diodes", *Journal of the Electrochemical Society*, **121**, Number 9, pp1202-1207, September 1974.
- [56] J I Pankove and M A Lampert, "Model for Electroluminescence in GaN", *Physical Review Letters*, **33**, Number 6, pp361-366, August 1974.
- [57] S Nakamura and M R Krames, "History of Gallium-Nitride-Based Light-Emitting Diodes for Illumination", *Proceedings of the IEEE*, **101**, Number 10, pp2211-2220, October 2013.
- [58] S Nakamura, S Pearson, G Fasol, "The Blue Laser Diode: The Complete Story", Second Edition, Springer, 2000.
- [59] H M Manasevit, "Single-Crystal Gallium Arsenide on Insulating Substrates", *Applied Physics Letters*, **12**, Number 4, pp156-159, February 1968.
- [60] H M Manasevit, F M Erdmann and W I Simpson, "The Use of Metalorganics in the Preparation of Semiconductor Materials", *Journal of the Electrochemical Society*, **118**, Number 11, pp1864-1868, November 1971.
- [61] A Y Cho and J R Arthur, "Molecular Beam Epitaxy", *Progress in Solid-State Chemistry*, **10**, Number 3, pp157-191, 1975.

- [62] S Yoshida, S Misawa and S Gonda, "Improvements on the Electrical and Luminescent Properties of Reactive Molecular Beam Epitaxially Grown GaN Films by Using AlN-Coated Sapphire Substrates", *Applied Physics Letters*, **42**, Number 5, pp427-429, December 1982.
- [63] H Amano, N Sawaki, I Akasaki and Y Toyoda, "Metalorganic Vapor Phase Epitaxial Growth of a High Quality GaN Film Using an AlN Buffer Layer", *Applied Physics Letters*, **48**, Number 5, pp353-355, December 1985.
- [64] K Hiramatsu, S Itoh, H Amano, I Akasaki, N Kuwano, T Shiraishi and K Oki, "Growth Mechanism of GaN Grown on Sapphire with AlN Buffer Layer by MOVPE", *Journal of Crystal Growth*, **115**, Numbers 1-4, pp628-633, December 1991.
- [65] H Murakami, T Asahi, H Amano, K Hiramatsu, N Sawaki and I Akasaki, "Growth of Si-Doped AlGaN on (0001) Sapphire Substrate by Metalorganic Vapor Phase Epitaxy", *Journal of Crystal Growth*, **115**, Numbers 1-4, pp648-651, December 1991.
- [66] S Nakamura, "GaN Growth Using GaN Buffer Layer", *Japanese Journal of Applied Physics*, **30**, Number 10A, pp1705-1707, October 1991.
- [67] S Nakamura, Y Harada and M Seno, "Novel Metalorganic Chemical Vapor Deposition System for GaN Growth", *Applied Physics Letters*, **58**, Number 18, pp2021-2023, February 1991.
- [68] H Amano, I Akasaki, T Kozawa, K Hiramatsu, N Sawaki, K Ikeda and Y Ishii, "Electron Beam Effects on Blue Luminescence of Zinc-Doped GaN", *Journal of Luminescence*, **40-41**, pp121-122, February 1988.
- [69] H Amano, M Kito, K Hiramatsu and I Akasaki, "P-Type Conduction in Mg-Doped GaN Treated with Low-Energy Electron Beam Irradiation (LEEBI)", *Japanese Journal of Applied Physics*, **28**, Number 12, pp2112-2114, December 1989.
- [70] S Nakamura, M Senoh and T Mukai, "Highly P-Typed Mg-Doped GaN Films Grown with GaN Buffer Layers", *Japanese Journal of Applied Physics*, **30**, Number 10A, pp1708-1711, October 1991.
- [71] S Nakamura, T Mukai and M Senoh, "High-Power GaN P-N Junction Blue Light-Emitting Diodes", *Japanese Journal of Applied Physics*, **30**, Number 12A, pp1998-2001, December 1991.
- [72] S Nakamura, M Senoh and T Mukai, "High-Power InGaN/GaN Double-Heterostructure Violet Light Emitting Diodes", *Applied Physics Letters*, **62**, Number 19, pp2390-2392, May 1993.

- [73] S Nakamura, T Mukai, M Senoh and N Iwasa, "Thermal Annealing Effects on P-Type Mg-Doped GaN Films", Japanese Journal of Applied Physics, **31**, Number 2B, pp139-142, February 1992.
- [74] S Nakamura, N Iwasa, M Senoh and T Mukai, "Hole Compensation Mechanism of P-Type GaN Films", Japanese Journal of Applied Physics, **31**, Number 5A, pp1258-1266, May 1992.
- [75] J I Pankove, D E Carlson, J E Berkeyheiser and R O Wance, "Neutralization of Shallow Acceptor Levels in Silicon by Atomic Hydrogen", Physical Review Letters, **51**, Number 24, pp2224-2225, December 1983.
- [76] S Nakamura, M Senoh and T Mukai, "P-GaN/N-InGaN/N-GaN Double-Heterostructure Blue-Light-Emitting Diodes", Japanese Journal of Applied Physics, **32**, Numbers 1A-B, pp8-11, January 1993.
- [77] S Nakamura, M Senoh, S Nagahama, N Iwasa, T Yamada, T Matsushita, H Kiyoku and Y Sugimoto, "InGaN-Based Multi-Quantum-Well-Structure Laser Diodes", Japanese Journal of Applied Physics **35**, Number 1B, pp74-76, January 1996.
- [78] S Nakamura and T Mukai, "High-Quality InGaN Films Grown on GaN Films", Japanese Journal of Applied Physics, **31**, Number 10B, pp1457-1459, October 1992.
- [79] H Jeon, J Ding, A V Nurmikko, W Xie, M Kobayashi and R L Gunshor, "ZnSe Based Multilayer PN Junctions as Efficient Light Emitting Diodes for Display Applications", Applied Physics Letters, **60**, Number 7, pp892-894, February 1992.
- [80] W Xie, D C Grillo, R L Gunshor, M Kobayashi, H Jeon, J Ding, A V Nurmikko, G C Hua and N Otsuka, "Room Temperature Blue Light Emitting P-N Diodes from Zn(S,Se)-Based Multiple Quantum Well Structures", Applied Physics Letters, **60**, Number 16, pp1999-2001, April 1992.
- [81] H Jeon, M Hagerott, J Ding and A V Nurmikko, "Blue and Blue/Green Laser Diodes and LED-Based Display Devices", IEEE Transactions on Electron Devices, **39**, Number 11, pp2652-2653, November 1992.
- [82] S Nakamura, T Mukai and M Senoh, "Candela-Class High-Brightness InGaN/AlGaN Double-Heterostructure Blue-Light-Emitting Diodes", Applied Physics Letters, **64**, Number 13, pp1687-1689, March 1994.
- [83] S Nakamura, T Mukai and M Senoh, "High-Brightness InGaN/AlGaN Double-Heterostructure Blue-Green-Light-Emitting Diodes", Journal of Applied Physics, **76**, Number 12, pp8189-8191, December 1994.

- [84] S Nakamura, M Senoh, N Iwasa, S Nagahama, T Yamada and T Mukai, "Super-Bright Green InGaN Single-Quantum-Well-Structure Light-Emitting Diodes", Japanese Journal of Applied Physics, **34**, Number 10B, pp1332-1335, October 1995.
- [85] I Akasaki, H Amano, S Sota, H Sakai, T Tanaka and M Koike, "Stimulated Emission by Current Injection from an AlGaIn/GaN/GaInN Quantum Well Device", Japanese Journal of Applied Physics, **34**, Number 11B, pp1517-1519, November 1995.
- [86] S Nakamura, M Senoh, S Nagahama, N Iwasa, T Yamada, T Matsushita, H Kiyoku, Y Sugimoto, "InGaN Multi-Quantum-Well-Structure Laser Diodes with Cleaved Mirror Cavity Facets", Japanese Journal of Applied Physics, **35**, Number 2B, pp217-220, February 1996.
- [87] S Nakamura, M Senoh, S Nagahama, N Iwasa, T Yamada, T Matsushita, Y Sugimoto and H Kiyoku, "Ridge-Geometry InGaN Multi-Quantum-Well-Structure Laser Diodes", Applied Physics Letters, **69**, Number 10, pp1477-1479, September 1996.
- [88] S Nakamura, M Senoh, S Nagahama, N Iwasa, T Yamada, T Matsushita, Y Sugimoto and H Kiyoku, "Continuous-Wave Operation of InGaN Multi-Quantum-Well-Structure Laser Diodes at 233K", Applied Physics Letters, **69**, Number 20, pp3034-3036, November 1996.
- [89] S Nakamura, M Senoh, S Nagahama, N Iwasa, T Yamada, T Matsushita, Y Sugimoto and H Kiyoku, "Room-Temperature Continuous-Wave Operation of InGaN Multi-Quantum-Well Structure Laser Diodes", Applied Physics Letters, **69**, Number 26, pp4056-4058, December 1996.
- [90] S Nakamura, M Senoh, S Nagahama, N Iwasa, T Yamada, T Matsushita, Y Sugimoto and H Kiyoku, "Room-Temperature, Continuous-Wave Operation of InGaN Multi-Quantum-Well Structure Laser Diodes with a Lifetime of 27 Hours", Applied Physics Letters, **70**, Number 11, pp1417-1419, March 1997.
- [91] S Nakamura, M Senoh, S Nagahama, N Iwasa, T Yamada, T Matsushita, Y Sugimoto and H Kiyoku, "High-Power, Long-Lifetime InGaN Multi-Quantum-Well-Structure Laser Diodes", Japanese Journal of Applied Physics, **36**, Number 8B, pp1059-1061, August 1997.
- [92] S Nakamura, M Senoh, S Nagahama, N Iwasa, T Yamada, T Matsushita, H Kiyoku, Y Sugimoto, T Kozaki, H Umamoto, M Sano and K Chocho, "InGaIn/GaN/AlGaIn-Based Laser Diodes with Modulation-Doped Strained-Layer Superlattices", Japanese Journal of Applied Physics, **36**, Number 12A, pp1568-1571, December 1997.

- [93] T Mukai, K Takekawa and S Nakamura, "InGaN-Based Blue Light-Emitting Diodes Grown on Epitaxially Laterally Overgrown GaN Substrates", *Japanese Journal of Applied Physics*, **37**, Number 7B, pp839-841, July 1998.
- [94] O Nam, M D Bremser, T S Zheleva and R F Davis, "Lateral Epitaxy of Low Defect Density GaN Layers via Organometallic Vapor Phase Epitaxy", *Applied Physics Letters*, **71**, Number 18, pp2638-2640, November 1997.
- [95] T Nakamura and K Motoki, "GaN Substrate Technologies for Optical Devices", *Proceeding of the IEEE*, **101**, Number 10, pp2221-2228, October 2013.
- [96] C Sasaoka, H Sunakawa, A Kimura, M Nido, A Usui and A Sakai, "High-Quality InGaN MQW on Low-Dislocation-Density GaN Substrate Grown by Hydride Vapor Phase Epitaxy", *Journal of Crystal Growth*, **189-190**, pp61-66, June 1998.
- [97] S T Kim, Y J Lee, D C Moon, C H Hong and T K Koo, "Preparation and Properties of Free-Standing HVPE Grown GaN Substrates", *Journal of Crystal Growth*, **194**, pp37-42, April 1998.
- [98] T Paskova, E M Goldys and B Monemar, "Hydride Vapour-Phase Epitaxy Growth and Cathodoluminescence Characterisation of Thick GaN Films", *Journal of Crystal Growth*, **203**, pp1-11, 1999.
- [99] S Porowski and I Grzegory, "Thermodynamical Properties of III-V Nitrides and Crystal Growth of GaN at High N₂ Pressure", *Journal of Crystal Growth*, **178**, pp174-188, 1997.
- [100] I Grzegory, "High Pressure Growth of Bulk GaN from Solutions in Gallium", *Journal of Physics: Condensed Matter*, **13**, pp6875-6892, 2001.
- [101] M Bockowski, I Grzegory, S Krukowski, B Lucznik, M Wroblewski, G Kamler, J Borysiuk, P Kwiatkowski, K Jasik and S Porowski, "Deposition of Bulk GaN from Solution in Gallium Under High N₂ Pressure on Silicon Carbide and Sapphire Substrates", *Journal of Crystal Growth*, **270**, pp409-419, 2004.
- [102] I Grzegory, B Lucznik, M Bockowski and S Porowski, "Crystallization of Low Dislocation Density GaN by High-Pressure Solution and HVPE Methods", *Journal of Crystal Growth*, **300**, pp17-25, 2007.
- [103] R Dwilinski, R Doradzinski, J Garcynski, L P Sierzputowski, A Puchalski, Y Kanbara, K Yagi, H Minakuchi and H Hayashi, "Bulk Annotermal GaN", *Journal of Crystal Growth*, **311**, pp3015-3018, 2009.

- [104] R Dwilinski, R Doradzinski, J Garczynski, L P Sierzputowski, M Zajac and M Rudzinski, "Homoepitaxy on Bulk Annotermal GaN", *Journal of Crystal Growth*, **311**, pp3058-3062, 2009.
- [105] S Kurai, Y Naoi, T Abe, S Ohmi, S Sakai, "Photopumped Stimulated Emission from Homoepitaxial GaN Grown on Bulk GaN Prepared by Sublimation Method", *Japanese Journal of Applied Physics*, **35**, Number 1B, pp77-79, January 1996.
- [106] H Yamane, M Shimada, T Sekiguchi, F J DiSalvo, "Morphology and Characterization of GaN Single Crystals Grown in Na Flux", *Journal of Crystal Growth*, **186**, pp8-12, 1998.
- [107] K Naniwae, S Itoh, H Amano, K Itoh, K Hiramatsu and I Akasaki, "Growth of Single Crystal GaN Substrate Using Hydride Vapor Phase Epitaxy", *Journal of Crystal Growth*, **99**, pp381-384, 1990.
- [108] S Nakamura, M Senoh, S Nagahama, N Iwasa, T Yamada, T Matsushita, H Kiyoku, Y Sugimoto, T Kozaki, H Umemoto, M Sano and K Cohcho, "High-Power, Long-Lifetime InGaN/GaN/AlGaIn-Based Laser Diodes Grown on Pure GaN Substrates", *Japanese Journal of Applied Physics*, **37**, Number 3B, pp309-312, March 1998.
- [109] X Li, J Wu, N Liu, T Han, X Kang, T Yu and G Zhang, "Self-Separation of Two-Inch-Diameter Freestanding GaN by Hydride Vapor Phase Epitaxy and Heat Treatment of Sapphire", *Materials Letters*, **132**, pp94-97, 2014.
- [110] T Paskova, V Darakchieva, P P Paskov, U Sodervall and B Monemar, "Growth and Separation Related Properties of HVPE-GaN Free-Standing Films", *Journal of Crystal Growth*, **246**, pp207-214, 2002.
- [111] M Bockowski, P Strak, P Kempisty, I Grzegory, S Krukowski, B Lucznik and S Porowski, "High Pressure-High Temperature Seeded Growth of GaN on 1 in Sapphire/GaN Templates: Analysis of Convective Transport", *Journal of Crystal Growth*, **307**, pp259-267, 2007.
- [112] T Paskova, D A Hanser and K R Evans, "GaN Substrates for III-Nitride Devices", *Proceedings of the IEEE*, **98**, Number 7, pp1324-1338 July 2010.
- [113] T Paskova and K R Evans, "GaN Substrates - Progress, Status and Prospects", *IEEE Journal of Selected Topics in Quantum Electronics*, **15**, Number 4, July 2009.

Chapter Two - FIB Modified Commercial Laser Diodes: Concept Proof

2.1 Introduction to Chapter

As discussed in Chapter One sections 1.8 and 1.9, gallium nitride (GaN) material and devices have seen rapid development since their first disclosure in 1971 [01-29] and are now readily commercially available [30]. With a high quality crystal and substrate, narrower bandwidths, greater output powers, and improved reliability and robustness were demonstrated [16-19,28,29,31,32].

Such milestones in the history of GaN laser devices, with the first viable light emitting diode reported in 1991 [15] and laser in 1996 [18], paved the way for marked and rapid progress in superluminescent light emitting diodes (SLEDs). However, the focus thus far has largely been on achieving ever-increasing output powers for pico-projection applications [33-35], which only require very modest bandwidths to ensure high powers. Work has therefore included high reflection coatings [36] and thermal management techniques [37], which are necessary as the output power increases, while bandwidths remain $\sim 5\text{nm}$ [33-39]. Limited research has been conducted in methods to enhance the bandwidth beyond this level, or indeed to explore the possibility of short wavelength devices being used for optical coherence tomography (OCT) applications [40-44].

Demand for greater axial resolution in OCT systems has resulted in the feasibility of wavelengths outside of the traditional 800 and 1300nm windows [41-44] being investigated, with limited 400nm sources leading to super-continuum lasers and non-linear fibre-based light sources [45] being used to access shorter wavelengths. However, both light sources require complex supplementary systems before they can be used for OCT [45-47]. If the

bandwidth of GaN SLEDs could be extended to $\sim 10\text{nm}$ at moderate output powers, it would offer opportunities for more efficient short-wavelength OCT systems, as well as multi-source systems [48] as alternatives to super-continuum lasers and non-linear fibre-based light sources [45-47]. Techniques for broadening the emission spectrum have been discussed in Chapter One and shown successfully in other material systems like gallium arsenide (GaAs) and indium phosphide (InP) [49-59]. Although there have been attempts to transfer these techniques to GaN devices, this has mainly been accomplished through the use of angled facets [34,36] and curved waveguides [60,61], with the potential for absorber sections in GaN SLEDs not yet fully realised. Absorber sections are those optically connected but electrically separate from the section of the device being used for light emission [36].

2.2 Outline of Chapter

In this chapter, the feasibility of an absorber section within a GaN SLED is investigated. Commercially available laser diodes are modified using a focused ion beam (FIB) system, and a passive, or open-circuit (O/C), absorber is created towards the rear of the device. This demonstrates the transferability of this technique from GaAs and InP devices to GaN, and that it reliably produces a SLED.

Section 2.3 describes the experimental setup and examines its suitability for conducting short wavelength measurements. Section 2.4 characterises several commercially available 405nm GaN laser diodes, demonstrating their performance below, approaching, and above lasing threshold, highlighting the uniformity of key parameters, and agreeing the results with device datasheets. Section 2.5 repeats elements of the characterisation carried out in section 2.4 following the use of a FIB system to modify a number of the laser diodes to produce SLEDs, to ensure minimal damage to the devices. The differences in device behaviours are analysed, and the feasibility of an absorber section within a GaN SLED is investigated. Section 2.6 introduces the point spread function (PSF), discussing its merit as a measure of resolution, and comparing values produced using this method to those calculated using first principles and theory. The PSF is then measured for the GaN SLED, with the PSF providing

the expected maximum resolution achievable should the device be deployed in an OCT system, with resolutions between $\sim 4.5\mu\text{m}$ and $\sim 11\mu\text{m}$ reported. Section 2.7 describes the construction and operation of an OCT experimental setup, or an interferometer, confirming the PSF can be accurately determined from the emission spectrum. The interferometer is then used to demonstrate OCT metrology measurements with a GaN SLED for the first time.

This forms part of the work published in my IEEE Journal of Selected Topics in Quantum Electronics paper.

2.3 Design of Experimental Setup

With the focus prior to this work on longer wavelength devices in the infrared part of the spectrum, an experimental setup capable of testing short wavelength devices such as GaN was not available when this work began. As such, setting up a short wavelength spectrometer with a suitable resolution to perform measurements; designing a system to obtain output power, current density, and voltage curves in the visible spectrum; and selecting current sources able to provide currents at the higher voltages required for wide bandgap material, were required prior to experimental work being carried out.

An experimental setup was constructed to permit standard characterisation of light emitting devices [62]. Figure 2-1a) shows a schematic of the Spex 1704 [63] spectrometer used to measure emission spectra from such devices. The device under test (DUT) is placed some distance from the entrance slit of the spectrometer, behind a pair of lenses. The first, *Collimating Lens*, collimates the diverging light emitted by the DUT; and the second, *Focusing Lens 1*, focuses the collimated light such that only a spot is incident on the entrance slit of the spectrometer. As it propagates along the length of the spectrometer the light diverges, ideally filling the first of two mirrors, *Mirror 1*, which reflects the light back along the length of the spectrometer onto the diffraction grating, where it is diffracted into its constituent wavelengths.

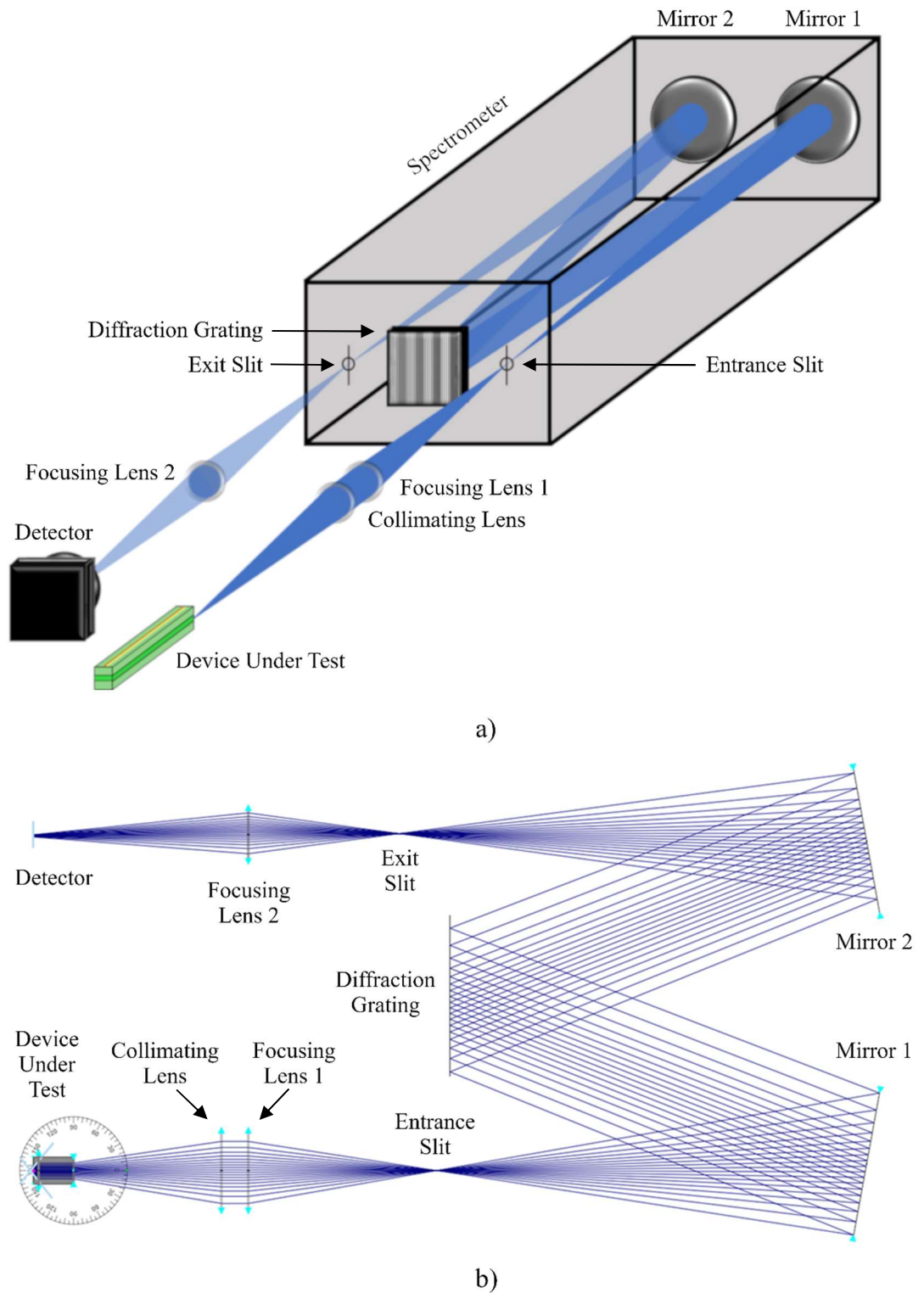


Figure 2-1 Emission spectra experimental setup a) schematic and b) ray diagram

The diffracted light then propagates to the second mirror, *Mirror 2*, where it is reflected onto the exit slit of the spectrometer. Before it is incident on the photodetector the light passes through a final lens, *Focusing Lens 2*, focusing the light so the sensor is optimally filled.

Figure 2-1b) shows a ray diagram [64] depicting how the light propagates from the DUT and through the spectrometer in Figure 2-1a) before it is incident on the photodetector. To calibrate the diffraction grating, a mercury argon lamp [65] was used in place of the DUT as it emits many strong spectral lines between 253-922nm at defined, precise wavelengths. Using a Labview program to interface with the spectrometer and the detector, the diffraction grating was swept between 250-1000nm and the spectrum recorded. The emission spectrum and associated maxima were compared to the expected wavelengths in the manual; with the grating alignment adjusted and this process repeated until the measured spectra was in good agreement with the expected values, within 1nm in the 400nm region.

With a focal length of 1m, a maximum resolution of 0.1 angstroms, \AA , or 0.01nm is offered [63,66]. For shorter wavelengths, higher resolution is important due to narrower longitudinal mode spacing, particularly for gain measurements. The mode separation can be calculated using Equation 2-1:

$$\Delta\lambda = \frac{\lambda_0^2}{2nL} \quad \text{Equation 2-1}$$

where λ_0 is the central wavelength of the light emission, n is the refractive index of the material, and L is the cavity length [67,68]. Table 2-1 shows the effect of increasing λ on the mode spacing and therefore the required resolution for four cavity lengths, 800, 1600, 2400, and 3200 μm , with a refractive index of 2.5 [69]. A typical cavity length for a commercial semiconductor laser is 800 μm [30,70-72], which would require a resolution of 0.040nm at 400nm wavelengths. The resolution limit of the Spex 1704 is not reached until a cavity length of 3200 μm , where the required resolution is 0.010nm at 400nm wavelengths.

The commercial laser diodes discussed in this chapter have a cavity length of 800 μm , and the devices fabricated as part of this research discussed in Chapters Three and Four have cavity lengths ranging from ~2400-3000 μm , meaning the resolution offered by the Spex 1704 will be sufficient.

Central Wavelength (nm)	Mode Spacing 800 μ m Cavity Length (nm)	Mode Spacing 1600 μ m Cavity Length (nm)	Mode Spacing 2400 μ m Cavity Length (nm)	Mode Spacing 3200 μ m Cavity Length (nm)
400	0.040	0.020	0.013	0.010
500	0.063	0.031	0.020	0.016
600	0.090	0.045	0.029	0.023
700	0.123	0.061	0.039	0.031
800	0.160	0.080	0.051	0.040
900	0.203	0.101	0.065	0.051
1000	0.250	0.125	0.080	0.063

Table 2-1 Mode Spacing for Varying Wavelengths at Four Different Cavity Lengths

2.4 Characterisation of Commercial GaN Laser Diodes

Figure 2-2a) and b) depict scanning electron microscope (SEM) images of a commercially available GaN laser diode, Nichia NDV4316 [30], from the front and above, respectively. Several of these 2 μ m wide, 800 μ m long, commercial laser diodes were purchased to allow characterisation of devices with defined behaviours.

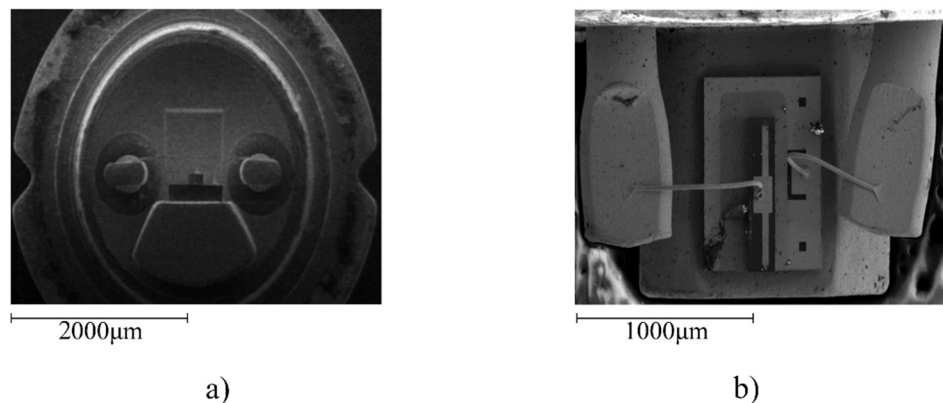


Figure 2-2 Scanning electron microscope images of one of the commercial laser diodes from the a) front and b) above

Figure 2-3a) plots emission spectra as a function of wavelength for different levels of continuous wave (CW) injected current, 0.6, 1.3, 1.9, and 2.5 kA/cm², applied to the device which has a threshold of ~2.2 kA/cm². This ensured that for all current densities the observed emission spectra were broad, smooth, and continuous. Figure 2-3b) plots the emission spectra from Figure 2-3a), normalised. As the current density is increased, the full width at half maximum (FWHM), or bandwidth, of the device decreases, and the central wavelength, λ_0 , undergoes a moderate blueshift. All measurements in this chapter were conducted CW.

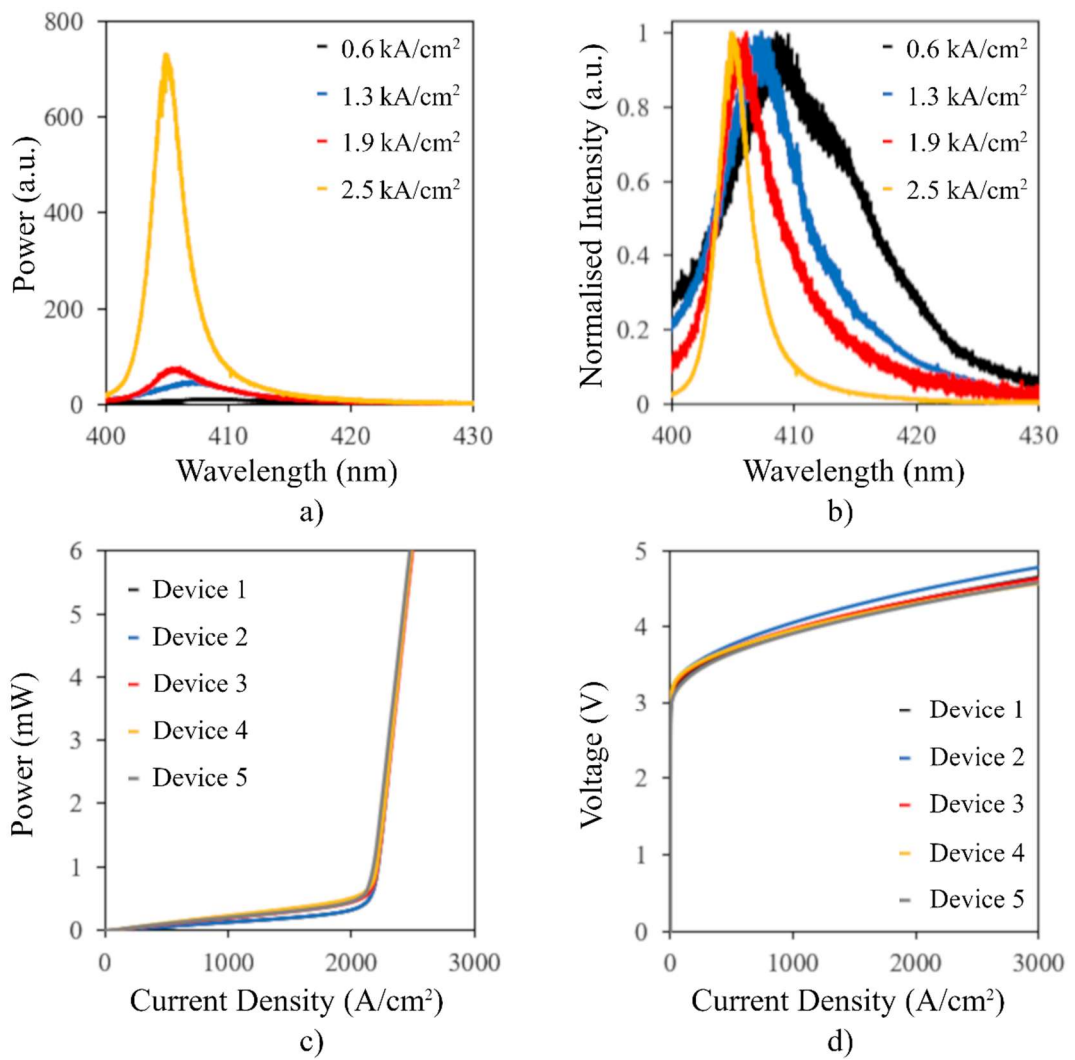


Figure 2-3 GaN laser diode a) emission spectra for various applied current densities b) normalised emission spectra for various applied current densities c) optical output power for injected current density and d) voltage for injected current density

Figure 2-3c) plots optical output power as a function of current density for five similar devices. As expected, as the current density increases optical output power also increases, with super-linearity observed both below lasing threshold and above. Figure 2-3d) plots voltage as a function of current density for the 5 similar devices in Figure 2-3c). This gives an average series resistance of $\sim 45\Omega$, which is comparable with the value calculated from the datasheet of $\sim 37\Omega$ [30]. The variance is attributed to higher resistance between the elements in the constructed experimental setup. To ensure self-heating was minimised, a thermoelectric cooler (TEC) and thermistor were mounted beneath the DUT, with a heatsink to help dissipate excess heat. The desired temperature was set at 20°C for all measurements.

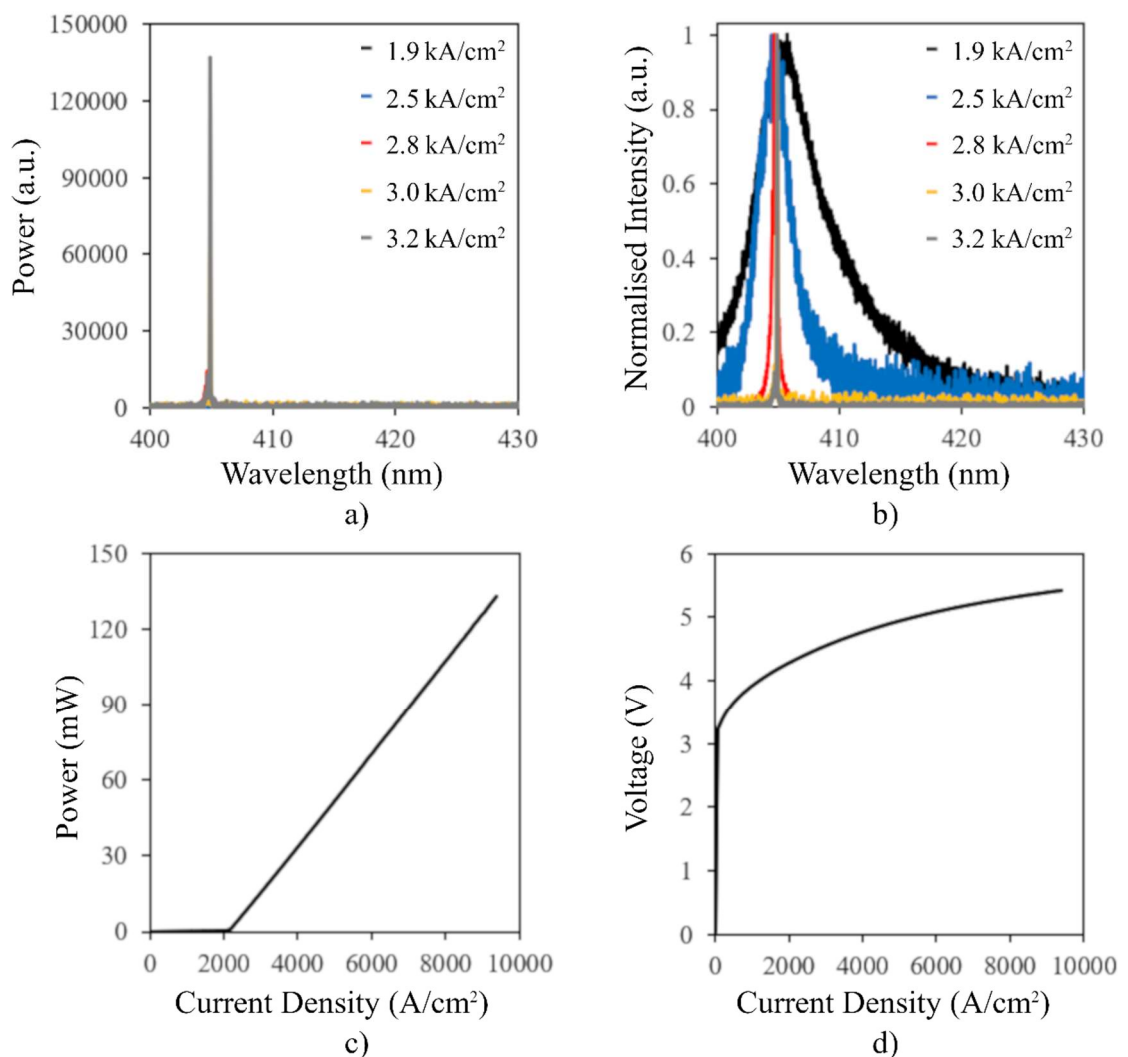


Figure 2-4 GaN laser diode a) emission spectra for various applied current densities b) normalised emission spectra for various applied current densities c) optical output power for injected current density and d) voltage for injected current density

Figure 2-4a) plots emission spectra as a function of wavelength for different levels of injected current applied to the device approaching, 1.9kA/cm^2 , and above, 2.5, 2.8, 3.0, and 3.2kA/cm^2 , lasing threshold. Figure 2-4b) plots the emission spectra from Figure 2-4a), normalised. As the current density is increased above threshold, the FWHM of the device decreases rapidly and the central wavelength, λ_0 , undergoes a further, more minor, blueshift. Figure 2-4c) plots optical output power as a function of current density. As seen earlier in Figure 2-3c), as the current density increases optical output power also increases, with super-linearity observed continuing to $\sim 10\text{kA/cm}^2$. Figure 2-4d) plots voltage as a function of current density for a device from Figure 2-3d), over an extended range.

2.5 Commercial GaN Laser Diode Contact Segmentation

Figure 2-5a) shows a schematic of a FIB system. At the top of the column there is a liquid metal ion source (LMIS) of gallium, held in a reservoir with a tungsten needle at the base [73]. LMIS are favourable for use within FIB systems due to their high current density ion beam with small energy spread [74-76], as well as options to use sources such as gallium, indium, bismuth, silicon, or gold [73,77]. However, plasma etching tools that utilise noble gas ions are beginning to displace the incumbent. Under vacuum, the gallium is heated, causing liquid gallium to flow along the tungsten needle and collect at its tip. Gallium ions are extracted from the tip of the needle by applying a very high voltage, which also accelerates them through the system at up to 50keV [73]; with systems more often operated between $20\text{-}30\text{keV}$ [74]. The beam shape is controlled by a series of electrostatic lenses, octopoles, and apertures, that focus it onto the sample [73].

Figure 2-5b) depicts a magnified view of the FIB and the sample, illustrating the position of the SEM often incorporated into FIB systems. As the gallium ions incident on the sample displace material, known as sputtering, the SEM is used preferentially to image and align the sample to reduce damage, particularly to sensitive samples. Once the sample is correctly aligned it is tilted to 52° , placing it perpendicular to the FIB. When the beam current is low, only a small amount of material is sputtered, permitting imaging of insulating samples that

could not easily be carried out in an SEM [78, 79]. As the beam current increases, the amount of sputtered material also increases, allowing the precision milling of a sample [73-78].

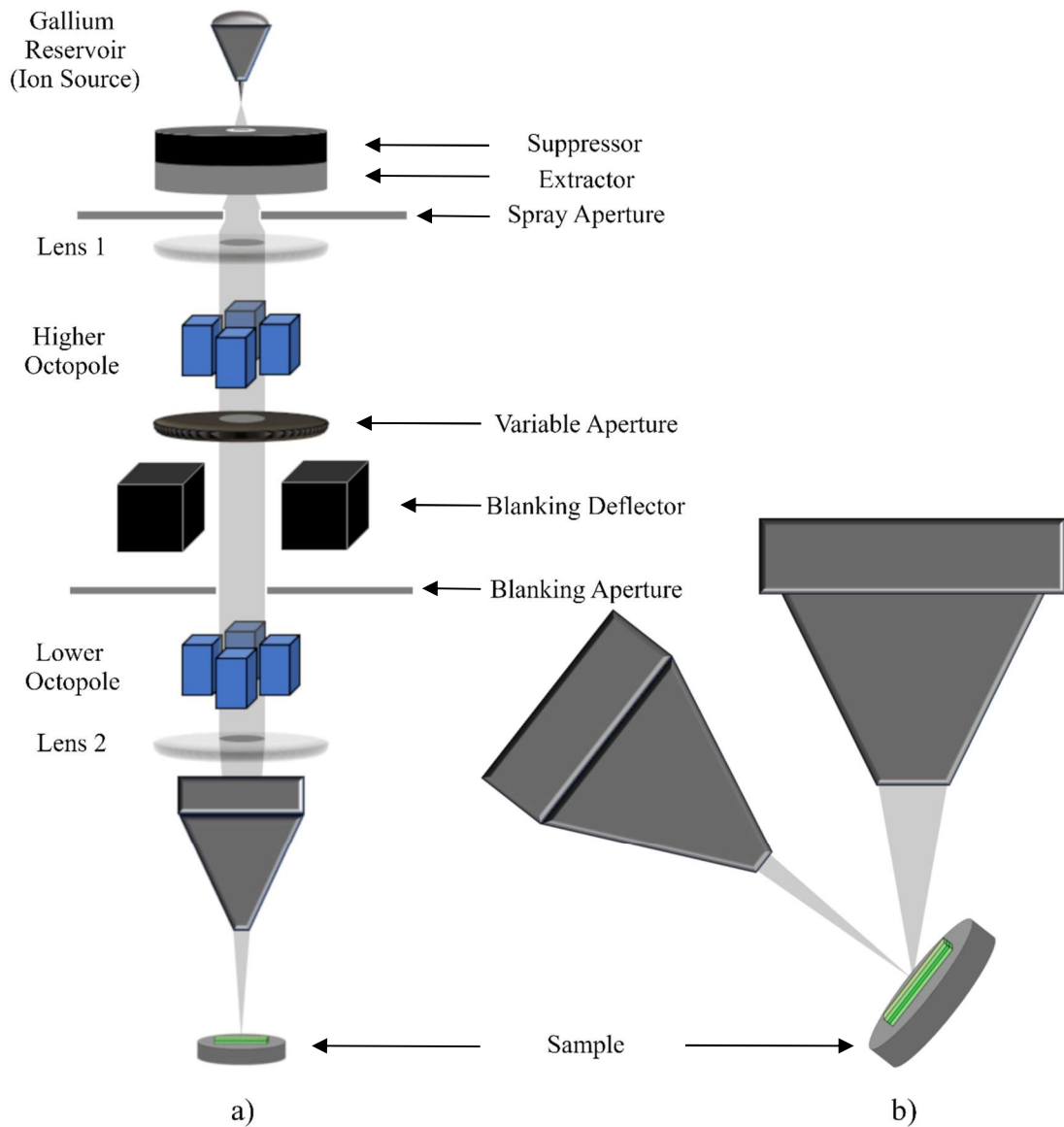


Figure 2-5 Focused ion beam a) schematic and b) magnified view

Figure 2-6a) shows an SEM image of several GaN SLEDs discussed in Chapters Three and Four. Their lengths are $\sim 2400-3000\mu\text{m}$, with ridge widths of 5, 10, 15, and $50\mu\text{m}$. Figure 2-6b) depicts a magnified SEM image of one of the GaN SLEDs shown in Figure 2-6a) taken while the device was inside the FIB system. Rather than a $50\mu\text{m}$ etch through the p^+ layer as used by Greenwood *et al.* [53], the FIB was instead used to segment the top contact of the

device. In order to minimise the level of damage inflicted upon the device during the milling process, a number of test mills were carried out on adjacent devices.

The optimal settings were a 30kV accelerating voltage and a 93pA the beam current, with a mill depth of 74.97nm. These parameters removed the top contact without causing any visible damage to the waveguide beneath, and maintained a low probability of gallium ion implantation, yet allowed the milling to be completed in good time. As the area of the device exposed to the FIB was only $\sim 40\mu\text{m}$ wide, compared to the $\sim 350\mu\text{m}$ wide device, a series of $35\mu\text{m}$ mills were carried out consecutively across the device, eventually producing two electrically isolated but optically connected sections. Figure 2-6a) shows one such $35\mu\text{m}$ mill.

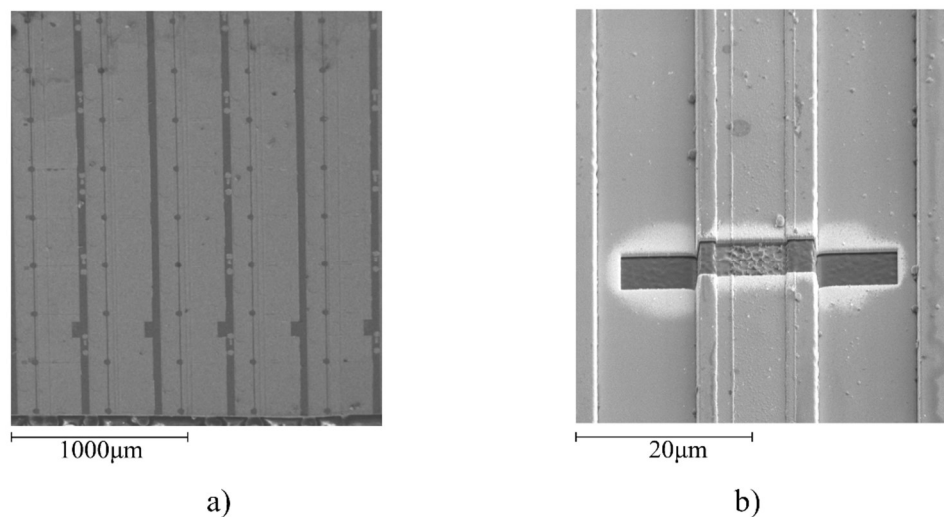


Figure 2-6 Scanning electron microscope images of a) a number of GaN SLEDs and b) the ridge and top contact of a GaN SLED during the focused ion beam milling process

Figure 2-7a) and b) show SEM images of a GaN laser diode after the FIB was used to mill the top contact, creating a passive absorber section. In order to minimise the level of damage imposed upon the device during the milling process, a number of test mills were carried out on areas of the top contact some distance from the waveguide. This created two electrically isolated but optically connected sections, separating the device into $\sim 2/3$ and $\sim 1/3$ respectively, the forwardmost section is $\sim 550\mu\text{m}$ and the rear section is $\sim 250\mu\text{m}$.

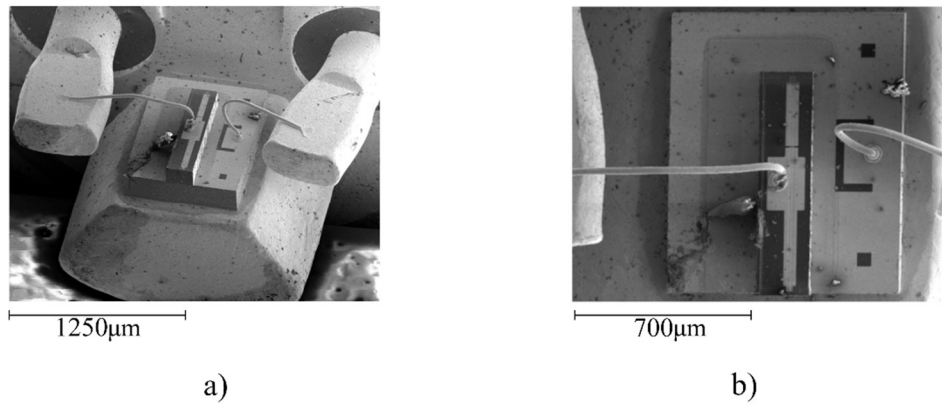


Figure 2-7 Scanning electron microscope images of a commercial laser diode after the creation of an absorber section from the a) front and b) above

Figure 2-8a) plots optical output power as a function of current density when applied to the front 2/3 of the device and the rear 1/3 is passive, or O/C. Super-linearity is observed at current densities above $\sim 2.8 \text{ kA/cm}^2$, with the lasing threshold increased from to $\sim 7.4 \text{ kA/cm}^2$.

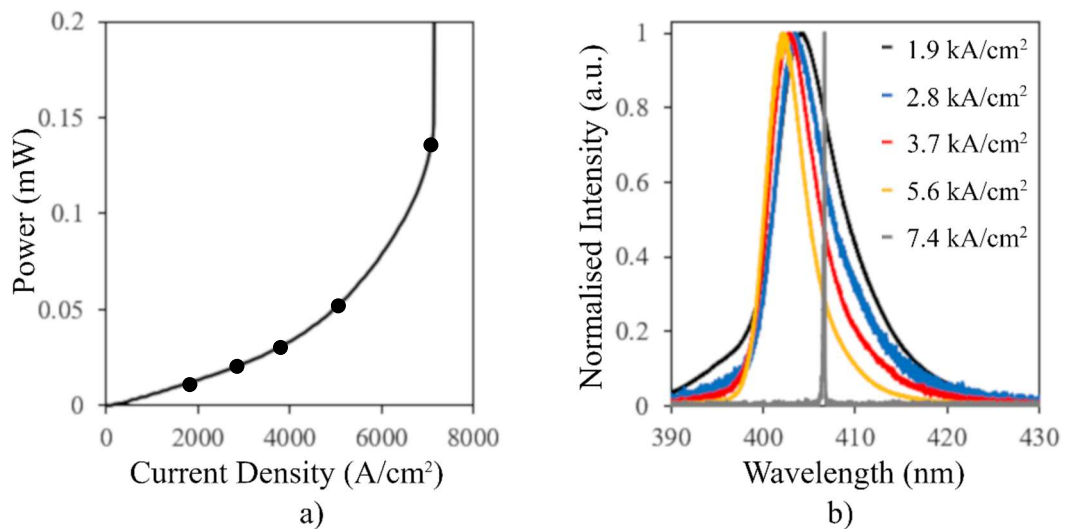


Figure 2-8 GaN laser diode following the segmentation of the top contact with the front 2/3 driven and the rear 1/3 O/C a) optical output power for injected current density and b) normalised emission spectra for various applied current densities

Figure 2-8b) plots emission spectra as a function of wavelength for different levels of injected current density. For current densities 1.9, 2.8, 3.7, and 5.6 kA/cm^2 , the observed

emission spectra are broad, smooth, and continuous, with no visible lasing peak; demonstrating that with the inclusion of the O/C absorber, a SLED has been produced. As the current density is increased and approaches 7.4kA/cm^2 , gain within the SLED overcomes the loss introduced by the absorber and lasing occurs. The device is no longer behaving as a SLED, and the desired smooth, continuous spectrum has been lost.

Figure 2-9a) plots the FWHM of the SLED produced using the FIB as a function of applied current density. As expected, as current density increases, the emission spectra narrow from $\sim 10.0\text{nm}$ to $\sim 5.2\text{nm}$. Figure 2-9b) plots predicted axial resolution as a function of current density, calculated using Equation 1-2 with the λ_0 values from Figure 2-8b), and the FWHM values from Figure 2-9a). As axial resolution is inversely proportional to the FWHM of the source, as the FWHM decreases, the magnitude of the axial resolution increases from $\sim 7.3\mu\text{m}$ to $\sim 14.3\mu\text{m}$, reducing the maximum predicted achievable resolution.

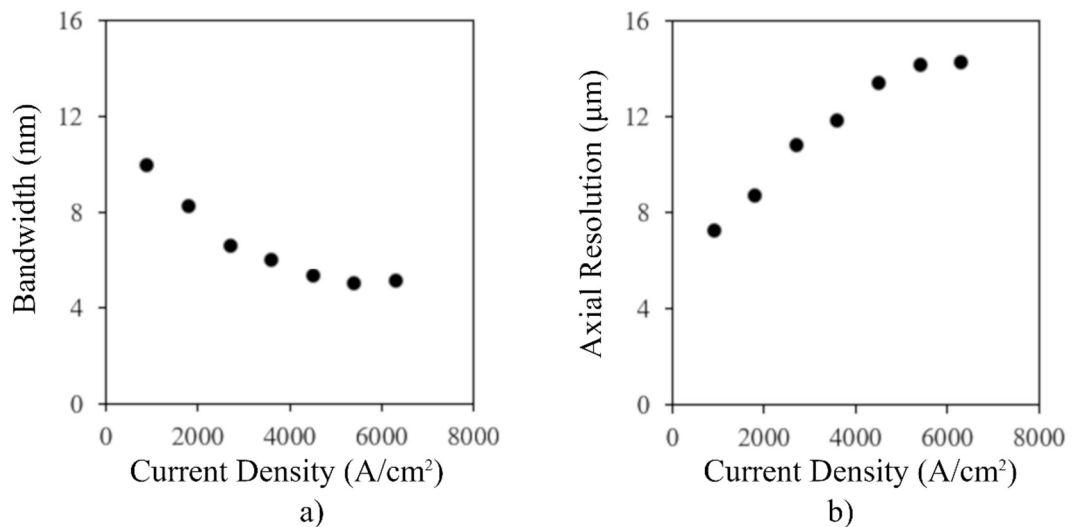


Figure 2-9 GaN laser diode following the segmentation of the top contact with the front 2/3 driven and the rear 1/3 O/C a) full width at half maximum for applied current density and b) predicted axial resolution for applied current density

2.6 Point Spread Function

Whilst the predicted axial resolution obtained using Equation 1-2 provides a value that can be used for benchmarking, only three points of the curve are utilised in the calculation, λ_0 and the two sides of the FWHM. This means that in the event the emission spectra exhibit a non-Gaussian shape, the magnitude of the predicted axial resolution is either under or overestimated [80]. Another method of predicting the axial resolution of an optical system is to obtain the PSF of the light source. The PSF expresses the response of an optical system to a light source [81] and is achieved by performing a Fourier transform [82,83] on the entirety of the emission spectrum, thereby taking any non-Gaussian behaviour into account and offering a more accurate value for axial resolution [80,81]. Figure 2-10a) plots the PSF obtained using the inverse fast Fourier transform (IFFT) function in OriginLab [84], from the emission spectra of the device shown in Figure 2-8a) and b) as a function of displacement for different values of current density, all of which were below threshold.

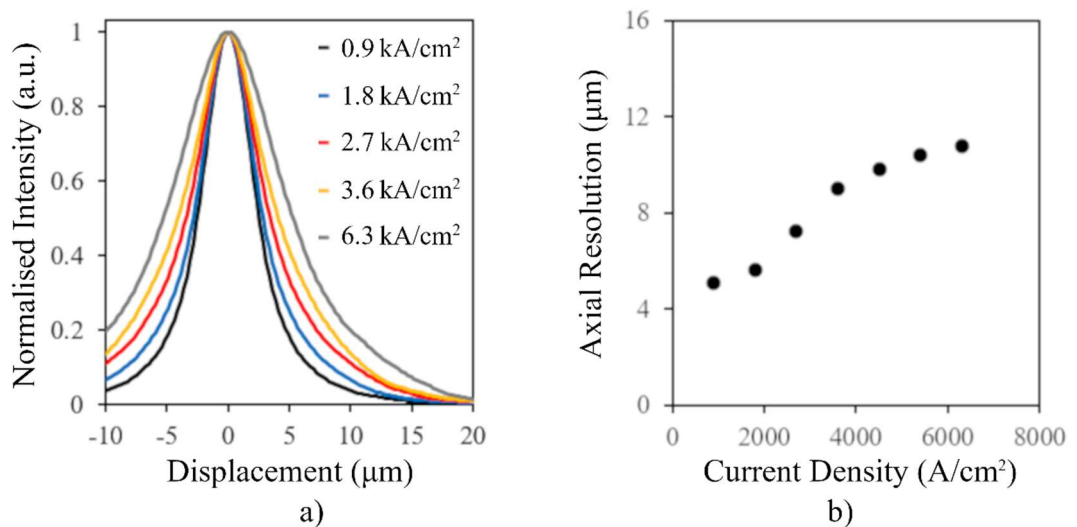


Figure 2-10 GaN laser diode following the segmentation of the top contact with the front 2/3 driven and the rear 1/3 O/C a) normalised point spread function for various applied current densities and b) predicted axial resolution for applied current density

The predicted axial resolution is determined by taking the half width at half maximum (HWHM) of the PSF. Discussed in further detail in section 2.7, this is due to the emitted

light propagating twice the distance through the sample before being incident on the detector. Figure 2-10b) plots the predicted axial resolution, taken from Figure 2-10a), as a function of current density. As expected, the magnitude of the predicted axial resolution increases as current density increases.

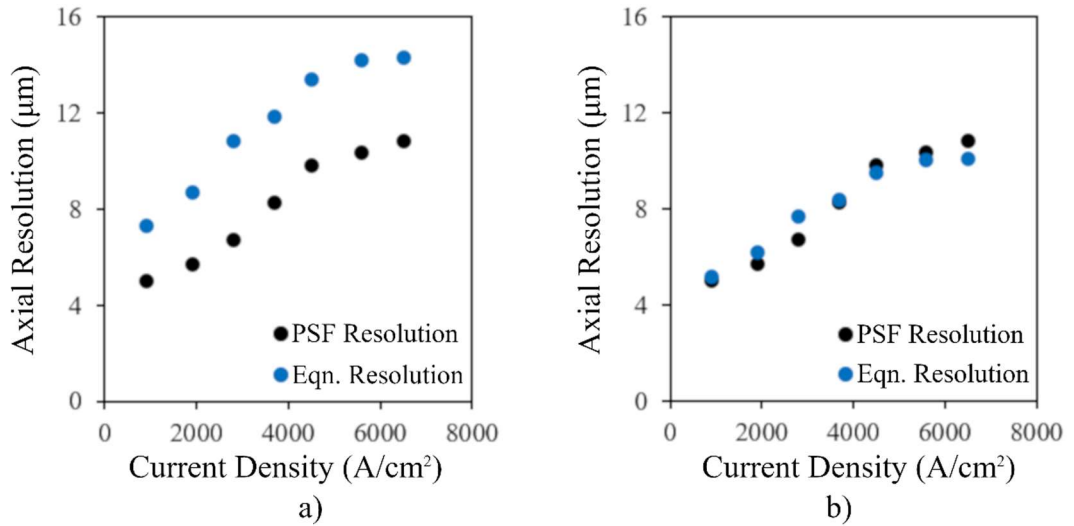


Figure 2-11 GaN laser diode following the segmentation of the top contact with the front 2/3 driven and the rear 1/3 O/C predicted axial resolution for applied current density a) as calculated and b) with values calculated using Equation 1-2 divided by $\sqrt{2}$

Figure 2-11a) plots the predicted axial resolution from Figure 2-9b), calculated using Equation 1-2, on the same axes as the predicted axial resolution plotted in Figure 2-10b), extracted from the PSF HWHM. This highlights the possible difference that can be observed between the two methods when measuring a non-Gaussian light source. Ackay *et al.*, identify that the approximated shape of the power spectral density (PSD) of the light source, Gaussian or Lorentzian, determines the coherence length and therefore the calculated resolution [80]. While Gaussian is the most commonly approximation used and gives Equation 1-2, if the PSD is assumed to be Lorentzian, Equation 1-2 becomes:

$$l_c = \sqrt{\frac{2l}{2\pi}} \times \frac{\lambda_0^2}{\Delta\lambda} \quad \text{Equation 2-2}$$

where l_c is the coherence length, or axial resolution, λ_0 is the central wavelength of the light emission, and $\Delta\lambda$ is the FWHM. Dividing the values calculated using Equation 1-2 by $\sqrt{2}$ converts them from a Gaussian approximation to a Lorentzian approximation shown in Equation 2-1. Figure 2-11b) plots the adjusted predicted axial resolution from Figure 2-9b) and the predicted axial resolution extracted from the PSF HWHM in Figure 2-10b) as a function of current density. The PSD of the device is more Lorentzian than Gaussian.

2.7 Optical Coherence Tomography

To measure the actual resolution and allow for comparison with the two methods discussed above, an OCT experimental setup was constructed. Figure 2-12a) depicts a schematic of the OCT setup. The DUT is placed some distance from the beam splitter, behind a lens. This lens, *Collimating Lens*, collimates the diverging light emitted by the DUT before it is incident on the beam splitter, a semi-reflective surface that reflects half of the light, termed beam b_1 , towards a mirror, *Mirror 1*, and transmits the other half of the light, termed beam b_2 , towards a second mirror, *Mirror 2*. *Mirror 1* is fixed in place, with *Mirror 2* mounted on a lateral translation stage, allowing the distance between *Mirror 2* and the beam splitter to be varied.

When b_1 and b_2 are reflected from *Mirror 1* and *Mirror 2* they propagate towards the beam splitter once more, where they are transmitted and reflected, respectively, towards the photodetector. Prior to the recombined light reflected from *Mirror 1* and *Mirror 2* being incident on the sensor of the photodetector, it passes through a focusing lens included to ensure that the sensor is optimally filled. The distances b_1 and b_2 travel along the OCT setup, or their path lengths, are determined by the positions of *Mirror 1* and *Mirror 2*, respectively. If both mirrors are equidistant from the beam splitter, then the path length of b_1 will be equal to the path length of b_2 , or their path length difference will be zero as b_1 and b_2 are in phase. If, when b_1 and b_2 recombine, their path length difference is zero, there will be a maximum of interference that should be detected by the photodetector. The positional resolution of the stepper motor on the translation stage was found to be similar to the period of oscillations in

the interferogram, resulting in only a small fraction of the data contained within the interferogram being detected and extracted. A sweeping, or free-running, *Mirror 2* was therefore adopted to obtain the full interferogram.

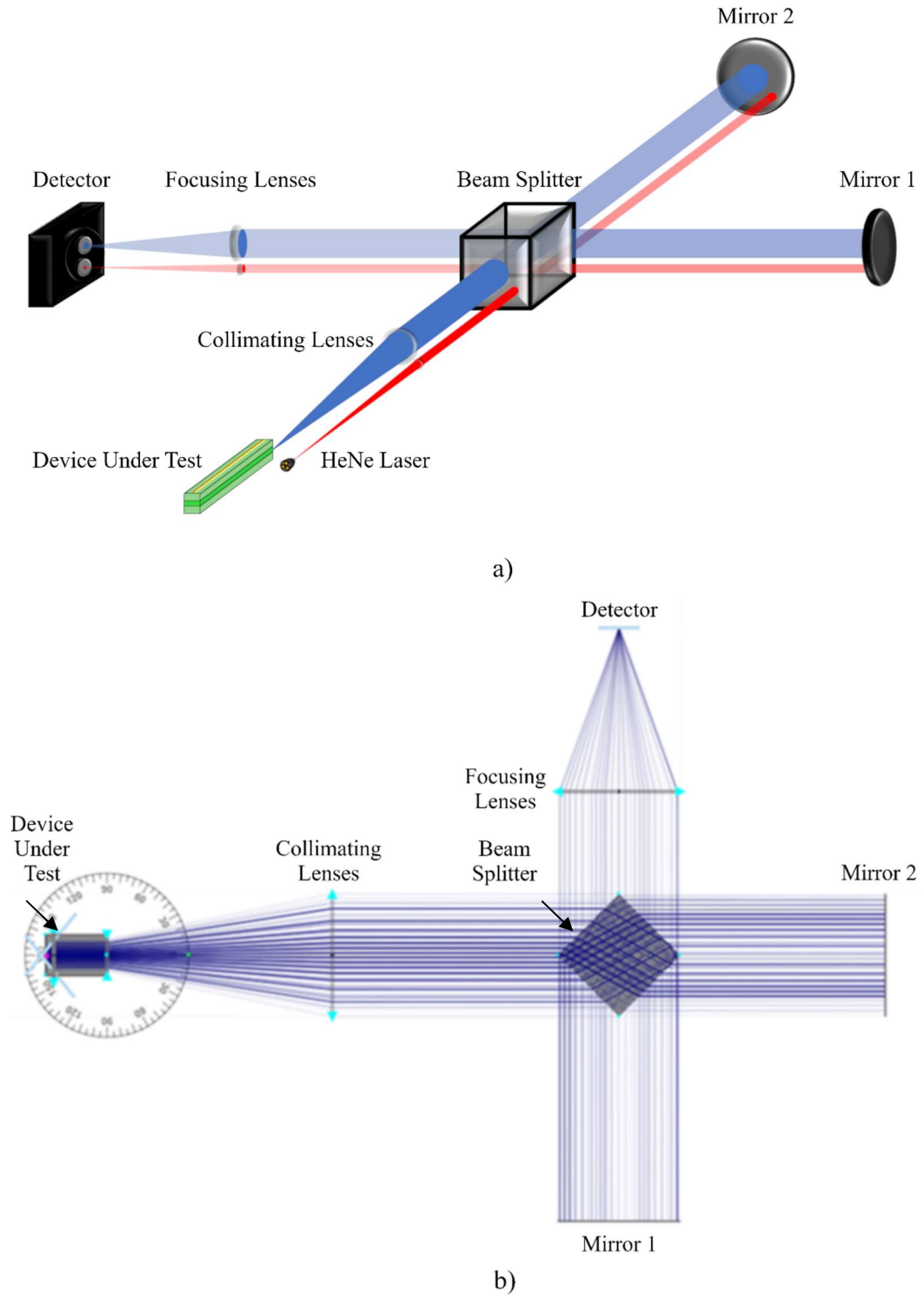
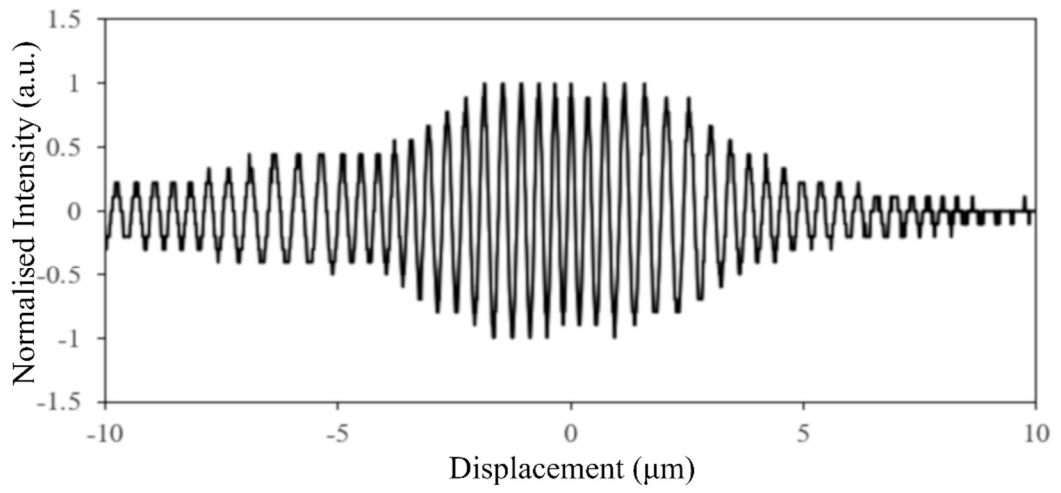


Figure 2-12 Optical coherence tomography experimental setup a) schematic and b) ray diagram

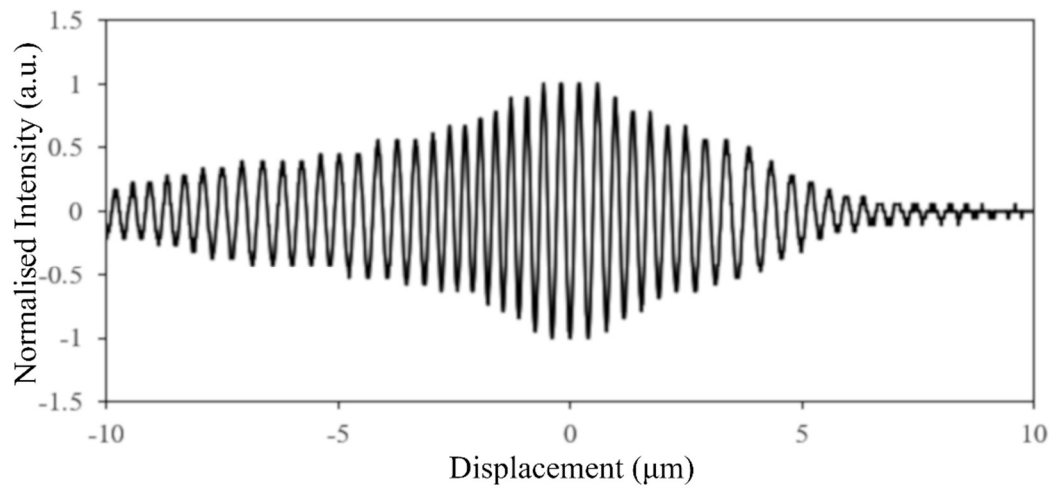
A helium neon (HeNe) laser was placed alongside the DUT, with steps taken to ensure the emitted light travelled the same path through the OCT setup as the light emitted from the DUT before it was incident on a second photodetector. By counting the number of cycles recorded by the HeNe laser photodetector during each measurement sweep, the distance travelled by light emitted from the HeNe laser can be accurately calculated. Superimposing the output from the DUT photodetector onto the output from the HeNe photodetector, the distance travelled by the light emitted from the DUT can be accurately calculated also. However, it is important to note that for every unit of distance *Mirror 2* moves away from the beam splitter, the light must travel two units of distance, as it will first propagate one unit of distance to the new position of *Mirror 2* and then propagate back to the original position of *Mirror 2* after being reflected on *Mirror 2* [80-83,85]. Hence why, for the PSFs plotted in Figure 2-10a), the predicted axial resolution is the HWHM and not the FWHM. Figure 2-12b) shows a ray diagram depicting how the light propagates from the DUT and through the OCT setup in Figure 2-12a) before it is incident on the photodetector.

Figure 2-13a), b), and c) plots normalised interferograms as a function of displacement for the device shown in Figure 2-8a) and b) for applied current densities of 1.8, 3.6, and 6.3kA/cm², respectively. When the distance calculations were performed with the output of the HeNe photodetector, they also adjusted for difference in distance that the light emitted from both the HeNe laser and DUT travelled compared to how far *Mirror 2* moved. Hence the FWHM from Figure 2-10a), b), and c) gives the actual axial resolution of the DUT, which was found to be 7.2, 7.6 and 9.1µm, respectively. As observed in Figures 2-9b), 2-10b), and 2-11a) and b), as current density increases, the magnitude of the axial resolution increases in line with the expected narrowing of device emission. These values of axial resolution are in good agreement with those obtained using the PSFs shown in Figure 2-10a), which can be obtained quickly, repeatedly, and reliably from emission spectra without the need for a second experimental setup to be constructed or a second measurement to be carried out.

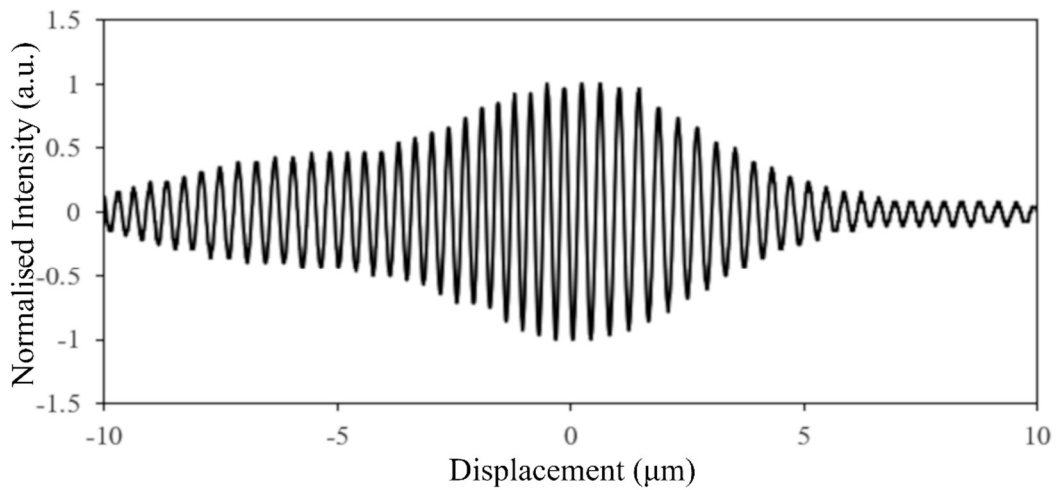
As such, any further axial resolution values will be determined from the emission spectra and subsequent PSF.



a)



b)



c)

Figure 2-13 GaN laser diode following the segmentation of the top contact with the front 2/3 driven and the rear 1/3 O/C normalised interferograms for a) 1.8kA/cm^2 , b) 3.6kA/cm^2 and c) 6.3kA/cm^2

Mirror 1 was then replaced with a microscope slide with a known, nominal thickness of $1100\mu\text{m}$ before *Mirror 2* was swept through its range of motion again. Figure 2-14 plots the normalised resulting interferogram as a function of displacement. When light is incident on the surface of the glass slide nearest to the DUT, a portion is reflected, similar to the situation before *Mirror 1* was removed. This produces the interference pattern to the left of the interferogram. The remainder of the light is transmitted through the glass slide until it is incident on the surface furthest from the DUT, where again a portion is reflected, producing the interference pattern to the right of the interferogram. The difference between these two maxima of interference is $1719\mu\text{m}$, which when divided by the refractive index of the slide of 1.518, gives a thickness of $\sim 1132\mu\text{m}$ measured using OCT. Figure 2-14 demonstrates the interferometer is capable of performing an A-scan [40-48].

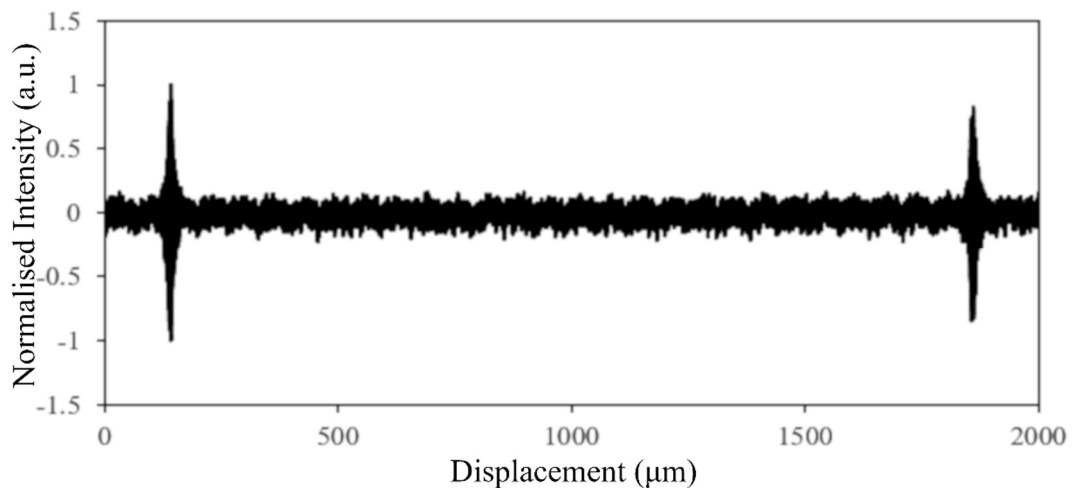


Figure 2-14 GaN laser diode following the segmentation of the top contact with the front 2/3 driven and the rear 1/3 O/C normalised interferograms with the inclusion of a glass microscope slide in place of Mirror 1

2.8 Summary

In this chapter, the feasibility of an absorber section within a GaN SLED was investigated. Commercially available laser diodes were modified using a FIB system, and an O/C absorber

was created towards the rear of the device. This demonstrated the transferability of this technique from GaAs and InP devices to GaN, and that it reliably produced a SLED.

Section 2.3 described the experimental setup and examined its suitability for conducting short wavelength measurements. Section 2.4 characterised several commercially available 405nm GaN laser diodes, demonstrated their performance below, approaching, and above lasing threshold, highlighted the uniformity of key parameters, and agreed the results with device datasheets. Section 2.5 repeated elements of the characterisation carried out in section 2.4 following the use of a FIB system to modify a number of the laser diodes to produce SLEDs, confirming minimal damage to the devices. The differences in device behaviours were analysed, and the feasibility of an absorber section within a GaN SLED was investigated. Section 2.6 introduced the PSF, discussed its merit as a measure of resolution, and compared values produced using this method to those calculated using first principles and theory. The PSF was then measured for the GaN SLED, with the PSF providing the expected maximum resolution achievable should the device be deployed in an OCT system, with resolutions between $\sim 4.5\mu\text{m}$ and $\sim 11\mu\text{m}$ reported. Section 2.7 described the construction and operation of an OCT experimental setup, or an interferometer, which confirmed that the PSF can be accurately determined from the emission spectrum. The interferometer was then used to demonstrate OCT metrology measurements with a GaN SLED for the first time.

2.9 Further Work

Having demonstrated proof of concept and a novel application for GaN SLEDs, the next step in the development process would be to attempt to increase the optical output power, and explore the imposition of different bias conditions on the absorber section; in particular, short-circuit operation. As output power is related to waveguide length [36,50,60,85-87] longer SLEDs should give rise to higher powers. Fabricating bespoke GaN SLEDs would allow control over the length of the waveguide and ensure suitable access to the absorber to connect it to ground.

References

- [01] J I Pankove, E A Miller, D Richman and J E Berkeyheiser, "Electroluminescence in GaN", *Journal of Luminescence*, **4**, Number 1, pp63-66, July 2002.
- [02] J I Pankove, E A Miller and J E Berkeyheiser, "GaN Blue Light Emitting Diodes", *Journal of Luminescence*, **5**, Number 1, pp84-86, March 1972.
- [03] J I Pankove, E A Miller and J E Berkeyheiser, *Electron Devices Meeting*, **17**, pp78, 1971.
- [04] R Dingle, K L Shaklee, R F Leheny and R B Zetterstrom, "Stimulated Emission and Laser Action in Gallium Nitride", *Applied Physics Letters*, **19**, Number 1, pp5-7, July 1971.
- [05] H P Maruska and D A Stevenson, "Violet Luminescence of Mg-Doped GaN", *Applied Physics Letters*, **22**, Number 6, pp303-305, March 1973.
- [06] H P Maruska, W C Rhines and D A Stevenson, "Preparation of Mg-Doped GaN Diodes Exhibiting Violet Electroluminescence", *Materials Research Bulletin*, **7**, Number 8, pp777-781, August 1972.
- [07] S Yoshida, S Misawa and S Gonda, "Improvements on the Electrical and Luminescent Properties of Reactive Molecular Beam Epitaxially Grown GaN Films by Using AlN-Coated Sapphire Substrates", *Applied Physics Letters*, **42**, Number 5, pp427-429, December 1982.
- [08] H Amano, N Sawaki, I Akasaki and Y Toyoda, "Metalorganic Vapor Phase Epitaxial Growth of a High Quality GaN Film Using an AlN Buffer Layer", *Applied Physics Letters*, **48**, Number 5, pp353-355, December 1985.
- [09] K Hiramatsu, S Itoh, H Amano, I Akasaki, N Kuwano, T Shiraishi and K Oki, "Growth Mechanism of GaN Grown on Sapphire with AlN Buffer Layer by MOVPE", *Journal of Crystal Growth*, **115**, Numbers 1-4, pp628-633, December 1991.
- [10] S Nakamura, "GaN Growth Using GaN Buffer Layer", *Japanese Journal of Applied Physics*, **30**, Number 10A, pp1705-1707, October 1991.
- [11] S Nakamura, Y Harada and M Seno, "Novel Metalorganic Chemical Vapor Deposition System for GaN Growth", *Applied Physics Letters*, **58**, Number 18, pp2021-2023, February 1991.

- [12] H Amano, I Akasaki, T Kozawa, K Hiramatsu, N Sawaki, K Ikeda and Y Ishii, "Electron Beam Effects on Blue Luminescence of Zinc-Doped GaN", *Journal of Luminescence*, **40-41**, pp121-122, February 1988.
- [13] H Amano, M Kito, K Hiramatsu and I Akasaki, "P-Type Conduction in Mg-Doped GaN Treated with Low-Energy Electron Beam Irradiation (LEEBI)", *Japanese Journal of Applied Physics*, **28**, Number 12, pp2112-2114, December 1989.
- [14] S Nakamura, M Senoh and T Mukai, "Highly P-Typed Mg-Doped GaN Films Grown with GaN Buffer Layers", *Japanese Journal of Applied Physics*, **30**, Number 10A, pp1708-1711, October 1991.
- [15] S Nakamura, T Mukai and M Senoh, "High-Power GaN P-N Junction Blue Light-Emitting Diodes", *Japanese Journal of Applied Physics*, **30**, Number 12A, pp1998-2001, December 1991.
- [16] S Nakamura, M Senoh and T Mukai, "High-Power InGaN/GaN Double-Heterostructure Violet Light Emitting Diodes", *Applied Physics Letters*, **62**, Number 19, pp2390-2392, May 1993.
- [17] S Nakamura, M Senoh and T Mukai, "P-GaN/N-InGaN/N-GaN Double-Heterostructure Blue-Light-Emitting Diodes", *Japanese Journal of Applied Physics*, **32**, Numbers 1A-B, pp8-11, January 1993.
- [18] S Nakamura, M Senoh, S Nagahama, N Iwasa, T Yamada, T Matsushita, H Kiyoku and Y Sugimoto, "InGaN-Based Multi-Quantum-Well-Structure Laser Diodes", *Japanese Journal of Applied Physics* **35**, Number 1B, pp74-76, January 1996.
- [19] S Nakamura and T Mukai, "High-Quality InGaN Films Grown on GaN Films", *Japanese Journal of Applied Physics*, **31**, Number 10B, pp1457-1459, October 1992.
- [20] S Nakamura, T Mukai and M Senoh, "Candela-Class High-Brightness InGaN/AlGaN Double-Heterostructure Blue-Light-Emitting Diodes", *Applied Physics Letters*, **64**, Number 13, pp1687-1689, March 1994.
- [21] S Nakamura, T Mukai and M Senoh, "High-Brightness InGaN/AlGaN Double-Heterostructure Blue-Green-Light-Emitting Diodes", *Journal of Applied Physics*, **76**, Number 12, pp8189-8191, December 1994.
- [22] S Nakamura, M Senoh, N Iwasa, S Nagahama, T Yamada and T Mukai, "Super-Bright Green InGaN Single-Quantum-Well-Structure Light-Emitting Diodes", *Japanese Journal of Applied Physics*, **34**, Number 10B, pp1332-1335, October 1995.

- [23] I Akasaki, H Amano, S Sota, H Sakai, T Tanaka and M Koike, "Stimulated Emission by Current Injection from an AlGaIn/GaN/GaInN Quantum Well Device", Japanese Journal of Applied Physics, **34**, Number 11B, pp1517-1519, November 1995.
- [24] S Nakamura, M Senoh, S Nagahama, N Iwasa, T Yamada, T Matsushita, H Kiyoku, Y Sugimoto, "InGaIn Multi-Quantum-Well-Structure Laser Diodes with Cleaved Mirror Cavity Facets", Japanese Journal of Applied Physics, **35**, Number 2B, pp217-220, February 1996.
- [25] S Nakamura, M Senoh, S Nagahama, N Iwasa, T Yamada, T Matsushita, Y Sugimoto and H Kiyoku, "Continuous-Wave Operation of InGaIn Multi-Quantum-Well-Structure Laser Diodes at 233K", Applied Physics Letters, **69**, Number 20, pp3034-3036, November 1996.
- [26] S Nakamura, M Senoh, S Nagahama, N Iwasa, T Yamada, T Matsushita, Y Sugimoto and H Kiyoku, "Room-Temperature Continuous-Wave Operation of InGaIn Multi-Quantum-Well Structure Laser Diodes", Applied Physics Letters, **69**, Number 26, pp4056-4058, December 1996.
- [27] S Nakamura, M Senoh, S Nagahama, N Iwasa, T Yamada, T Matsushita, Y Sugimoto and H Kiyoku, "Room-Temperature, Continuous-Wave Operation of InGaIn Multi-Quantum-Well Structure Laser Diodes with a Lifetime of 27 Hours", Applied Physics Letters, **70**, Number 11, pp1417-1419, March 1997.
- [28] S Nakamura, M Senoh, S Nagahama, N Iwasa, T Yamada, T Matsushita, Y Sugimoto and H Kiyoku, "High-Power, Long-Lifetime InGaIn Multi-Quantum-Well-Structure Laser Diodes", Japanese Journal of Applied Physics, **36**, Number 8B, pp1059-1061, August 1997.
- [29] S Nakamura, M Senoh, S Nagahama, N Iwasa, T Yamada, T Matsushita, H Kiyoku, Y Sugimoto, T Kozaki, H Umemoto, M Sano and K Cocho, "High-Power, Long-Lifetime InGaIn/GaN/AlGaIn-Based Laser Diodes Grown on Pure GaN Substrates", Japanese Journal of Applied Physics, **37**, Number 3B, pp309-312, March 1998.
- [30] Nichia, "Violet Laser Diode", NDV4316 datasheet, January 2013.
- [31] S Nakamura, "III-V Nitride Based Light Emitting Devices", Solid State Communications, **102**, Number 2-3, pp237-248, 1997.
- [32] S Nakamura and M R Krames, "History of Gallium-Nitride-Based Light-Emitting Diodes for Illumination", Proceedings of the IEEE, **101**, Number 10, pp2211-2220, October 2013.

- [33] U T Schwarz, F Kopp, T Weig, C Eichler and U Strauss, "Superluminescent Light Emitting Diodes of 100mW Output Power for Pico-Projection", Conference on Lasers and Electro-Optics Pacific Rim (CLEO-PR), pp1-2, June 2013.
- [34] F Kopp, C Eichler, A Lell, S Tautz, J Ristic, B Stojetz, C Hoss, T Weig, U T Schwarz and U Strauss, "Blue Superluminescent Light-Emitting Diodes with Output Power Above 100mW for Picoprojection", Japanese Journal of Applied Physics, **52**, pp08JH07-1-5, 2013.
- [35] H Ohno, K Orita, M Kawaguchi, K Yamanaka and S Takigawa, "200mW GaN-Based Superluminescent Diode with a Novel Waveguide Structure", IEEE Photonics Conference, pp505-506, October 2011.
- [36] A Kafar, S Stanczyk, S Grzanka, R Czernecki, M Leszczynski, T Suski and P Perlin, "Cavity Suppression in Nitride Based Superluminescent Diodes", Journal of Applied Physics, **111**, pp083106-1-6, 2012.
- [37] K Holc, L Marona, R Czernecki, M Bockowski, T Suski, S Najda and P Perlin, "Temperature Dependence of Superluminescence in InGaN-Based Superluminescent Light Emitting Diode Structures", Journal of Applied Physics, **108**, pp013110-1-4, 2010.
- [38] E Feltin, A Castiglia, G Cosendey, L Sulmoni, J F Carlin, N Grandjean, Rossetti, J Dorsaz, V Laino, M Duelk and C Velez, "Broadband Blue Superluminescent Light-Emitting Diodes Based on GaN", Applied Physics Letters, **95**, pp081107-1-3, August 2009.
- [39] M Rossetti, J Dorsaz, R Rezzonico, M Duelk, C Velez, E Feltin, A Castiglia, G Cosendey, J F Carlin and N Grandjean, "High Power Blue-Violet Superluminescent Light Emitting Diodes with InGaN Quantum Wells", Applied Physics Express, **3**, pp061002-1-3, 2010.
- [40] D Huang, E A Swanson, C P Lin, J S Schuman, W G Stinson, W Chang, M R Hee, T Flotte, K Gregory, C A Puliafito and J G Fujimoto, "Optical Coherence Tomography", Science, **254**, Number 5035, pp1178-1181, November 1991.
- [41] A F Fercher, W Drexler, C K Hitzenberger and T Lasser, "Optical Coherence Tomography - Principles and Applications", Reports on Progress in Physics, **66**, Number 2, pp239-303, February 2003.
- [42] J M Schmitt, "Optical Coherence Tomography (OCT) - A Review", IEEE Journal of Selected Topics in Quantum Electronics, **5**, Number 4, pp1205-1215, August 1999.
- [43] A Gh Podoleanu, "Optical Coherence Tomography", Journal of Microscopy, **247**, Number 3, pp209-219, September 2012.

- [44] W Drexler, "Ultrahigh-resolution Optical Coherence Tomography", *Journal of Biomedical Optics*, **9**, Number 1, pp47-74, February 2004.
- [45] A Unterhuber, B Povazay, K Bizheva, B Hermann, H Sattmann, A Stingl, T Le, M Seefeld, R Menzel, M Preusser, H Budka, Ch Schubert, H Reitsamer, P K Ahnelt, J E Morgan, A Cowey and W Drexler, "Advances in Broad Bandwidth Light Sources for Ultrahigh Resolution Optical Coherence Tomography," *Physics in Medicine and Biology*, **49**, pp1235-1246, March 2004.
- [46] A D Aguirre, P Hsiung, T H Ko, I Hartl and J G Fujimoto, "High-Resolution Optical Coherence Microscopy for High-Speed, in vivo Cellular Imaging," *Optics Letters*, **28**, Number 21, pp 2064-2066, November 2003.
- [47] W Drexler, U Morgner, R K Ghanta, F X Kartner, J S Schuman and J G Fujimoto, "Ultrahigh-Resolution Ophthalmic Optical Coherence Tomography," *Nature Medicine*, **7**, Number 4, pp502-507, April. 2001.
- [48] V R Shidlovski, "*Optical Coherence Tomography*," 2nd Edition. W Drexler and J G Fujimoto, Editors., Springer International Publishing, 2008, pp505-617.
- [49] T P Lee, C A Burrus Jr and B I Miller, "A Stripe Geometry Double-Heterostructure Amplified-Spontaneous-Emission (Superluminescent) Diode", *Journal of Quantum Electronics*, **9**, Number 8, pp820-828, August 1973.
- [50] G A Alphonse, D B Gilbert, M G Harvey and M Ettenberg, "High-Power Superluminescent Diodes", *Journal of Quantum Electronics*, **24**, Number 12, pp2454-2457, December 1988.
- [51] Z Y Zhang, I J Luxmoore, C Y Jin, H Y Liu, Q Jiang, K M Groom, D T Childs, M Hopkinson, A G Cullis and R A Hogg, "Effect of Facet Angle on Effective Facet Reflectivity and Operating Characteristics of Quantum Dot Edge Emitting Lasers and Superluminescent Light Emitting Diodes", *Applied Physics Letters*, **91**, pp081112-1-3, August 2007.
- [52] P D L Judson, K M Groom, D T D Childs, M Hopkinson and R A Hogg, "Multi-Section Quantum Dot Superluminescent Diodes for Spectral Shape Engineering", *IET Optoelectronics*, **3**, Number 2, pp100-104, November 2008.
- [53] R A Hogg, P D L Greenwood, D T D Childs, N Krstajic, K Kennedy, K M Groom, M Hugues, M Hopkinson, L E Smith, S J Matcher, M Bonesi, S Macneil and R Smallwood, "GaAs Based Quantum Dot Superluminescent Diodes for Optical

- Coherence Tomography of Skin Tissue", International Conference on Computers and Devices for Communication, pp1-6, December 2009.
- [54] N S K Kwong, K Y Lau, N Bar-Chaim, I Ury and K J Lee, "High-Power, High Efficiency Window Buried Heterostructure GaAlAs Superluminescent Diode with Integrated Absorber", Applied Physics Letters, **51**, Number 23, pp1879-1881, December 1987.
- [55] S A Safin, A T Semenov, V R Shidlovski, N A Zhuchkov and Y V Kurnyavko, "High-Power 0.82 μ m Superluminescent Diodes with Extremely Low Fabry-Perot Modulation Depth", Electronics Letters, **28**, Number 2, pp127-129, January 1992.
- [56] A T Semenov, V R Shidlovski, S A Safin, V P Konyaev and M V Zverkov, "Superluminescent Diodes for Visible (670nm) Spectral Range Based on AlGaInP/GaInP Heterostructures with Tapered Grounded Absorber", Electronics Letters, **29**, Number 6, pp530-532, March 1993.
- [57] A T Semenov, V K Batovrin, I A Garmash, V R Shidlovsky, M V Shramenko and S D Yakubovich, "(GaAl)As SQW Superluminescent Diodes with Extremely Low Coherence Length", Electronics Letters, **31**, Number 4, pp314-315, February 1995.
- [58] A T Semenov, V R Shidlovski, D A Jackson, R Willsch and W Ecke, "Spectral Control in Multisection AlGaAs SQW Superluminescent Diodes at 800nm", Electronics Letters, **32**, Number 3, pp255-256, February, 1996.
- [59] N S K Kwong, K Y Lau and N Bar-Chaim, "High-Power High-Efficiency GaAlAs Superluminescent Diodes with an Internal Absorber for Lasing Suppression", Journal of Quantum Electronics, **25**, Number 4, pp696-704, April 1989.
- [60] A Kafar, S Stanczyk, G Targowski, T Oto, I Makarowa, P Wisinieski, T Suski and P Perlin, "High-Optical-Power InGaN Superluminescent Diodes with "j-shape" Waveguide", Applied Physics Express, **6**, pp092102-1-4, 2013.
- [61] F Kopp, T Lermer, C Eichler and U Strauss, "Cyan Superluminescent Light-Emitting Diode Based on InGaN Quantum Wells", Applied Physics Express, **5**, pp082105-1-3, 2012.
- [62] Newport, "Application Note 1 - Fiber Optics and Photonics - Test and Characterization of Laser Diodes: Determination of Principal Parameters", K S Mobarhan.
- [63] SPEX, "Instructions 1702/1704 Spectrometer", 1995.
- [64] C S Williams and O A Becklund, "Optics: A Short Course for Engineers and Scientists", Wiley, 1972.

- [65] Ocean Optics, "HG-1 Mercury Argon Calibration Light Source - Installation and Operation Instructions".
- [66] S G Rautian, "Real Spectral Apparatus", *New Apparatus and Methods of Measurement*, Soviet Physics USPEKHI, **66**, Number 2, pp245-273, November 1958.
- [67] L A Coldren, S W Corzine and M L Masanovic, "Diode Lasers and Photonic Integrated Circuits", 2nd Edition, Wiley, 2012.
- [68] W H Guo, D Byrne, Q Lu, B Corbett and J F Donegan, "Fabry-Perot Laser Characterization Based on the Amplified Spontaneous Emission Spectrum and the Fourier Series Expansion Method", *IEEE Journal of Selected Topics in Quantum Electronics*, **17**, Number 5, pp1356-1363, September 2011.
- [69] J C Johnson, H J Choi, K P Knutsen, R D Schaller, P Yang and R J Saykally, "Single Gallium Nitride Nanowire Lasers", *Nature Materials Letters*, **1**, pp106-110, September 2002.
- [70] Opnext, "Low Operating Current Visible Laser Diode", HL6362MG/63MG datasheet, August 2008.
- [71] Mitsubishi, 1550, 1520nm InGaAsP FP Laser Diodes", ML9xx45 Series datasheet, May 2004.
- [72] Osram, Blue Laser Diode in TO38 ICut Package", PL450B datasheet, October 2013.
- [73] L A Giannuzzi and F A Stevie, "A Review of Focused Ion Beam Milling Techniques for TEM Specimen Preparation", *Micron*, **30**, pp197-204, 1999.
- [74] B I Prenitzer, L A Giannuzzi, K Newman, S R Brown, R B Irwin, T L Shofner and F A Stevie, "Transmission Electron Microscope Specimen Preparation of Zn Powders Using the Focused Ion Beam Lift-Out Technique", *Metallurgical and Materials Transactions A*, **29A**, pp2399-2406, September 1998.
- [75] M Saito, T Aoyama, T Hashimoto and S Isakozawa, "Transmission Electron Microscope Sample Shape Optimization for Energy Dispersive X-Ray Spectroscopy Using the Focused Ion Beam Technique", *Japanese Journal of Applied Physics*, **37**, pp335-359, January 1998.
- [76] M H F Overwijk, F C van den Heuvel and C W T Bulle-Lieuwma, "Novel Scheme for the Preparation of Transmission Electron Microscopy Specimens with a Focused Ion Beam", *Journal of Vacuum Science and Technology B*, **11**, Number 6, pp2021-2-24, November 1993.
- [77] M Tarutani, Y Takai and R Shimizu, "Application of the Focused-Ion-Beam Technique for Preparing the Cross-Sectional Sample of Chemical Vapor Deposition

- Diamond Thin Film for High-Resolution Transmission Electron Microscope Observation”, Japanese Journal of Applied Physics, **31**, pp1305-1308, September 1992.
- [78] R Hull, F A Stevie and D Bahnck, “Observation of Strong Contrast from Doping Variations in Transmission Electron Microscopy of InP-based Semiconductor Laser Diodes”, Applied Physics Letters, **66**, Number 3, pp341-343, January 1995.
- [79] L A Giannuzzi, J L Drown, S R Brown, R B Irwin and F A Stevie, “Focused Ion Beam Milling for Site Specific Scanning and Transmission Electron Microscopy Specimen Preparation”, Microscopy Society of America 55th Annual Meeting, **3**, Number 2, pp347-348, August 1997.
- [80] C Akcay, P Parrein and J P Rolland, “Estimation of Longitudinal Resolution in Optical Coherence Imaging,” *Applied Optics*, Vol. 41, No. 25, pp5256-5262, Sep. 2002.
- [81] A C Akcay, J P Rolland and J M Eichenholz, “Spectral Shaping to Improve the Point Spread Function in Optical Coherence Tomography,” *Optics Letters*, Vol. 28, No. 20, pp1921-1923, Oct. 2003.
- [82] S W Lee, H W Jeong, B M Kim, Y C Ahn, W Jung and Z Chen, “Optimization for Axial Resolution, Depth Range, and Sensitivity of Spectral Domain Optical Coherence Tomography at 1.3 μ m”, Journal of the Korean Physical Society, Vol. 55, No.6, pp2354-2360, December 2009.
- [83] J A Izatt and M A Choma, “*Optical Coherence Tomography*,” 2nd Edition. W Drexler and J G Fujimoto, Editors., Springer International Publishing, 2008, pp47-72
- [84] <https://www.originlab.com/doc/Origin-Help/IFFT>
- [85] M Rossetti, J Napierala, N Matuschek, U Achattz, M Duelk, C Velez, A Castiglia, N Grandjean, A Dorsaz and E Feltn, “Superluminescent Light Emitting Diodes – The Best Out of Two Worlds”, Proceedings of SPIE, Volume 8252, February 2012.
- [86] C Zeng, S Zhang, J Liu, D Li, D Jiang, M Feng, Z Li, K Zhou, F Wang, H Wang, H Wang and H Yang, “Characteristics of InGaN-based Superluminescent Diodes with One-sided Oblique Cavity Facet”, Chinese Scientific Bulletin, **59**, pp1903-1906, October 2012.
- [87] A Kafar, S Stanczyk, P Wisniewski, T Oto, I Makarowa, G Targowski, T Suski and P Perlin, “Design and Optimization of InGaN Superluminescent Diodes”, Physica Status Solidi A, **212**, Number 5, pp997-1004, September 2014.

Chapter Three - The Effect of Absorbers on GaN SLED Performance

3.1 Introduction to Chapter

Conventional and gallium nitride (GaN) superluminescent light emitting diodes (SLEDs) [01,02] are introduced in Chapter One, which describes and explains the key differences in their design, operation, and performance compared to laser diodes [03].

Since they were first disclosed in 1973 by Lee *et al.*, [01] SLEDs were quickly identified as suitable light sources for use in fibre optic gyroscopes (FOGs) [04,05], pico-projection [06,07], and optical coherence tomography (OCT) applications. Even though GaN SLEDs were not reported by Feltin *et al.*, [02] until 2009 due to the complexities around growing and doping GaN as discussed in section 1.8 in Chapter One; considerable effort has been spent on rapidly improving their performance to bring it in line with conventional SLEDs. Techniques such as applying anti-reflection (AR) coatings [08], using angled facets or waveguides [09], using bent, or j shape, waveguides [10], absorber sections [11], windows [12], or a combination of these techniques [08-12], have been demonstrated to be methods of suppressing optical feedback readily transferrable to GaN SLEDs [02,03,06,07,13-17].

Although applications for SLEDs include FOGs and OCT, the main impetus for GaN SLEDs has been for pico-projection [06,07]. This is due to SLEDs addressing the shortcomings observed when either lasers or light emitting diodes (LEDs) were used for pico-projection. Lasers emit at practically a singular wavelength, meaning that when the emitted light is incident on the surface being used to display the projected image, constructive and destructive interference occurs due to the time coherence of the light [18]. This interference manifests itself as fluctuations of image brightness and is termed speckle. As speckle is

inversely proportional to the spectral bandwidth of the light source, image quality and clarity improves as bandwidth broadens [06]. LEDs, while offering broad bandwidth, have low power densities which is perceived by the consumer as low brightness, and low directionality [18]. With GaN SLEDs offering high power densities and high directionality coupled with modest ($\sim 5\text{nm}$) bandwidths [06,07], they were quickly adopted for use in pico-projectors with research focusing almost exclusively on ever-increasing output powers [13,17], with 200mW [16,19], 250mW [20], and 350mW [21] achieved in only a few years.

In the pursuit of high output powers, the techniques of suppressing optical feedback [08-12] were limited to preventing lasing, rather than increasing the full width at half maximum (FWHM), or bandwidth, of the emission. As such, whenever device designs and geometries are discussed, those featuring absorber sections are often dismissed in favour of tilted or bent waveguides [22]. This has led to mature device designs, such as those with bent waveguides, being repurposed in attempts to broaden emission bandwidth. One such example is disclosed by Kafar *et al.*, who patterned the substrate so the indium content decreased along the SLED waveguide broadening the emission from 3.4nm in the reference device to 6.1nm [23].

The use of absorber sections within GaN SLEDs is still in its infancy, and could hold the key to both enhanced FWHMs and the wider use of the devices in applications such as OCT.

3.2 Outline of Chapter

In this chapter, the role of an absorber section within GaN SLEDs is explored further. A series of GaN laser diodes around three times longer than the commercially available laser diodes discussed in Chapter Two were fabricated in the University of Sheffield's National Centre for III-V Technologies. Producing bespoke devices allows for control over the length and width of the waveguide, facet orientations, and accessibility of absorber sections. Once characterised, absorber sections are created using a focused ion beam (FIB) system, with an option to operate them open-circuit (O/C) or short-circuit (S/C).

Section 3.3 describes the fabrication process performed to produce the GaN laser diodes and SLEDs from a 2 quantum well (QW) GaN substrate. Section 3.4 characterises GaN laser diodes and investigates the effect of increasing ridge width. Section 3.5 repeats elements of the characterisation carried out in section 3.4 following the use of a FIB system to convert the laser diodes into SLEDs, to ensure minimal damage was inflicted upon the devices. Section 3.6 examines the scenario when the absorber section of the SLED is operated in O/C, and section 3.7 when the absorber is operated in S/C. Section 3.8 reintroduces the point spread function (PSF) and extracts the predicted resolution of the devices.

This forms part of the work published in my IEEE Journal of Selected Topics in Quantum Electronics paper.

3.3 Fabrication Steps for Gallium Nitride SLEDs

A metalorganic chemical vapour deposition (MOCVD) system was used to grow 430nm indium gallium nitride (InGaN) InGaN/GaN-based SLED structures on a 2-inch freestanding c-plane GaN substrate with a dislocation density in the range of $1-5 \times 10^6/\text{cm}^2$. The epilayer stack consists of $1\mu\text{m}$ silicon (Si)-doped n-GaN ($n_d = 3 \times 10^{18}/\text{cm}^3$), a $1\mu\text{m}$ cladding layer of Si-doped aluminium gallium nitride (AlGaN) $\text{Al}_{0.07}\text{Ga}_{0.93}\text{N}$ ($n_d = 1 \times 10^{18}/\text{cm}^3$), an active region of two 4.5nm $\text{In}_{0.12}\text{Ga}_{0.88}\text{N}/\text{GaN}$ QWs, separated by an 11.5nm GaN barrier, a 20nm electron blocking layer of magnesium (Mg)-doped $\text{Al}_{0.2}\text{Ga}_{0.8}\text{N}$ ($n_d = 1 \times 10^{17}/\text{cm}^3$), 110nm Mg-doped GaN, a $0.5\mu\text{m}$ cladding layer of Mg-doped $\text{Al}_{0.06}\text{Ga}_{0.94}\text{N}$ ($n_d = 1 \times 10^{17}/\text{cm}^3$), and 50nm Mg-doped p-GaN.

The devices were fabricated using standard photolithography, and the ridge waveguides were etched below the active region using a plasma-enhanced chemical vapour deposition (PECVD), silicon dioxide (SiO_2) mask, and inductively coupled plasma reactive-ion etch (ICP-RIE) process. 300nm SiO_2 was deposited as an insulating layer by PECVD, and nickel

gold (Ni/Au) and titanium gold (Ti/Au) Ohmic contacts were deposited on the p-GaN and n-GaN layers, respectively.

Photolithography is a process that uses opaque and transparent masks, a photosensitive chemical, 'photoresist', and ultraviolet light to pattern the wafer with geometric shapes, so that after deposition material can be removed from areas it is not required at up to micron resolutions. Photoresist can be either positive or negative. Positive photoresist means that the photochemical reaction that occurs when the polymer it comprises of is exposed to light, results in the photoresist becoming soluble with the photoresist developer. Areas that have been exposed to light prior to the application of the developer will be removed preferentially compared to those that have not. Negative photoresist is the opposite to positive photoresist, meaning when it is exposed to light it is no longer soluble with the photoresist developer.

The first step of the process is to cleave and clean the wafer. As a result of the wurtzite structure of GaN, discussed in more detail in Chapter One, the substrate is unlikely to cleave at 90°, or in straight lines. Cleaning is performed using acetone, n-butyl acetate, and isopropyl alcohol (IPA) as part of a three-stage clean. This is followed by a 30 second oxygen (O₂) plasma ash, after which the wafer is soaked in a 1:1 ratio of hydrochloric acid and water for 1 minute; before being rinsed thoroughly with deionised water and dried with a nitrogen gun. These steps remove any dirt and dust particles from the surface of the wafer, as well as any oxide layers, which could otherwise interfere with the quality of deposition and ultimately affect device performance.

Figure 3-1a) depicts a 3D schematic of the GaN wafer following the cleave and clean, with Figure 3-1b) the view from the side and Figure 3-1c) the birds-eye view. The figures throughout this section show the fabrication process as if it were being carried out for 1 device for simplicity.

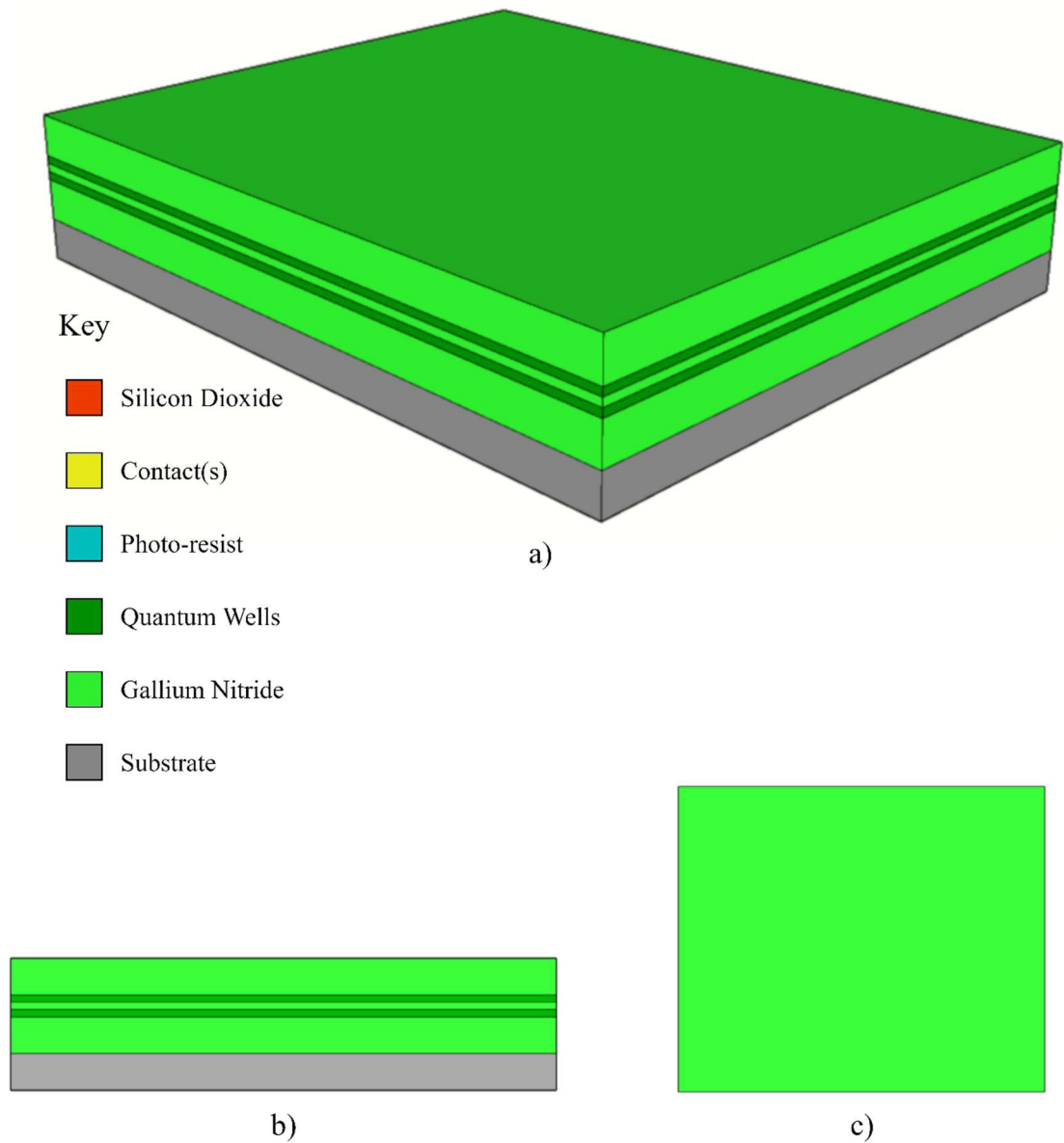
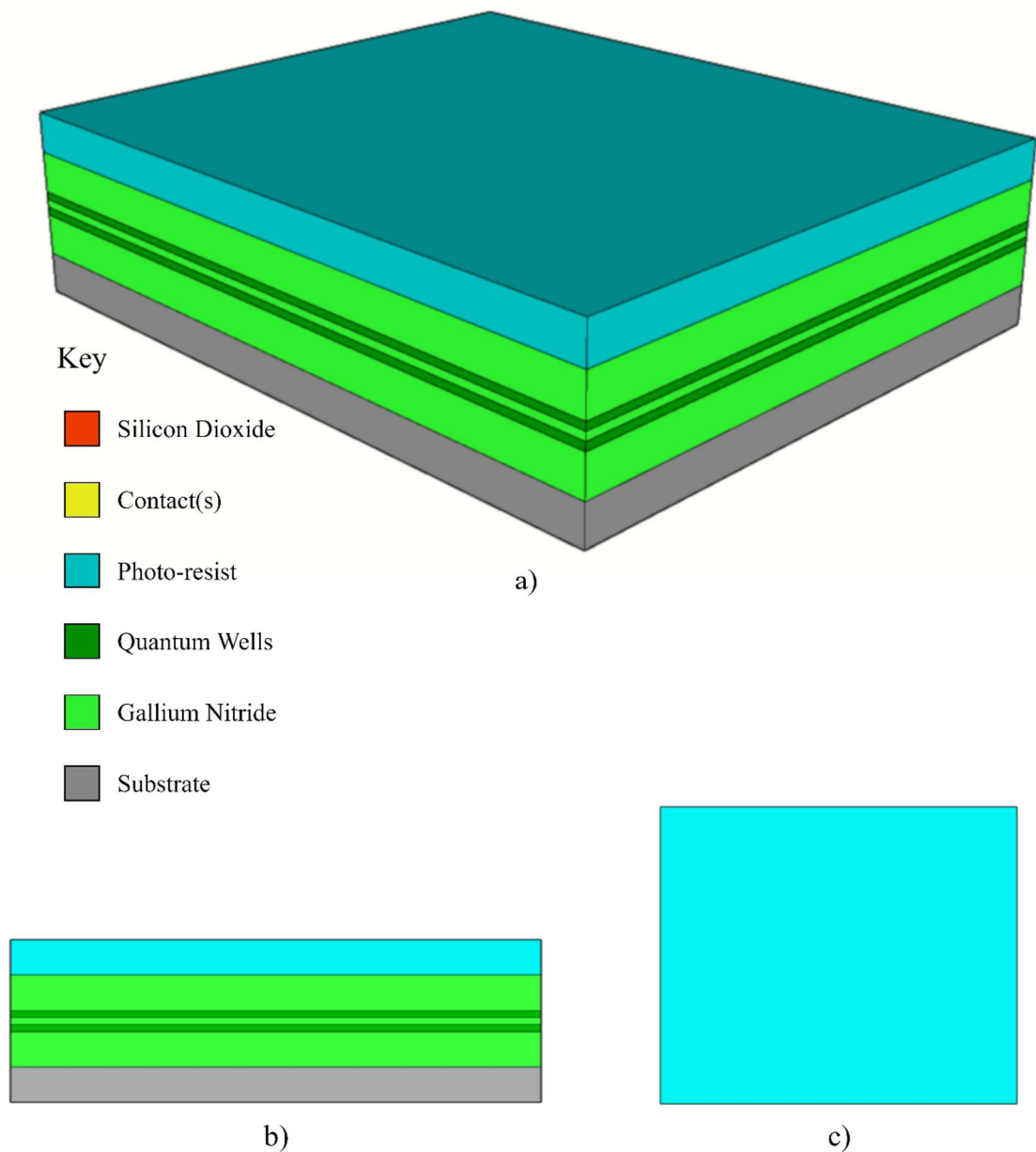


Figure 3-1 Schematic of gallium nitride wafer following cleave and clean a) 3D view, b) side view and c) birds-eye view

The second step of the fabrication process is to perform the p-contact photolithography. BPRS 200, a positive photoresist, is applied to the wafer using a dropper, before the wafer

is placed onto a spinner for 30 seconds to obtain a smooth, uniform coating as shown in Figures 3-2a), b), and c).



*Figure 3-2 Schematic of gallium nitride wafer following deposition and spin of BPRS 200
a) 3D view, b) side view and c) birds-eye view*

To create a section for the p-contact deposition, an opaque mask with a narrow, transparent, central strip is aligned above the wafer before the ultraviolet light source within the mask aligner is illuminated. The wafer is then immersed in photoresist developer, causing the now

soluble central strip of photoresist to dissolve, exposing a narrow section of the wafer on to which the p-contact can be deposited, as shown in Figures 3-3a), b), and c). This is followed by another 30 second O₂ plasma ash to remove any residual photoresist or developer from the wafer.

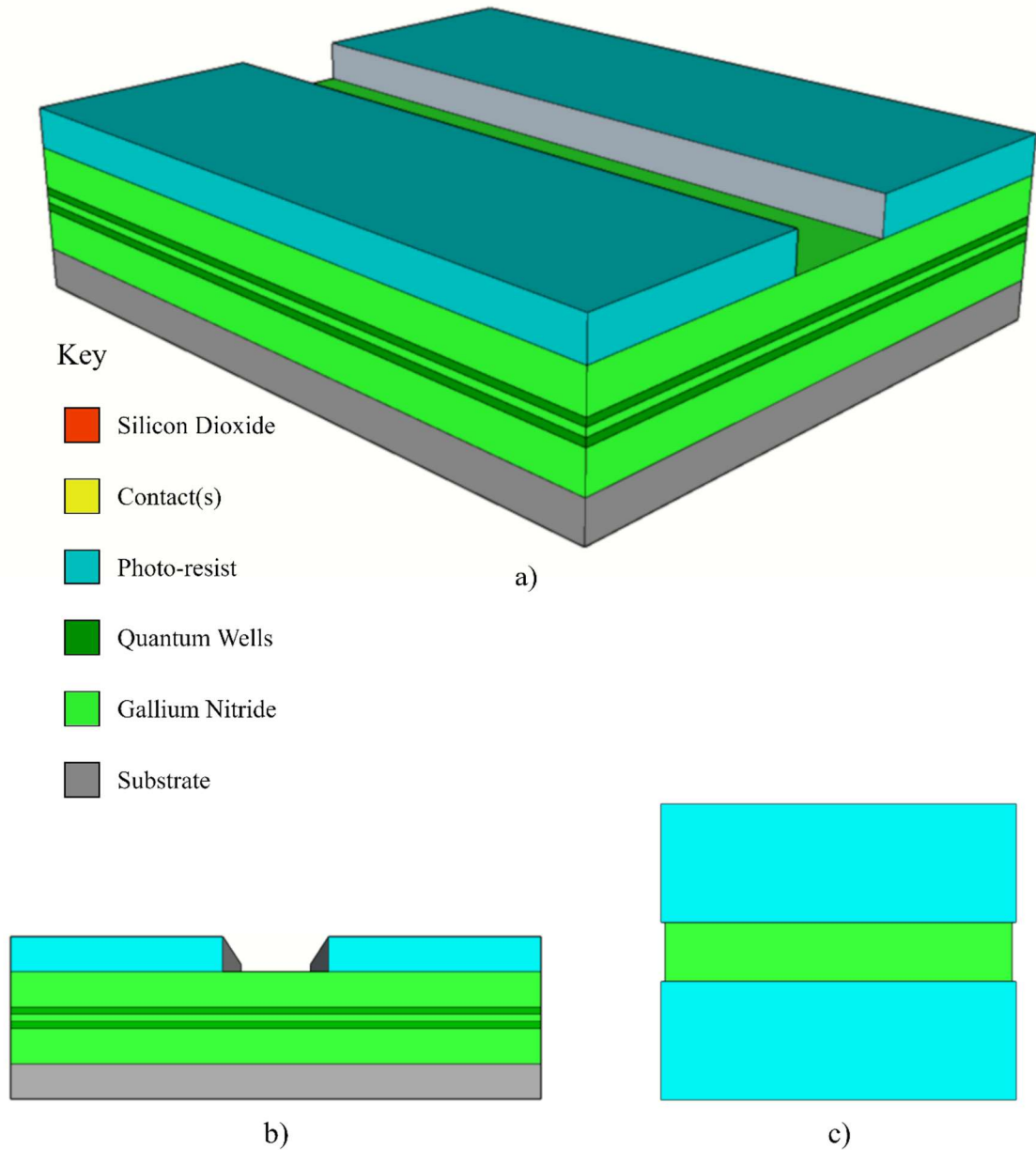


Figure 3-3 Schematic of gallium nitride wafer following exposure and development of BPRS 200 a) 3D view, b) side view and c) birds-eye view

Before the p-contact deposition, the wafer is again soaked in a 1:1 ratio of hydrochloric acid and water for 1 minute; before being rinsed thoroughly with deionised water and dried with a nitrogen gun. 5nm of nickel and 10nm of gold are then deposited onto the wafer, as shown in Figures 3-4a), b), and c), using either a sputterer or a thermal evaporator. The Ni is deposited to help act as an adhesive between the GaN wafer and the Au.

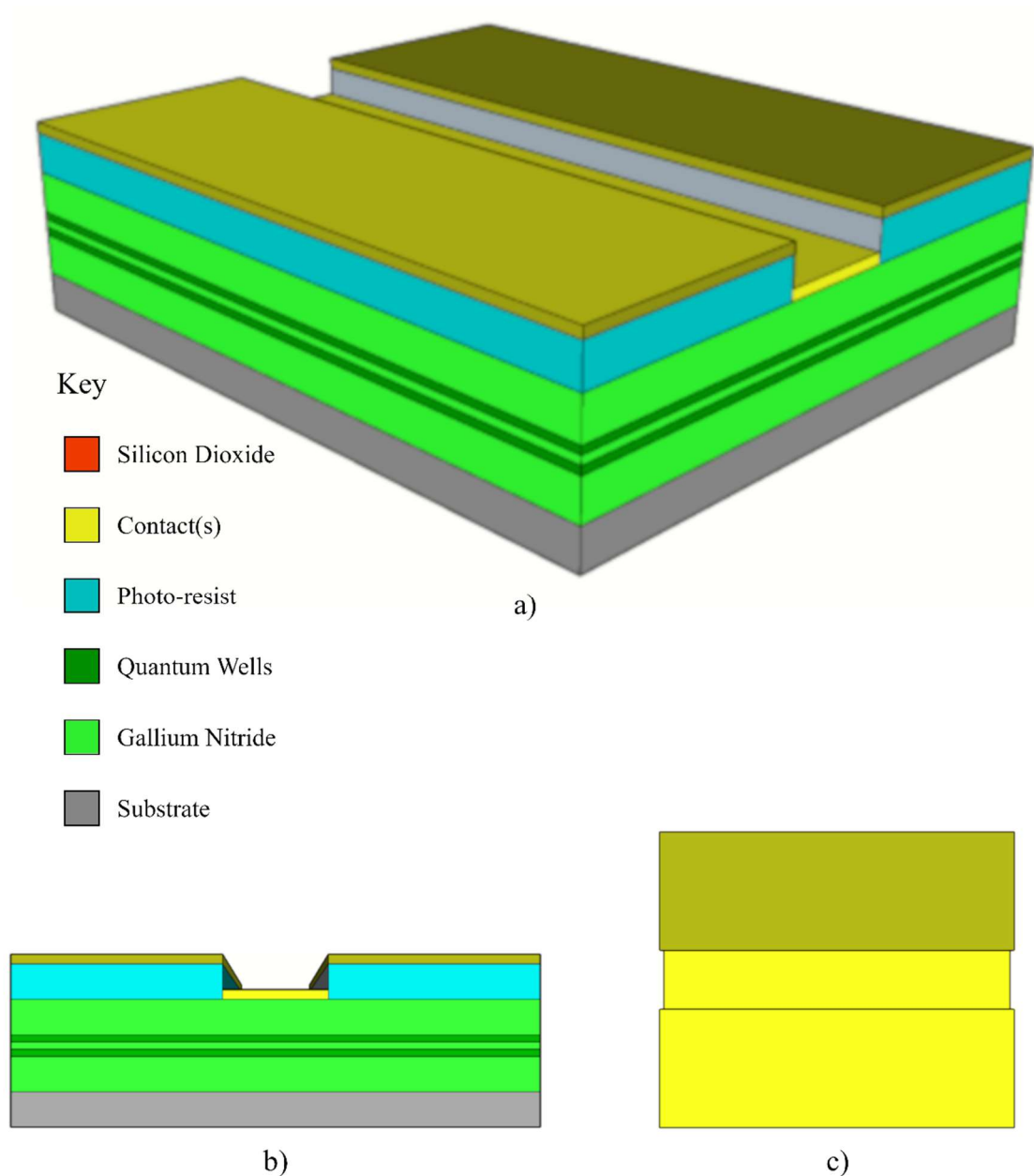


Figure 3-4 Schematic of gallium nitride wafer following deposition of nickel and gold a) 3D view, b) side view and c) birds-eye view

Following metallisation, the remaining photoresist, and Ni and Au not forming part of the p-contact, are removed using acetone before the wafer is given another three-stage clean as described earlier. The p-contact is then annealed for 5 minutes at 500°C in a rapid thermal annealer (RTA) with an oxygen nitrogen gas mix to ensure good adhesion to the wafer. Figures 3-5a), b), and c) show the wafer once the p-contact has been deposited and the photoresist removed.

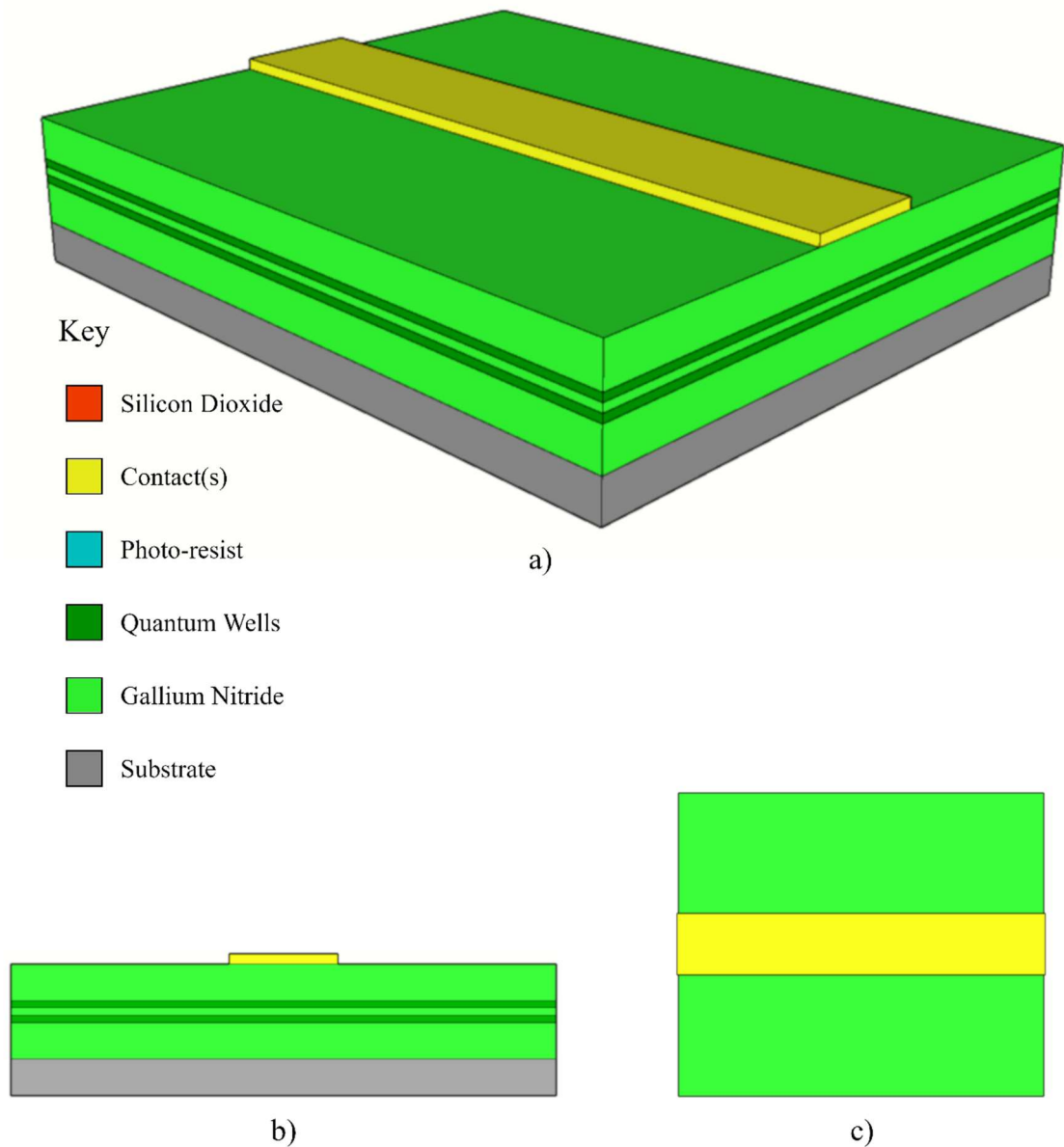


Figure 3-5 Schematic of gallium nitride wafer following deposition of nickel, gold, and removal of photoresist a) 3D view, b) side view and c) birds-eye view

The next step in the fabrication process is to prepare the wafer for etching the ridge and other features. This is performed by using PECVD to deposit 300nm of SiO₂ onto the wafer, as shown in Figures 3-6a), b), and c). This dielectric effectively acts as a hard ‘mask’, protecting the semiconductor from the etching tools that will be used to define the ridge.

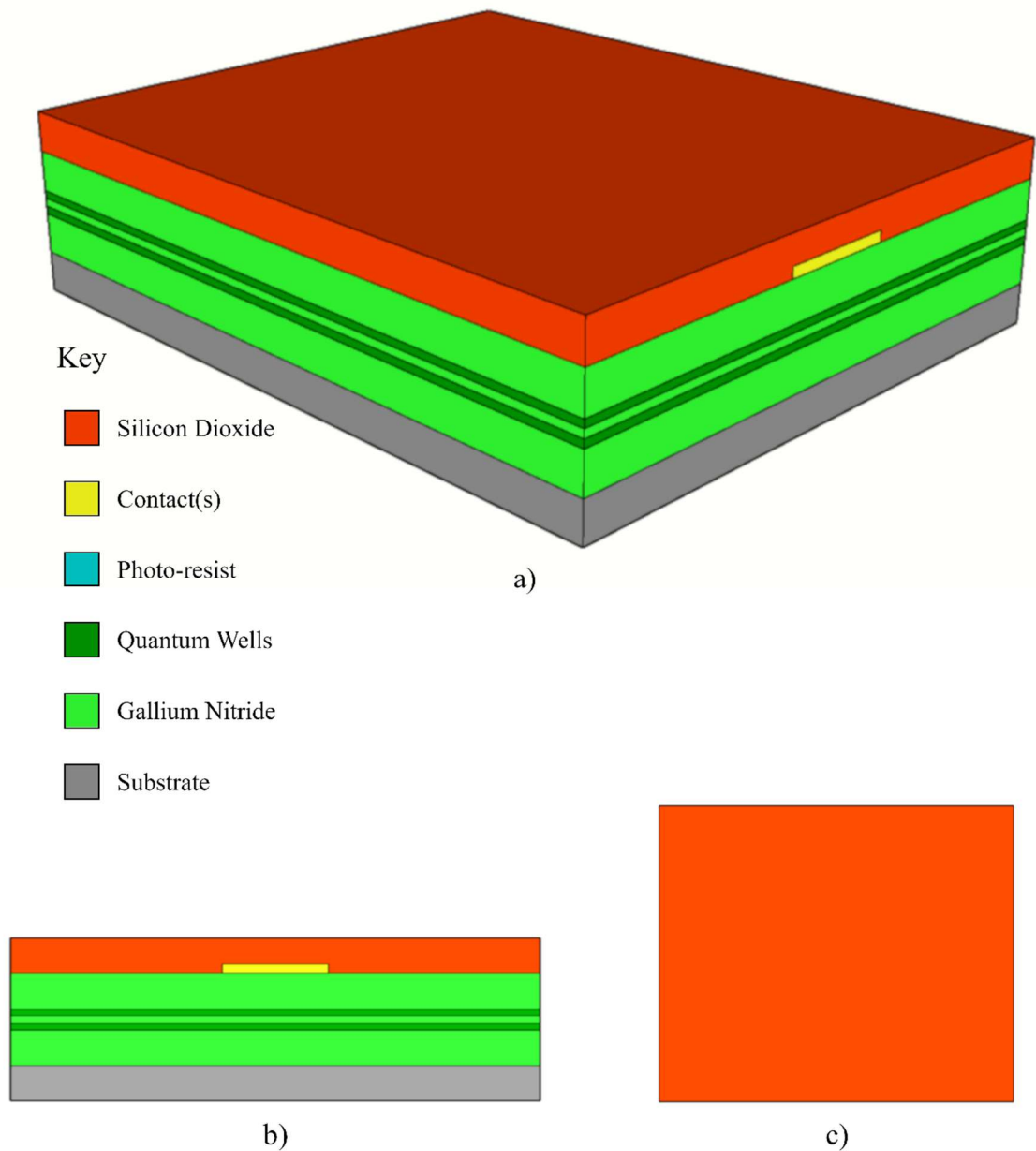


Figure 3-6 Schematic of gallium nitride wafer following deposition of silicon dioxide a) 3D view, b) side view and c) birds-eye view

SPR 350, a photoresist designed for use on dielectrics such as SiO₂ and for etching applications, is applied to the wafer using a dropper, before the wafer is placed onto a spinner for 30 seconds to obtain a smooth, uniform coating as shown in Figures 3-7a), b), and c).

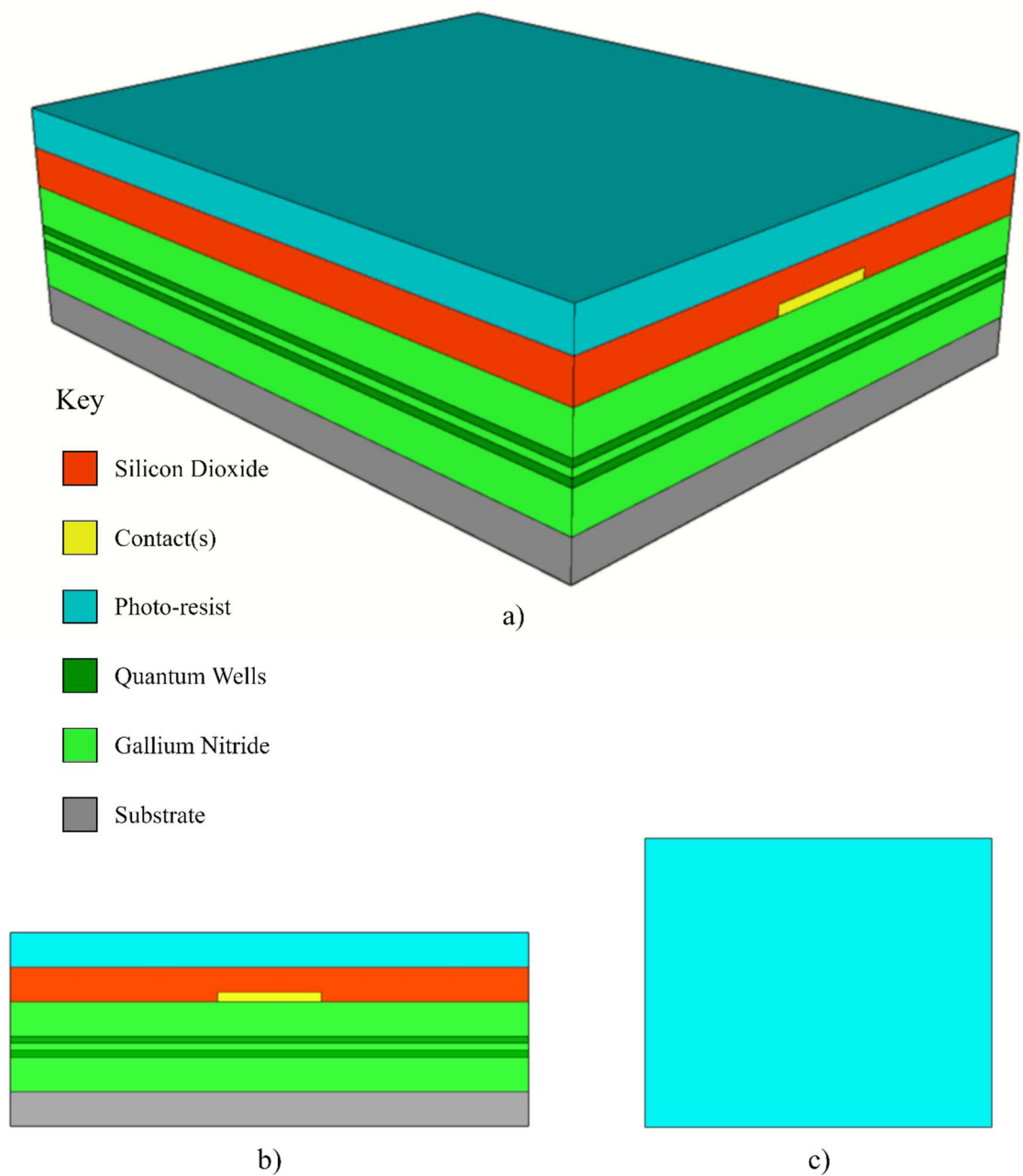


Figure 3-7 Schematic of gallium nitride wafer following deposition and spin of SPR 350 a) 3D view, b) side view and c) birds-eye view

As with the section for the p-contact definition, an opaque mask with narrow, transparent strips is aligned above the wafer, this time creating parallel lines either side of the p-contact and another narrow strip for the n-contact; as illustrated in Figures 3-8a), b), and c). The SPR 350 is exposed and developed in the same manner as the BPRS 200, followed by a 1-minute O₂ plasma ash. To set the photoresist, it is hard baked for 1 minute at 100°C.

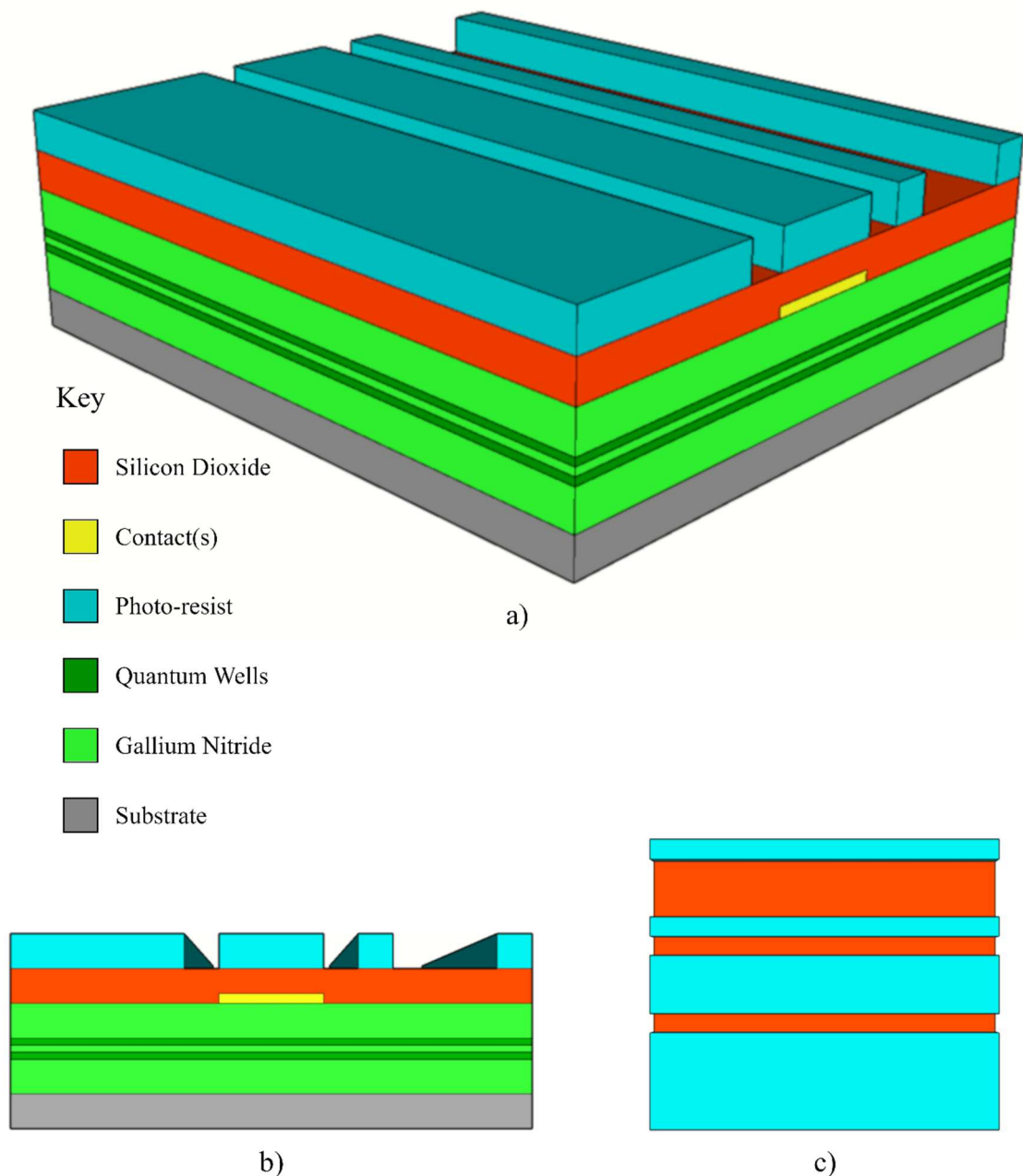


Figure 3-8 Schematic of gallium nitride wafer following exposure and development of SPR 350 a) 3D view, b) side view and c) birds-eye view

To define the ridge and expose the n-type material to the n-contact deposition, an ICP etching system is used to dry etch through the active layer at a rate of $\sim 180\text{nm}$ per minute, as shown in Figures 3-9a), b), and c). The SiO_2 layer erodes at a slower rate than the photoresist resulting in the definition of the ridge and n-contact regions. This is followed by a 1-minute oxygen O_2 plasma ash.

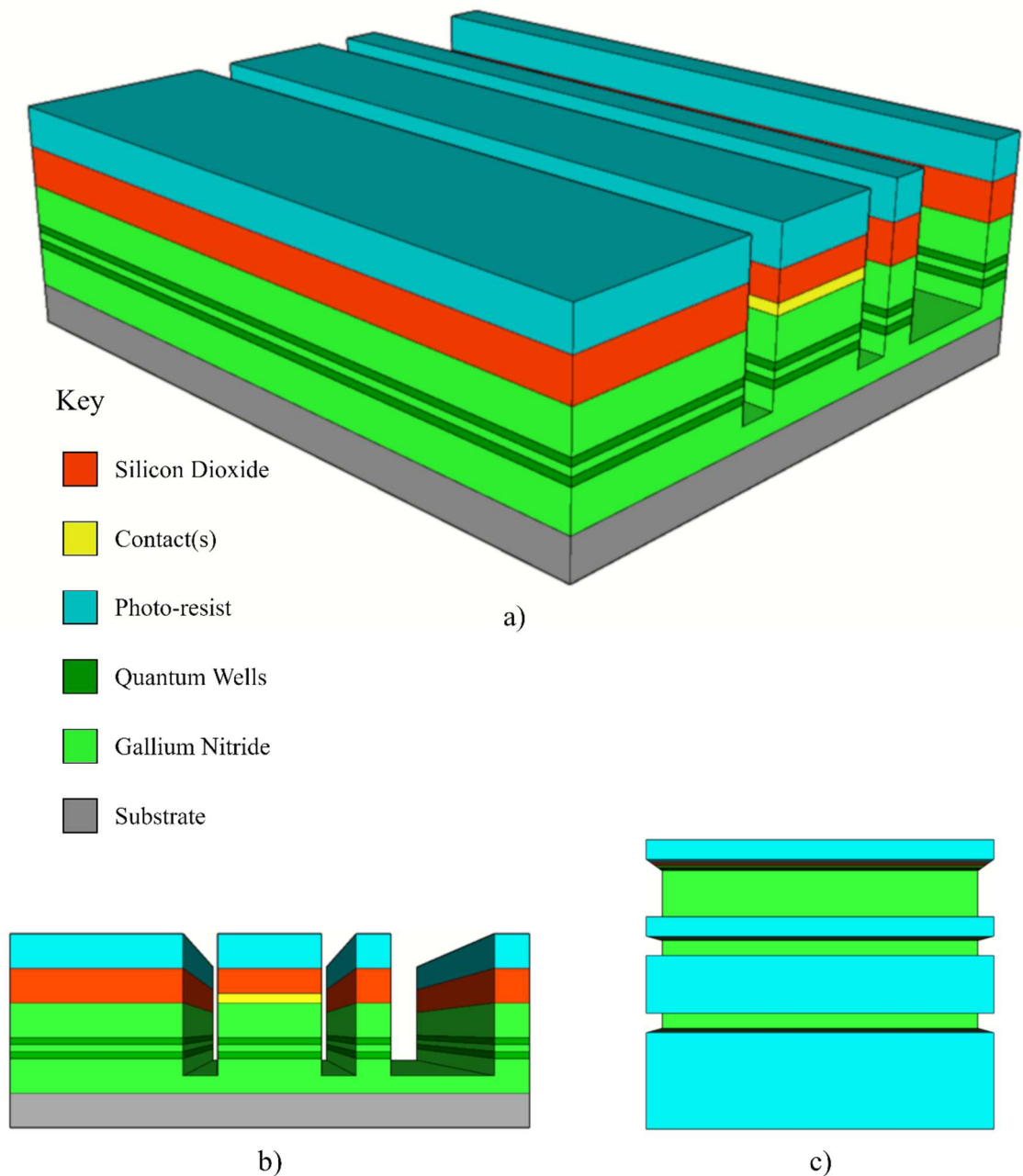


Figure 3-9 Schematic of gallium nitride wafer following dry etch a) 3D view, b) side view and c) birds-eye view

Any remaining photoresist is removed using acetone before the hard mask is removed using hydrofluoric (HF) acid and the wafer is given another three-stage clean as described earlier. The result is depicted in Figures 3-10a), b), and c).

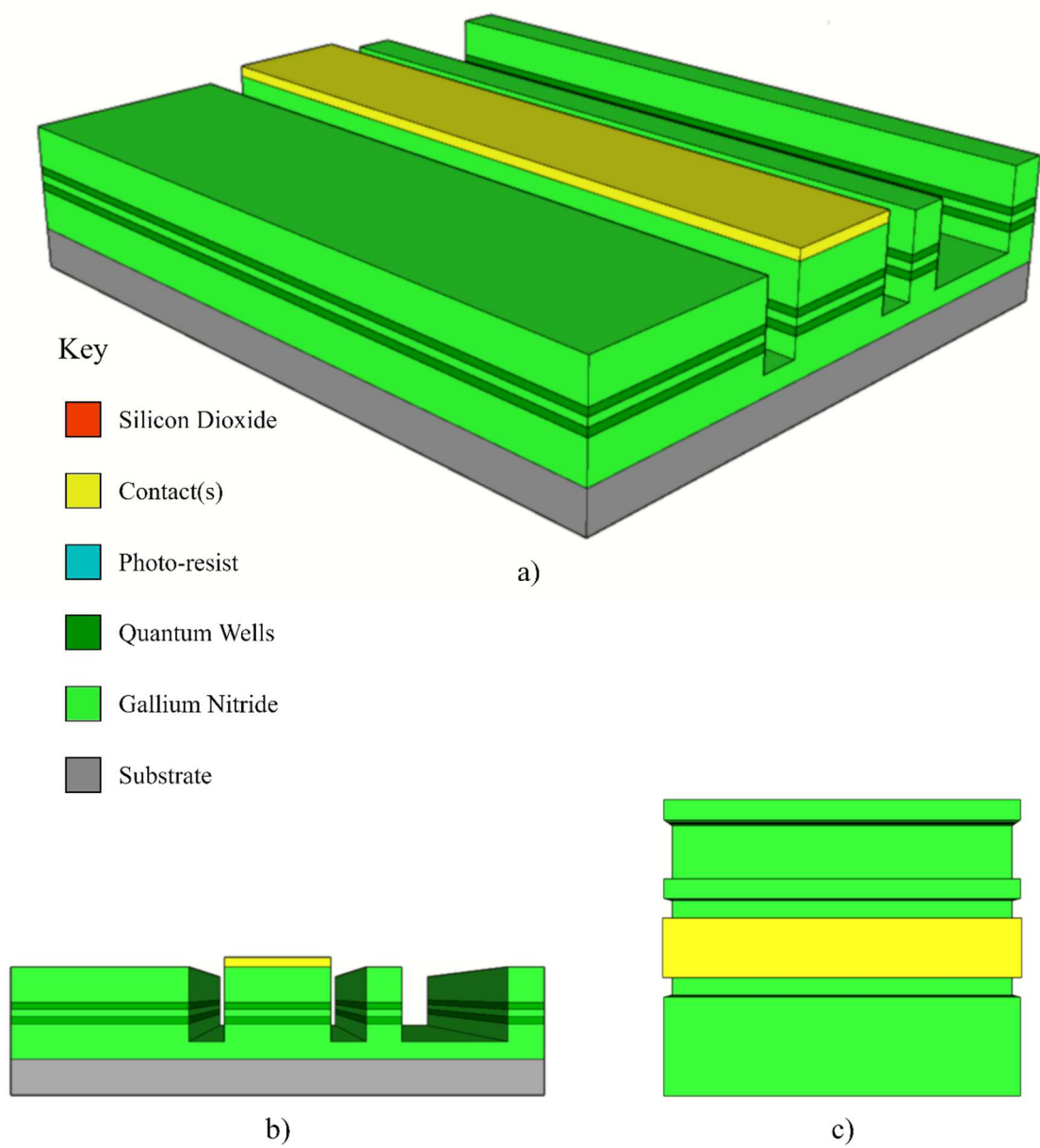


Figure 3-10 Schematic of gallium nitride wafer following removal of SPR 350 and silicon dioxide a) 3D view, b) side view and c) birds-eye view

With the ridge defined, the next step is to create insulated p and n-contact windows. The PECVD is again used to deposit 300nm of SiO₂, as shown in Figures 3-11a), b), and c).

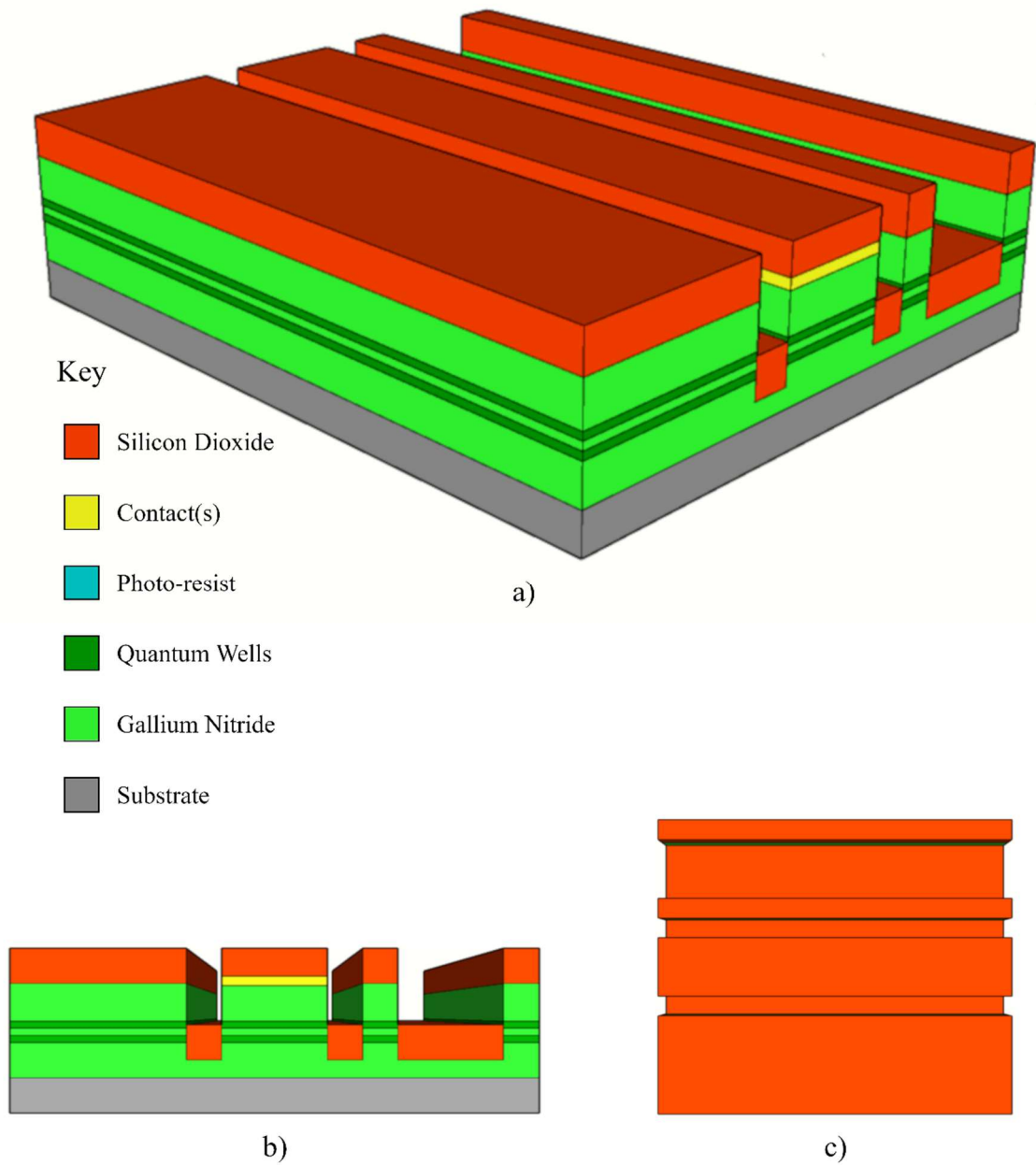


Figure 3-11 Schematic of gallium nitride wafer following deposition of silicon dioxide a) 3D view, b) side view and c) birds-eye view

BPRS 200 is applied to the wafer using a dropper, before the wafer is placed onto a spinner for 30 seconds to obtain a smooth, uniform coating as shown in Figures 3-12a), b), and c). As this etch will be shallower than before, BPRS 200 is used instead of SPR 350.

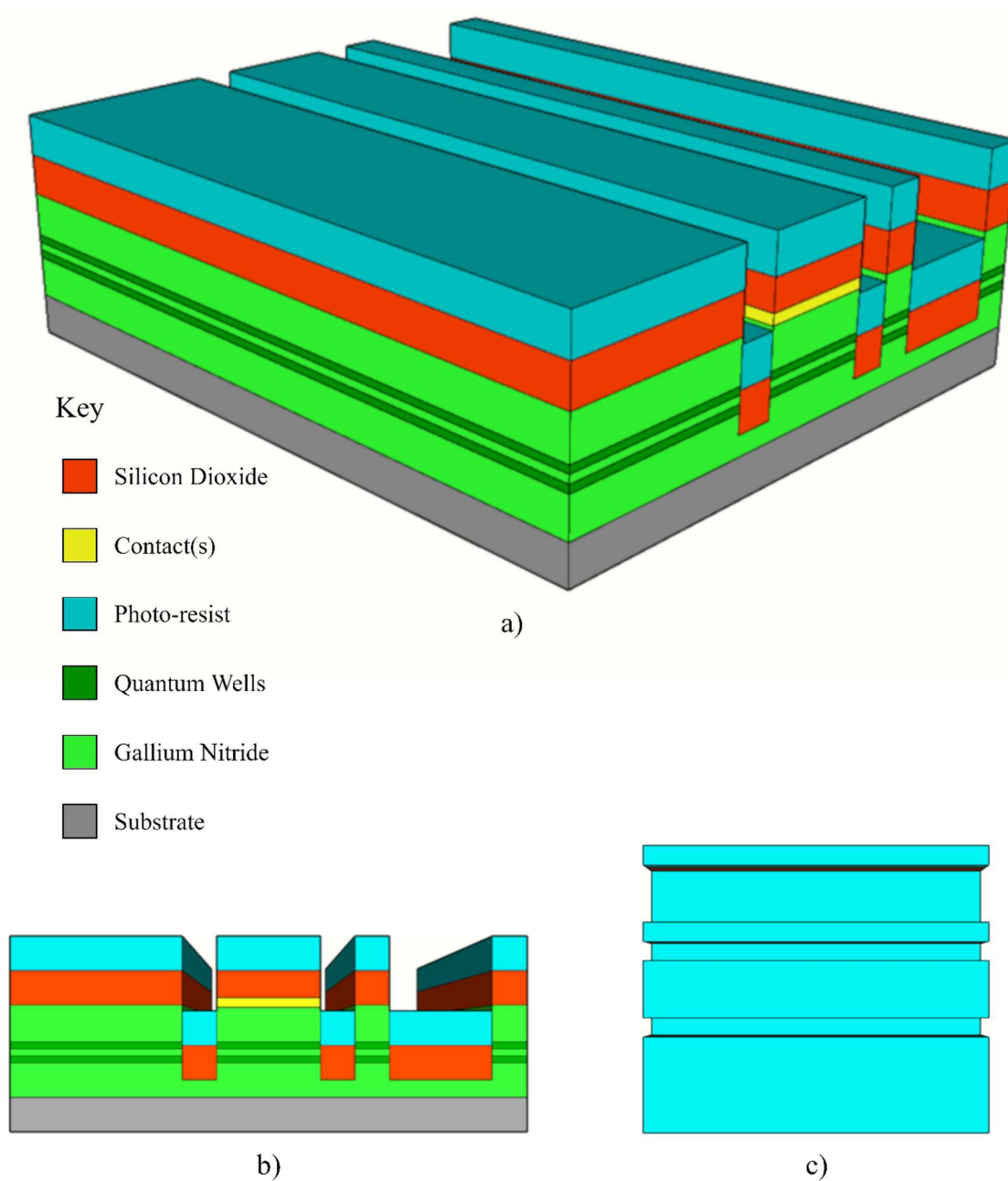


Figure 3-12 Schematic of gallium nitride wafer following deposition and spin of BPRS 200
a) 3D view, b) side view and c) birds-eye view

As with the sections for the p-contact definition and the ridge definition, an opaque mask with narrow, transparent strips is aligned above the wafer, this time creating rectangles above the p-contact and where the n-contact will be to the side of the p-contact; as illustrated in Figures 3-13a), b), and c). The BPRS 200 is exposed and developed in the same manner before, followed by a 1-minute O₂ plasma ash. Again, the photoresist is hard baked for 1 minute at 100°C so it sets prior to the dry etch.

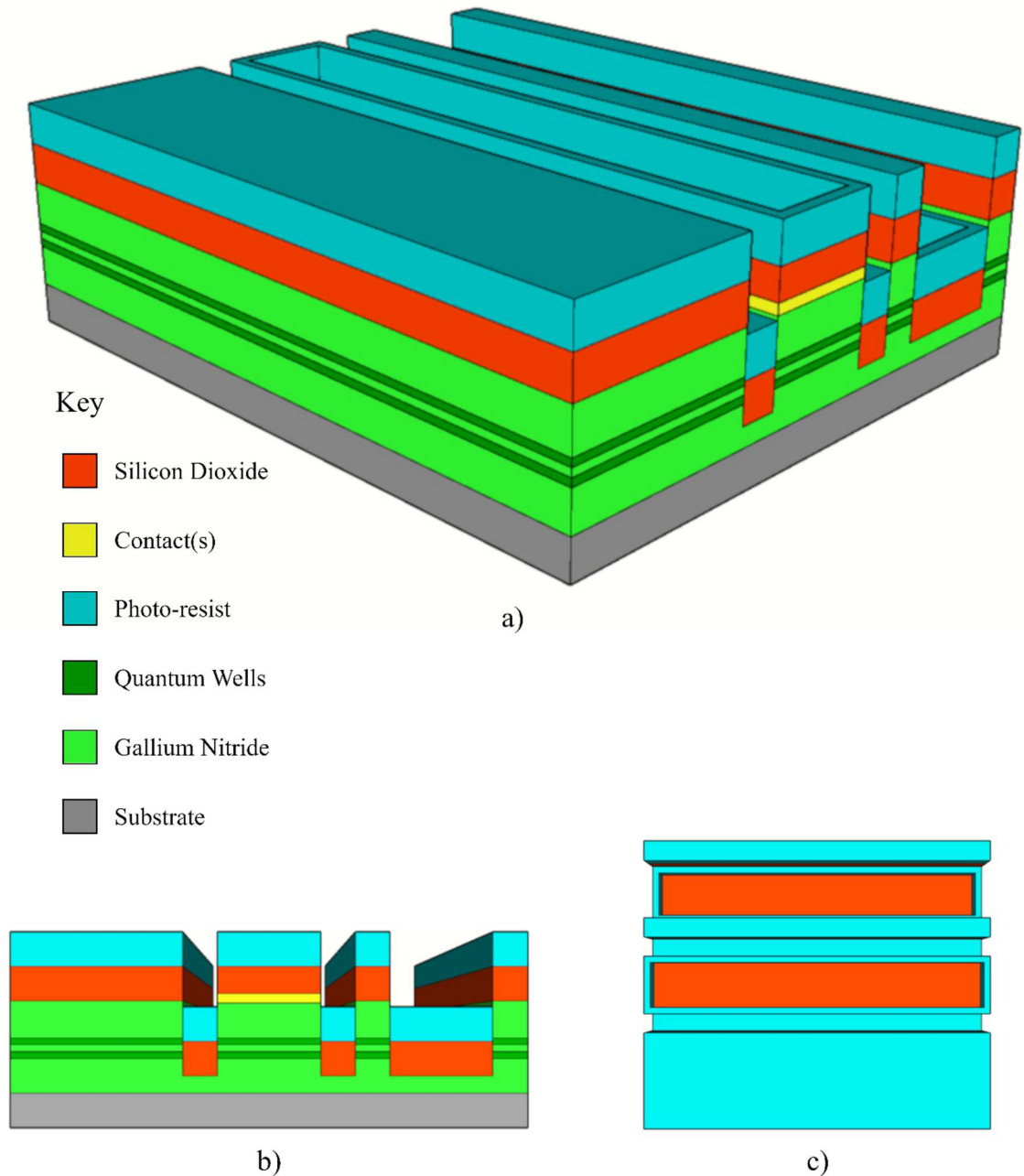


Figure 3-13 Schematic of gallium nitride wafer following exposure and development of BPRS 200 a) 3D view, b) side view and c) birds-eye view

ICP is used again to dry etch through the SiO₂ layer at a rate of ~180nm per minute, as shown in Figures 3-14a), b), and c). This is followed by a 1-minute O₂ plasma ash. As with p-contact deposition, the wafer is soaked in a 1:1 ratio of hydrochloric acid and water, but this time for 30 seconds; before being rinsed thoroughly with deionised water and dried with a nitrogen gun.

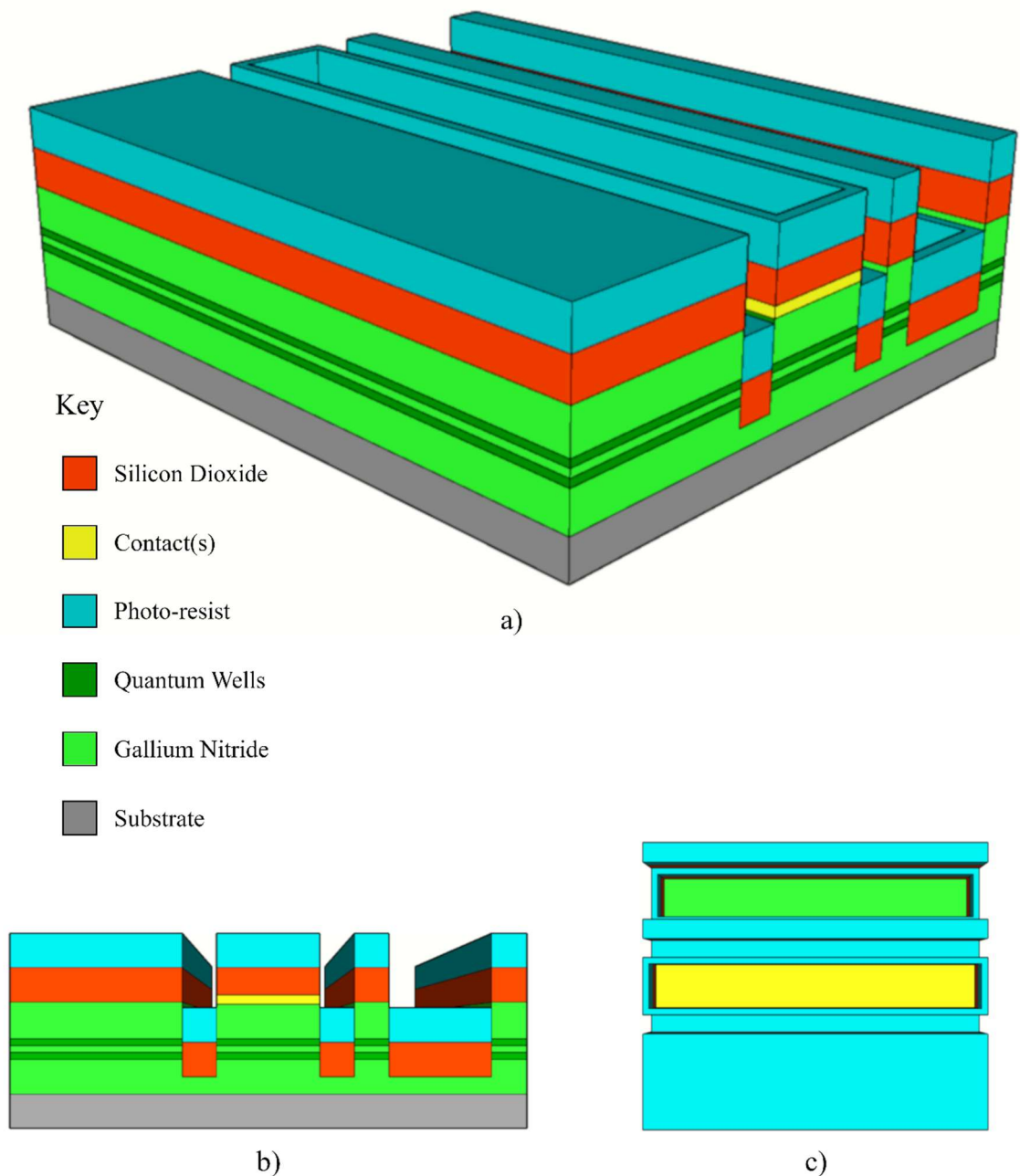


Figure 3-14 Schematic of gallium nitride wafer following dry etch a) 3D view, b) side view and c) birds-eye view

20nm of Ti and 200nm of Au are then deposited onto the wafer using either a sputterer or a thermal evaporator to form the n-contact and bond pads. The Ti is deposited to help act as an adhesive between the GaN wafer and the Au. The remaining photoresist, and Ti and Au not forming part of the n-contacts and bond pads, are removed using acetone before the wafer is given another three-stage clean as described earlier. The result is depicted in Figures 3-15a), b), and c).

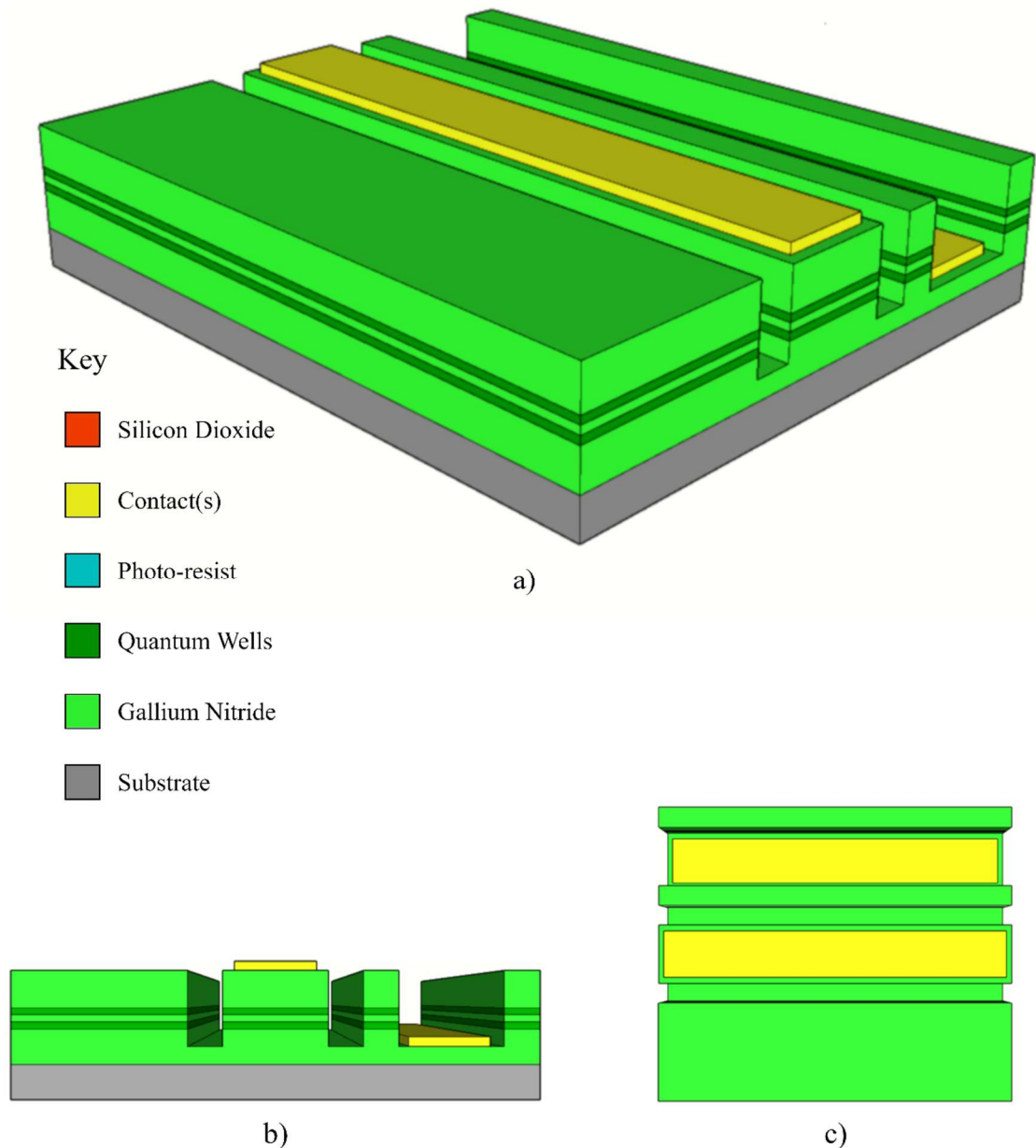


Figure 3-15 Schematic of gallium nitride wafer following deposition of titanium, gold, and removal of BPRS 200 a) 3D view, b) side view and c) birds-eye view

Finally, the substrate is thinned, followed by a 1-minute O₂ plasma ash and a three-stage clean. The wafer is then soaked again in a 1:1 ratio of hydrochloric acid and water for 30 seconds; before being rinsed thoroughly with deionised water and dried with a nitrogen gun. 20nm of Ti and 200nm of Au are then deposited onto the backside of the wafer using either a sputterer or a thermal evaporator to form a rear n-contact. As before, the Ti is deposited to help act as an adhesive between the GaN wafer and the Au. The final device schematics are illustrated in Figures 3-16a), b), and c).

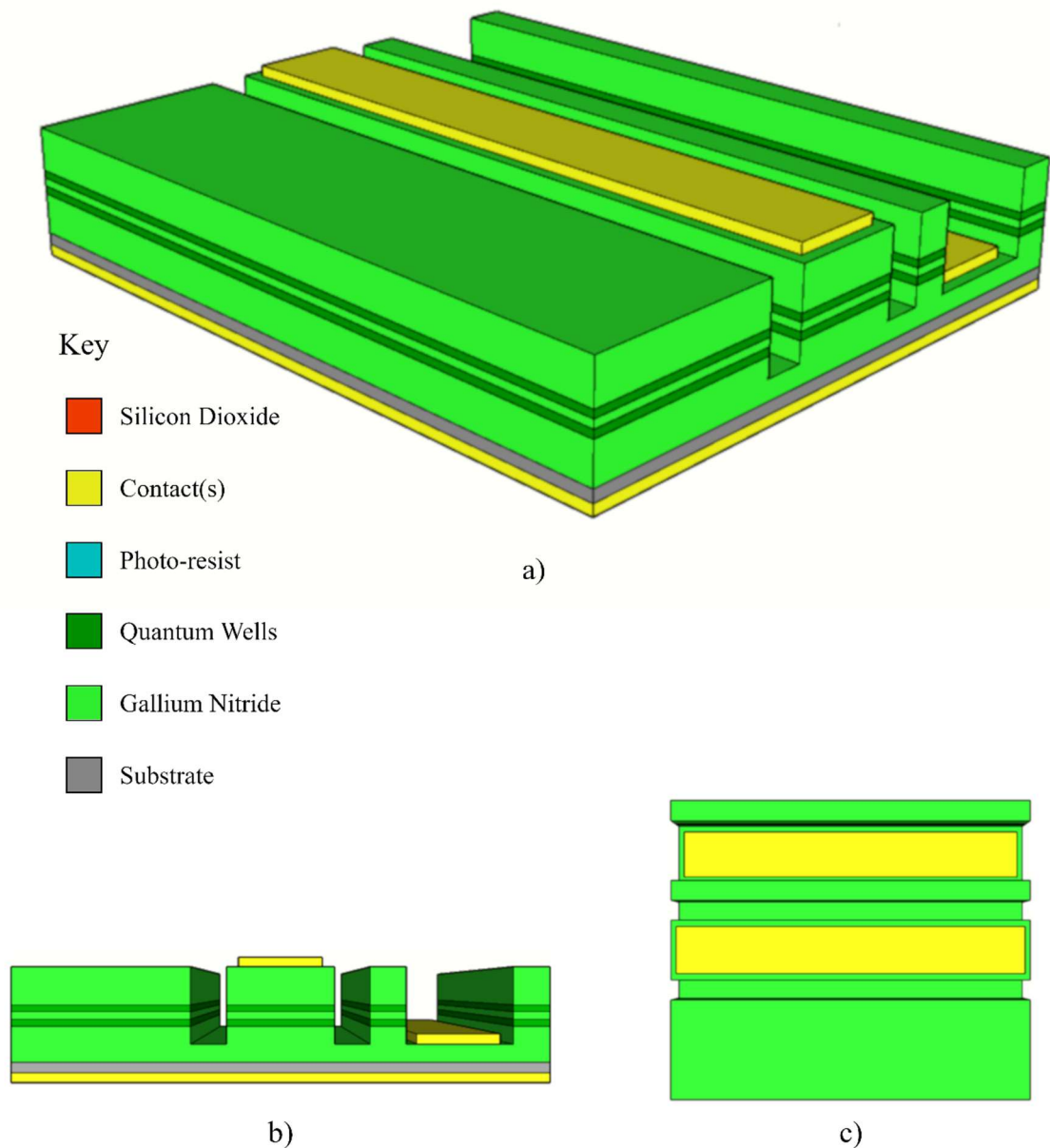


Figure 3-16 Schematic of gallium nitride wafer following thinning of substrate and deposition of titanium and gold a) 3D view, b) side view and c) birds-eye view

3.4 Characterisation of Fabricated GaN Laser Diodes

Figure 3-17a) shows a scanning electron microscope (SEM) image of a number of GaN laser diodes fabricated as part of this research. Their lengths range from $\sim 2400\text{-}3000\mu\text{m}$, with widths of 5, 10, 15, and $50\mu\text{m}$. Three devices are labelled in terms of their ridge width, as they will be the main devices characterised and discussed in this chapter. Figure 3-17b) shows a magnified SEM image of one of the GaN lasers shown in Figure 3-17a) zoomed in on the front facet, ridge, and top contact.

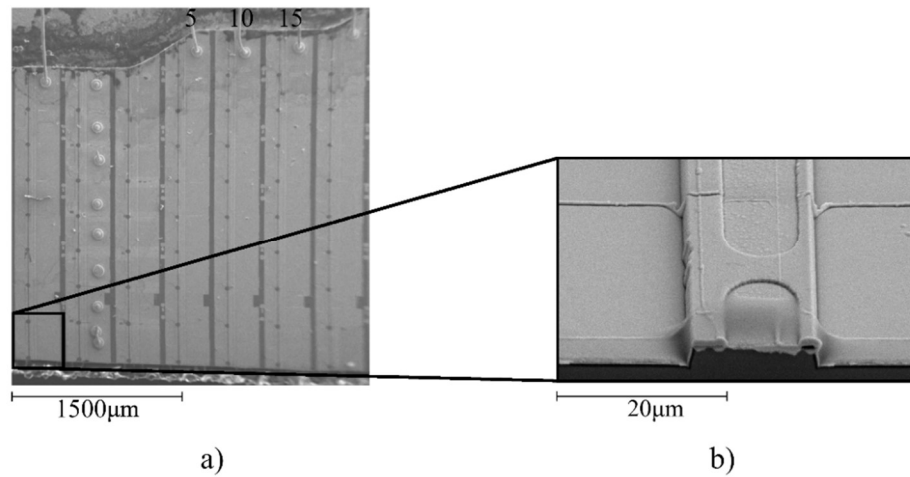


Figure 3-17 Scanning electron microscope images of a) a number of GaN laser diodes and b) the front facet, ridge and top contact

As introduced in Chapter One section 1.3, gain is related to the length of the laser waveguide by Equation 1-1, which can be rearranged to form Equation 3-1 assuming the absorption coefficient, α , is approximately constant:

$$R_1 R_2 e^{2g_{th}L} e^{-2\alpha L} = 1 \quad \text{Equation 3-1}$$

where R_1 and R_2 are the mirror reflectivities, L is the length of the gain medium, and g_{th} is the threshold gain [24]. Also described in Chapter One section 1.3 is the necessity that a

resonant cavity is formed within the waveguide of a laser diode in order for lasing to occur. SLED design reduces the feedback required to form the resonant cavity such that the only gain, and by extension output power, produced is from a single pass along the waveguide. This is expressed in Equation 3-2:

$$G_S = e^{\left[\Gamma\left(g_0\eta_i\frac{J}{d}-\alpha\right)L\right]} = e^{\left[\frac{\Gamma\kappa I}{d}-\Gamma\alpha L\right]} \quad \text{Equation 3-2}$$

where G_S is the single pass gain, Γ is the confinement factor, g_0 is the gain coefficient, $\sim 7680\text{cm}^{-1}$ for GaN [25], η_i is the internal quantum efficiency, J is the injection current density, d is the active layer thickness, α remains the absorption coefficient, L is the length of the gain medium, κ is the effective stripe width, and I is the injection current. The output power is approximately equal to the spontaneous emission power, P_S , multiplied by G_S [09]. It is therefore expected that by fabricating around three times longer devices in comparison to the commercially available laser diodes from Chapter One, it is expected gain will be increased, in addition to more on-chip real estate being available for absorber sections.

Figure 3-18a) (inset) shows a schematic of the $5\mu\text{m}$ wide GaN device labelled ‘5’ in Figure 3-17a), which is $\sim 2600\mu\text{m}$ long and features a $5\mu\text{m}$ wide ridge. The front facet is perpendicular to the waveguide and no anti-reflection coatings were used. This device is a SLED rather than a laser diode due to the angled rear facet, included to suppress lasing by reducing feedback. Methods of feedback suppression are compared and discussed in Chapter One section 1.3. Figure 3-18b) plots voltage as a function of current density, giving a series resistance of $\sim 19\Omega$. Figure 3-18c) plots optical output power as a function of current density. As the injected current density increases optical output power also increases, except super-linearity is observed prior to the lasing threshold, confirming the device is indeed a SLED and neither an LED nor a laser diode. Figure 3-18d) plots emission spectra as a function of wavelength for different levels of injected current applied to the device. For low current densities, such as 1.9 , 3.8 , and 5.7kA/cm^2 , the observed emission spectra are broad, smooth, and continuous. As the current density is increased and approaches 7.6kA/cm^2 , gain within the SLED overcomes loss and lasing occurs at $\sim 425\text{nm}$.

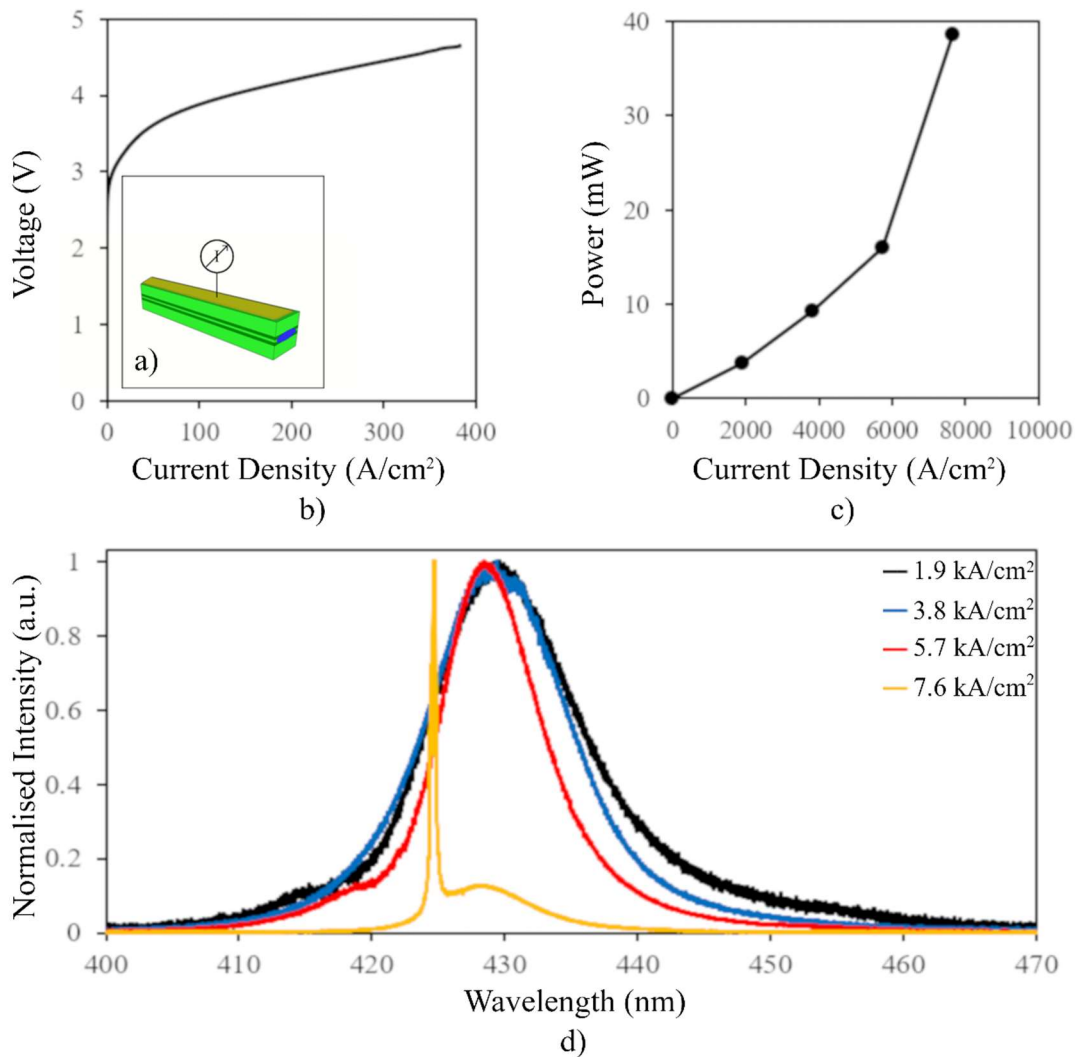


Figure 3-18 5 μm GaN SLED a) schematic b) voltage for injected current density c) optical output power for injected current density and d) emission spectra for various applied current densities

As the fabricated GaN devices were bespoke, with little known about their characteristics, performance, reliability, and reproducibility, the decision was made to operate the devices pulsed rather than continuous wave (CW) as in Chapter Two. When determining the width of the pulse and its duty cycle or period, a compromise must be made between very short pulses and low duty cycle to minimise self-heating effects, and the overshoot and ringing becoming a significant proportion of the pulse width. The current source [26] was connected to an oscilloscope and the output observed over a range of pulse widths, duty cycles, and currents. The optimum drive settings were found to be 10 μs pulse widths with a 2.5% duty cycle, and were used for all measurements in this chapter and in Chapter Four, except for voltage as a function of current density, which were obtained CW.

Figure 3-19a) (inset) shows a schematic of the 10 μm wide GaN laser diode labelled ‘10’ in Figure 3-17a), which is $\sim 2700\mu\text{m}$ long and features a 10 μm wide ridge. The front and rear facets are perpendicular to the waveguide and no anti-reflection coatings were used. Figure 3-19b) plots voltage as a function of current density, giving a series resistance of $\sim 12\Omega$.

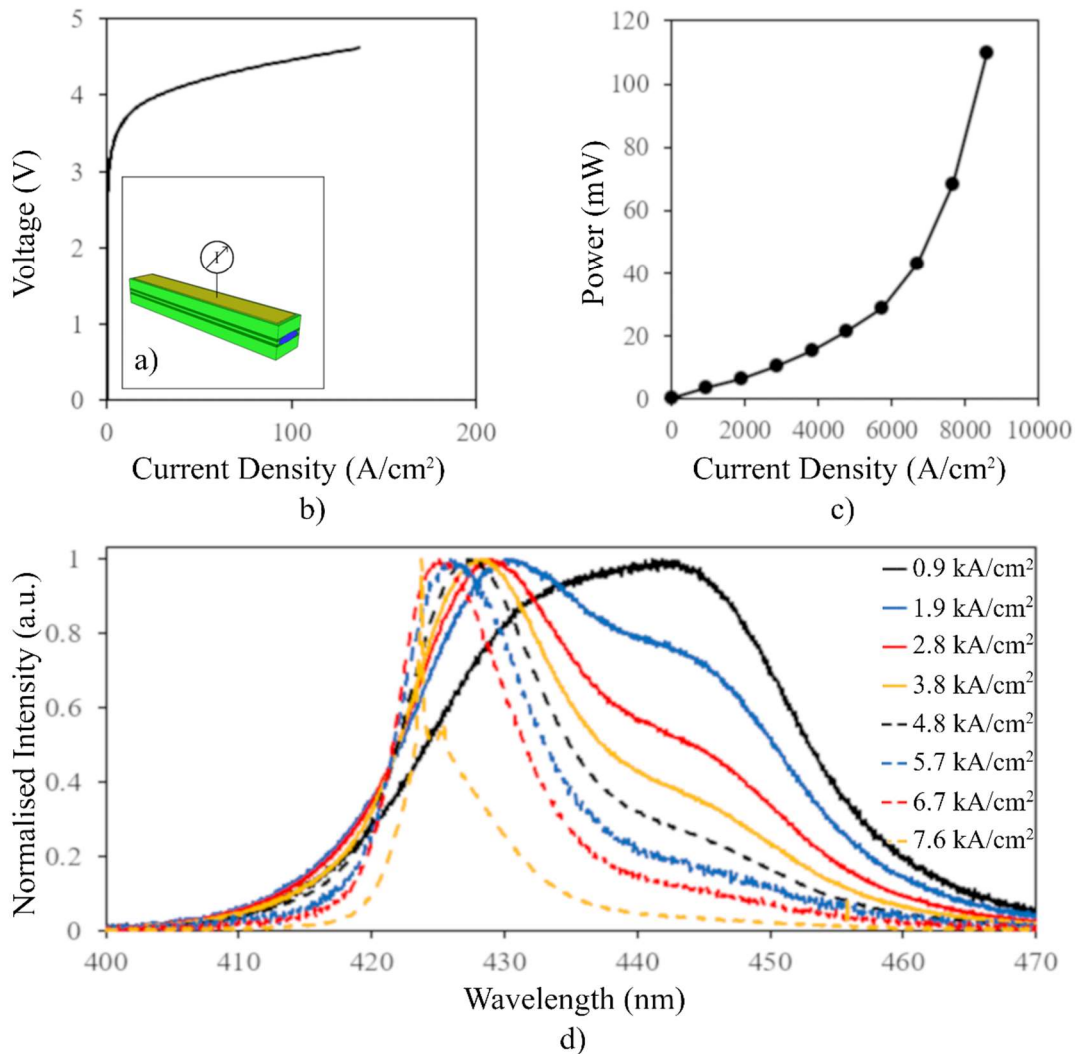


Figure 3-19 10 μm GaN laser diode a) schematic b) voltage for injected current density c) optical output power for injected current density and d) emission spectra for various applied current densities

Figure 3-19c) plots optical output power as a function of current density. As with the 5 μm SLED, as the current density increases optical output power also increases, with super-linearity observed. Figure 3-19d) plots emission spectra as a function of wavelength for different levels of injected current applied to the device. For current densities, up to

$\sim 7\text{kA/cm}^2$, the observed emission spectra are broad, smooth, and continuous. As the current density is increased above 7kA/cm^2 a lasing peak $\sim 423\text{nm}$ is visible, broader than that observed in Figure 3-18d), suggesting there could be mode hopping within this device [24].

Figure 3-20a) (inset) shows a schematic of the $15\mu\text{m}$ wide GaN laser diode labelled ‘15’ in Figure 3-17a), which is $\sim 2700\mu\text{m}$ long and features a $15\mu\text{m}$ wide ridge. The front and rear facets are perpendicular to the waveguide and no anti-reflection coatings were used. Figure 3-20b) plots voltage as a function of current density, giving a series resistance of $\sim 14\Omega$.

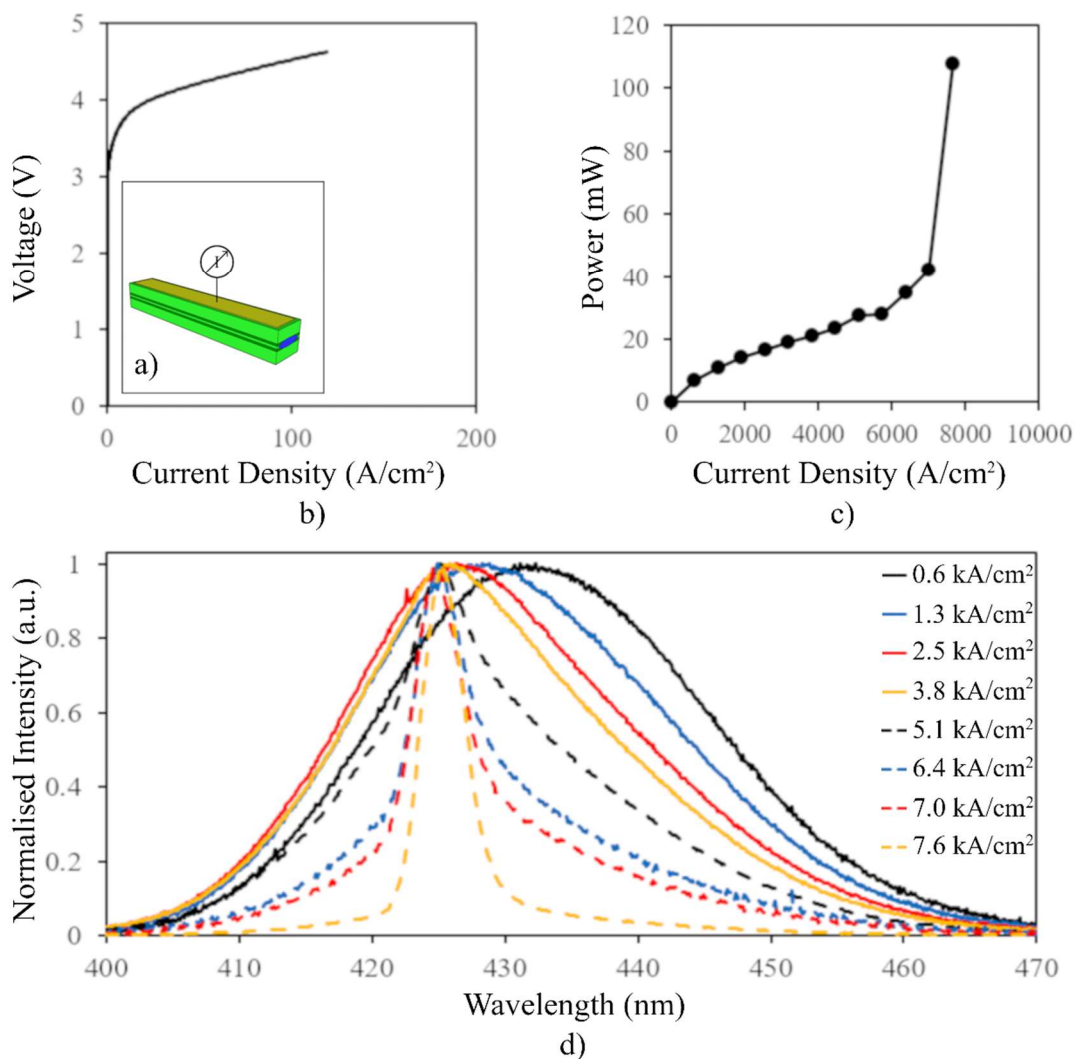


Figure 3-20 $15\mu\text{m}$ GaN laser diode a) schematic b) voltage for injected current density c) optical output power for injected current density and d) emission spectra for various applied current densities

Figure 3-20c) plots optical output power as a function of current density. As with the 5 μm and 10 μm devices discussed so far, as the current density increases optical output power also increases, with super-linearity observed, and a large increase in output power above 7kA/cm². Figure 3-20d) plots emission spectra as a function of wavelength for different levels of injected current applied to the device. Unlike the other devices discussed in this chapter, there was no lasing peak observed for any applied current density, the observed emission spectra were all broad, smooth, and continuous. This is attributed to the larger ridge width causing increased absorption and lateral modes, and had it been possible to increase the output of the current source any further, it is expected that a lasing peak would have been seen for current densities not much greater than 7.6kA/cm².

From Equation 3-2, as well as increasing the length of the waveguide, increasing its width should also give rise to SLEDs with higher powers [09]. However, limitations of the current source [26] in supplying currents greater than 3A, equivalent to current densities above 7.6kA/cm² through the 15 μm wide ridge; coupled with the significant self-heating effect when applying such high currents to a device without further thermal management considerations than those discussed in Chapter Two section 2.4 and earlier in this section, meant only the 5 μm and 10 μm ridge width devices were investigated further.

3.5 Post FIB Modification

Figure 3-21a) (inset) shows a schematic of the 5 μm wide SLED following segmentation of the top contact using a FIB system. The operation of a FIB system and contact segmentation details are described and discussed in Chapter Two section 2.5. Separated into two sections, optically connected but electrically isolated, of $\sim 2/3$ and $\sim 1/3$ of the device length respectively, the forwardmost section is $\sim 1750\mu\text{m}$ long and the rear section is $\sim 850\mu\text{m}$, with an isolation of 5M Ω achieved between them. To discern whether the device performance had been adversely affected by the FIB process, both sections were connected to the same current source and driven as one. Figure 3-21b) plots voltage as a function of current density for the front 2/3 only, the rear 1/3 only, and both sections together.

As discussed in section 3.4, concerns regarding whether the device would undergo too much self-heating following the FIB process meant these measurements were conducted to $\sim 1/3$ of the level in Figure 3-18b), as the device was operated CW. However, for the range in which the measurements overlap with those obtained before segmentation, the resistances when current is injected into either only the rear 1/3, or both sections at once, are higher; while the resistance when current is injected into only the front 2/3 is lower.

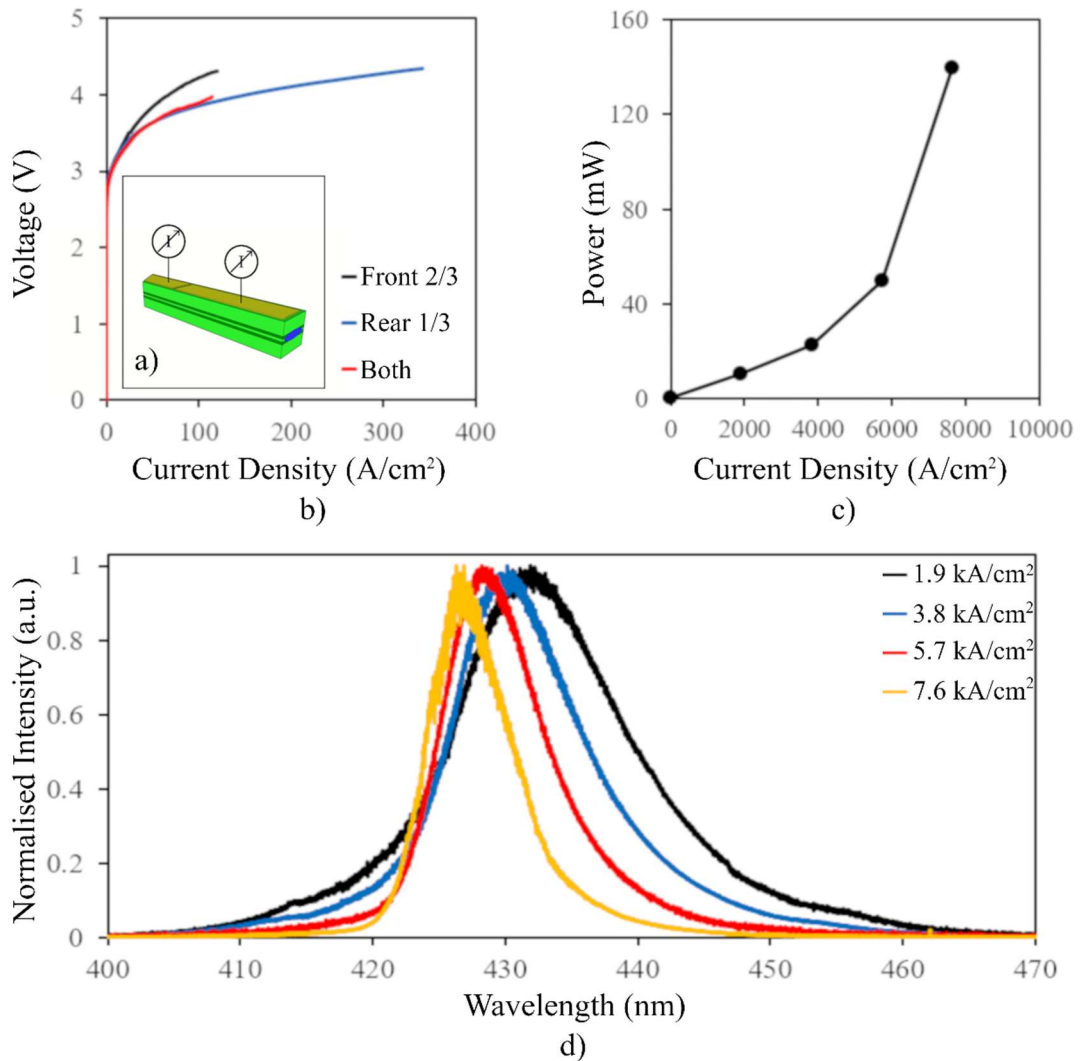


Figure 3-21 5 μm GaN SLED following the first segmentation of the top contact with both sections driven together as one a) schematic b) voltage for injected current density c) optical output power for injected current density and d) emission spectra for various applied current densities

The reduction in resistance in the front 2/3 could be due to gallium ion implantation during the FIB process, self-annealing while obtaining measurements of the spectra at high current densities, or a combination of both. The higher resistance is attributed to the reduced area for the current to flow through as the top contact is smaller.

Figure 3-21c) plots optical output power as a function of current density, with the curve shape in good agreement with the one displayed in Figure 3-18c). However, the output power for the same current density is ~100mW higher. There are a couple of potential reasons for the increase in output power; the first being improved alignment with the power meter, but this seems very unlikely to account for such an increase. The second potential reason is the difference in resistances for each section as described above, meaning more current could be injected into the rear of the device than the front 2/3. Increased current density in the rear 1/3 could result in this section optically pumping the front 2/3, which, if the front 2/3 becomes transparent, could operate as a ~1750 μ m long semiconductor optical amplifier [27]. This is considered more likely to produce the observed increase in power after segmentation. Figure 3-21d) plots emission spectra as a function of wavelength for different levels of injected current applied to the device. As with Figure 3-18d), for low current densities such as 1.9, 3.8, and 5.7kA/cm², the observed emission spectra are broad, smooth, and continuous. The notable difference is for 7.6kA/cm², where although spectral ripple can be seen in Figure 3-5d), implying that the threshold is being approached, there is a distinct lack of the lasing peak seen in Figure 3-18d). This suggests that in the process of segmenting the top contact, the FIB milling process has slightly increased the lasing threshold, offering a greater range of SLED operation.

Figure 3-22a) shows a schematic of the 10 μ m wide GaN laser diode following the first segmentation of the top contact using the FIB system. Also separated into 2 sections ~2/3 and ~1/3 respectively, the forwardmost section is ~1800 μ m and the rear section is ~900 μ m, with an isolation of >1k Ω achieved between them. As above, both sections were connected to the same current source and driven as though they were one device. Figure 3-22b) plots optical output power as a function of current density, and the curve is in good agreement with that plotted in Figure 3-19c).

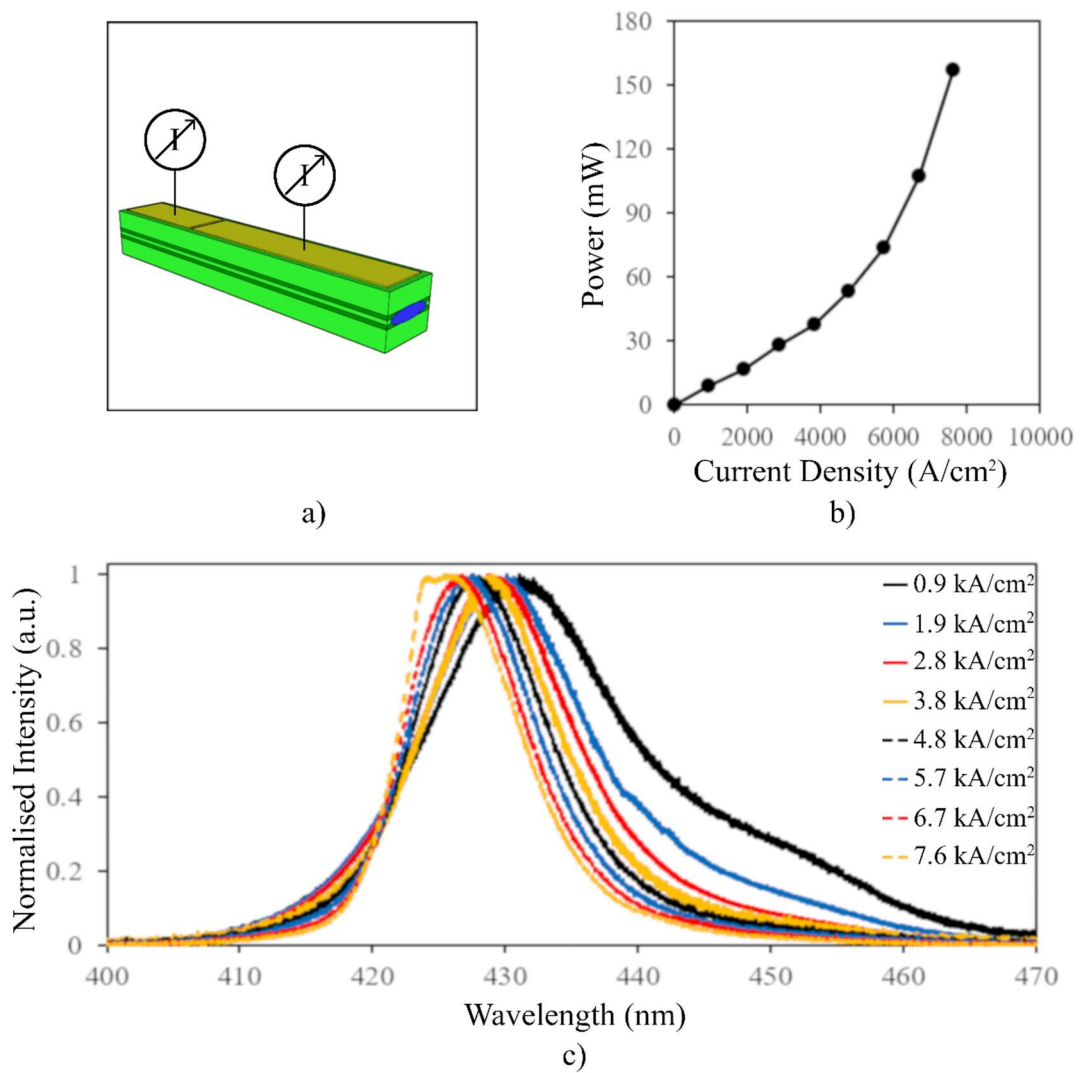


Figure 3-22 10µm GaN SLED following segmentation of the top contact with both sections driven together as one a) schematic b) optical output power for injected current density and c) emission spectra for various applied current densities

This suggests that although the lasing threshold may have been increased slightly by the FIB process, the device performance is otherwise unaffected. As with the 5µm wide SLED, a notable increase in output power is observed and is attributed to the same mechanism described earlier. Figure 3-22c) plots emission spectra as a function of wavelength for different levels of injected current applied to the device. All of the observed emission spectra are broad, smooth, and continuous, with no lasing peak visible as there was at 7.6kA/cm² in Figure 3-19d); although the ripple at the peak of 7.6kA/cm² suggests for current densities above this magnitude, lasing would occur.

3.6 Open-Circuit GaN SLED

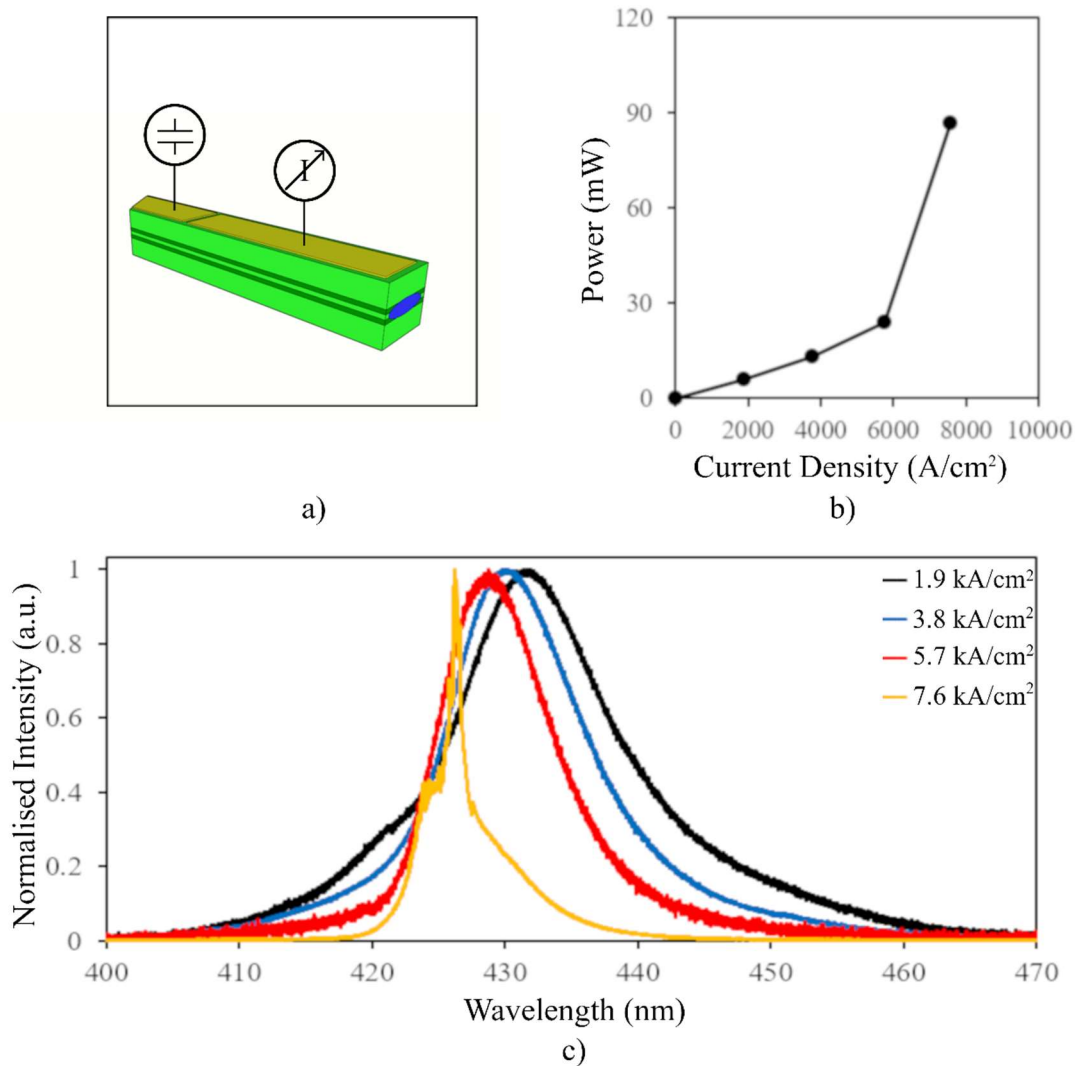


Figure 3-23 5µm GaN SLED following segmentation of the top contact with the front 2/3 driven and the rear 1/3 O/C a) schematic b) optical output power for injected current density and c) emission spectra for various applied current densities

Figure 3-23a) shows a schematic of the 5µm GaN SLED following the segmentation of the top contact using the FIB system and inclusion of an absorber. Current was injected into the front 2/3, with the rear 1/3 operated passively, or O/C. Figure 3-23b) plots optical output power as a function of current density. Super-linearity is observed, with similar performance when both sections were driven as one, as well as before segmentation was carried out. Figure 3-23c) plots emission spectra as a function of wavelength for different levels of

injected current. At 7.6kA/cm^2 a lasing peak at $\sim 425\text{nm}$ is visible, showing that the gain has overcome loss, and the device is no longer behaving as a SLED.

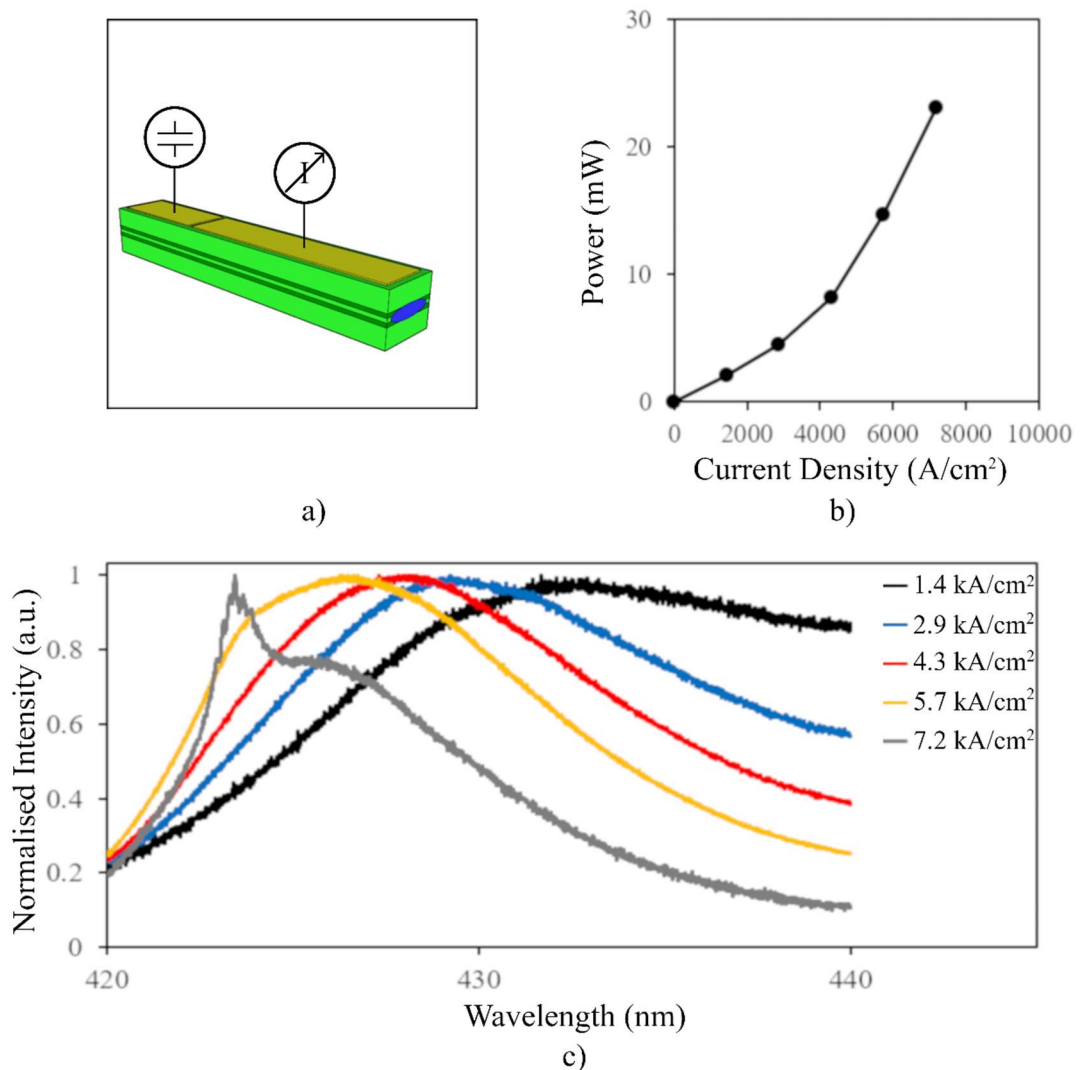


Figure 3-24 $10\mu\text{m}$ GaN SLED following segmentation of the top contact with the front 2/3 driven and the rear 1/3 O/C a) schematic b) optical output power for injected current density and c) emission spectra for various applied current densities

Figure 3-24a) shows a schematic of the $10\mu\text{m}$ GaN SLED following the segmentation of the top contact using the FIB system and inclusion of an absorber. The front 2/3 were driven, with the rear 1/3 O/C. Figure 3-24b) plots optical output power as a function of current density, again with super-linearity observed as when both sections were driven together and before segmentation was carried out. Figure 3-24c) plots emission spectra as a function of

wavelength for different levels of injected current. As above in Figure 3-23c), at 7.2kA/cm^2 a lasing peak at $\sim 425\text{nm}$ is visible. This slight reduction in threshold is also attributed to self-heating within the device, and influence from the absorber as backward travelling light pumps it into transparency.

Figure 3-25a) plots the bandwidth of the emission spectra as a function of injected current density for the $5\mu\text{m}$ GaN SLED when both sections are active, and when only the front 2/3 are active and the rear 1/3 is O/C. At low current densities, the bandwidth when both sections are active is equal to when the rear 1/3 is O/C and acting as an absorber. However, as the current density increases, the bandwidth when both sections are active reduces at a faster rate than when the rear 1/3 is O/C, demonstrating that the absorber is operating as anticipated.

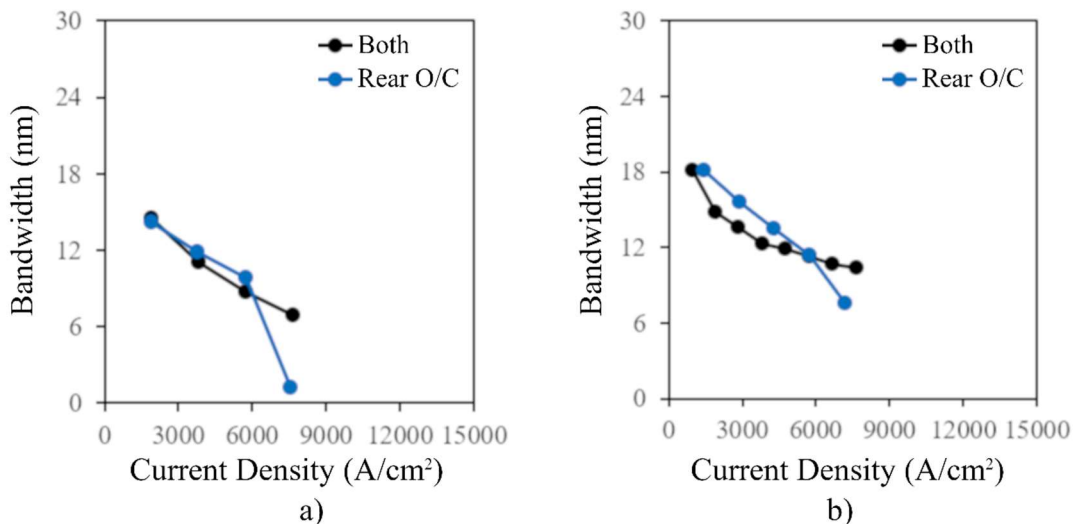


Figure 3-25 GaN SLEDs full width at half maximum values for injected current density when both sections are driven and when the rear section is O/C a) $5\mu\text{m}$ and b) $10\mu\text{m}$

Figure 3-25b) plots the bandwidth of the emission spectra as a function of injected current density for the $10\mu\text{m}$ GaN SLED when both sections are active, and when only the front 2/3 are active and the rear 1/3 is O/C. The bandwidths in both cases display a similar trend to those for the $5\mu\text{m}$ GaN SLED for current densities approaching 6kA/cm^2 , initially equal with smaller bandwidths observed for the same current densities when both sections are active.

As current densities increase above 6kA/cm^2 , the bandwidths become equal again before the bandwidth where the rear 1/3 is O/C reduces to $\sim 7\text{nm}$. This rapid reduction in bandwidth is a result of the SLED experiencing “burn through” [08] and starting to lase, confirmed by the lasing peak visible in Figure 3-24c) for 7.2kA/cm^2 . “Burn through” is discussed in Chapter One section 1.4.

3.7 Short-Circuit GaN SLED

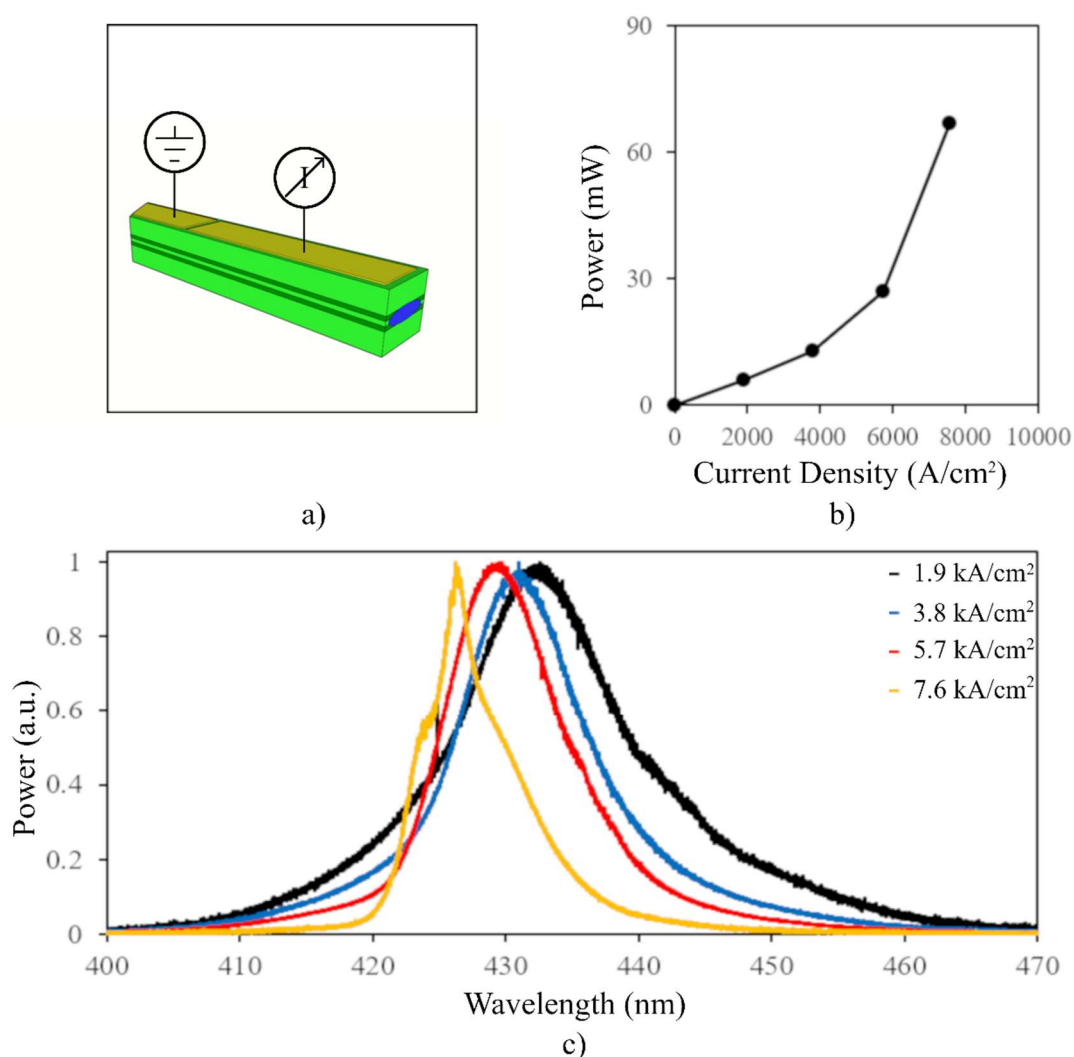


Figure 3-26 $5\mu\text{m}$ GaN SLED following segmentation of the top contact with the front 2/3 driven and the rear 1/3 S/C a) schematic b) optical output power for injected current density and c) emission spectra for various applied current densities

Figure 3-26a) shows a schematic of the 5 μm GaN SLED following the segmentation of the top contact using the FIB system and inclusion of an absorber. Current was injected into the front 2/3, with the rear 1/3 connected to ground, or S/C. Figure 3-26b) plots optical output power as a function of current density. Super-linearity is observed, and performance is similar to when both sections being driven as one, the front 2/3 were driven while the rear 1/3 was O/C, as well as before segmentation was carried out. Figure 3-26c) plots emission spectra as a function of wavelength for different levels of injected current. As with the rear 1/3 O/C, at 7.6kA/cm² a lasing peak at $\sim 425\text{nm}$ is visible, showing that the gain has overcome loss, and the device is no longer behaving as a SLED.

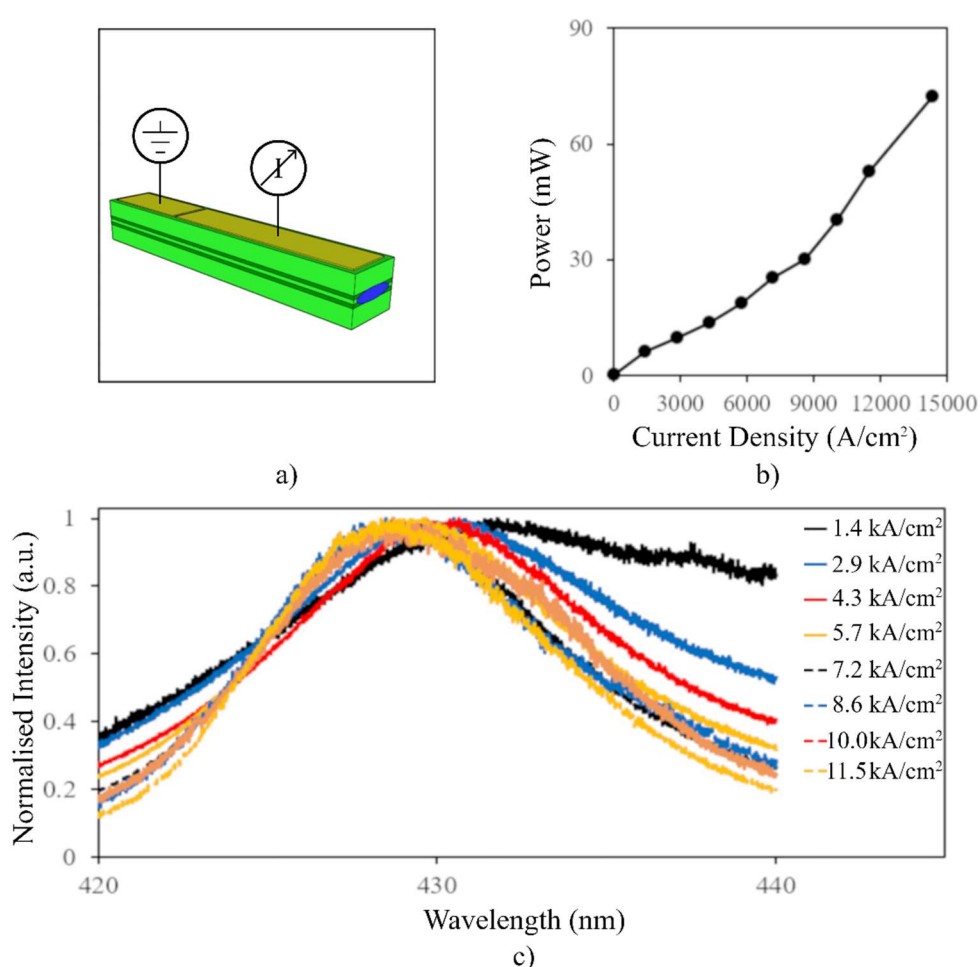


Figure 3-27 10 μm GaN SLED following segmentation of the top contact with the front 2/3 driven and the rear 1/3 S/C a) schematic b) optical output power for injected current density and c) emission spectra for various applied current densities

Figure 3-27a) shows a schematic of the 10 μ m GaN SLED following the segmentation of the top contact using the FIB system and inclusion of an absorber. The front 2/3 were driven, with the rear 1/3 connected to ground, or S/C. Figure 3-27b) plots optical output power as a function of current density. Super-linearity is again observed, but at lower current densities there is an impact on output power. This is attributed to the increased width of the absorber section slowing its saturation and therefore increasing its effectiveness.

As discussed in Chapter One section 1.4, by connecting the absorber to ground, it helps to prevent the accumulation of carriers within the absorber, increasing loss and delaying “burn through” [11]. Figure 3-27c) plots emission spectra as a function of wavelength for different levels of injected current. Unlike Figure 3-24c), no lasing peak is present for any injected current density, with that applied >50% greater than before the contact was segmented.

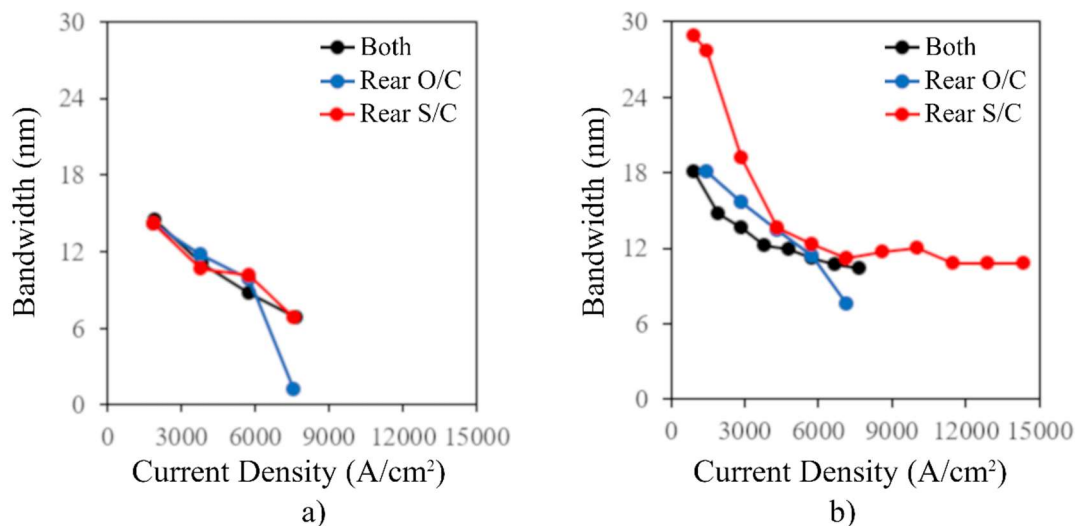


Figure 3-28 GaN SLEDs full width at half maximum values for injected current density when both sections are driven, when the rear section is O/C, and when the rear section is S/C a) 5 μ m and b) 10 μ m

Figure 3-28a) plots the bandwidth of the emission spectra as a function of injected current density for the 5 μ m GaN SLED when both sections are active, when only the front 2/3 are active and the rear 1/3 is O/C, and when only the front 2/3 are active and the rear 1/3 is S/C. For all the applied current densities, except for when the rear 1/3 is O/C and experiences

“burn though” at 7.2kA/cm^2 [08], all values of bandwidth are in good agreement with one another. Figure 3-28b) plots the bandwidth of the emission spectra as a function of injected current density for the $10\mu\text{m}$ GaN SLED when both sections are active, when only the front 2/3 are active and the rear 1/3 is O/C, and when only the front 2/3 are active and the rear 1/3 is S/C. Although all the bandwidths have similar values between 4kA/cm^2 and 7kA/cm^2 ; as the current density increases in the cases where both sections are driven and when the rear 1/3 is O/C, there is a continuous reduction in bandwidth resulting in lasing, whereas when the rear 1/3 is S/C the bandwidth initially reduces, but then appears to saturate at $\sim 1\text{nm}$.

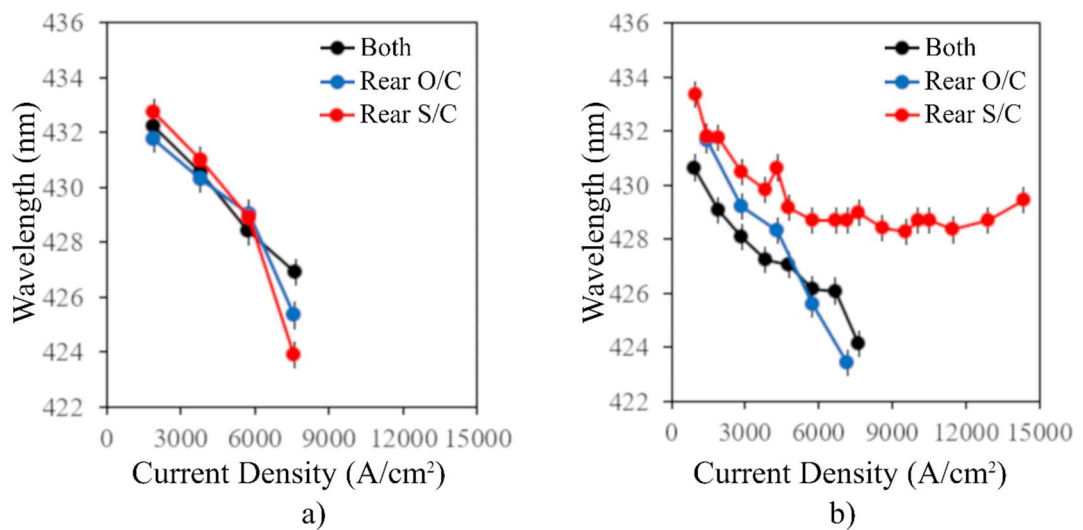


Figure 3-29 GaN SLEDs central wavelength for injected current density when both sections are driven, when the rear section is O/C, and when the rear section is S/C a) $5\mu\text{m}$ and b) $10\mu\text{m}$

Figure 3-29a) plots the central wavelength of the emission spectra as a function of injected current density for the $5\mu\text{m}$ GaN SLED when both sections are active, when only the front 2/3 are active and the rear 1/3 is O/C, and when only the front 2/3 are active and the rear 1/3 is O/C. For all the applied current densities, the behaviours of the central wavelength of the emission appears to be in good agreement, undergoing an average of a $\sim 7\text{nm}$ blueshift due to state filling [14,16]. Figure 3-29b) plots the central wavelength of the emission spectra as a function of injected current density for the $10\mu\text{m}$ GaN SLED when both sections are active, when only the front 2/3 are active and the rear section is O/C, and when only the front 2/3 are active and the rear section is S/C. Until 6kA/cm^2 the central wavelengths all follow the

same trend, a $\sim 5\text{nm}$ blueshift; for current densities above this threshold when the rear is S/C, the central wavelength is ‘pinned’ at $\sim 429\text{nm}$.

3.8 Point Spread Function

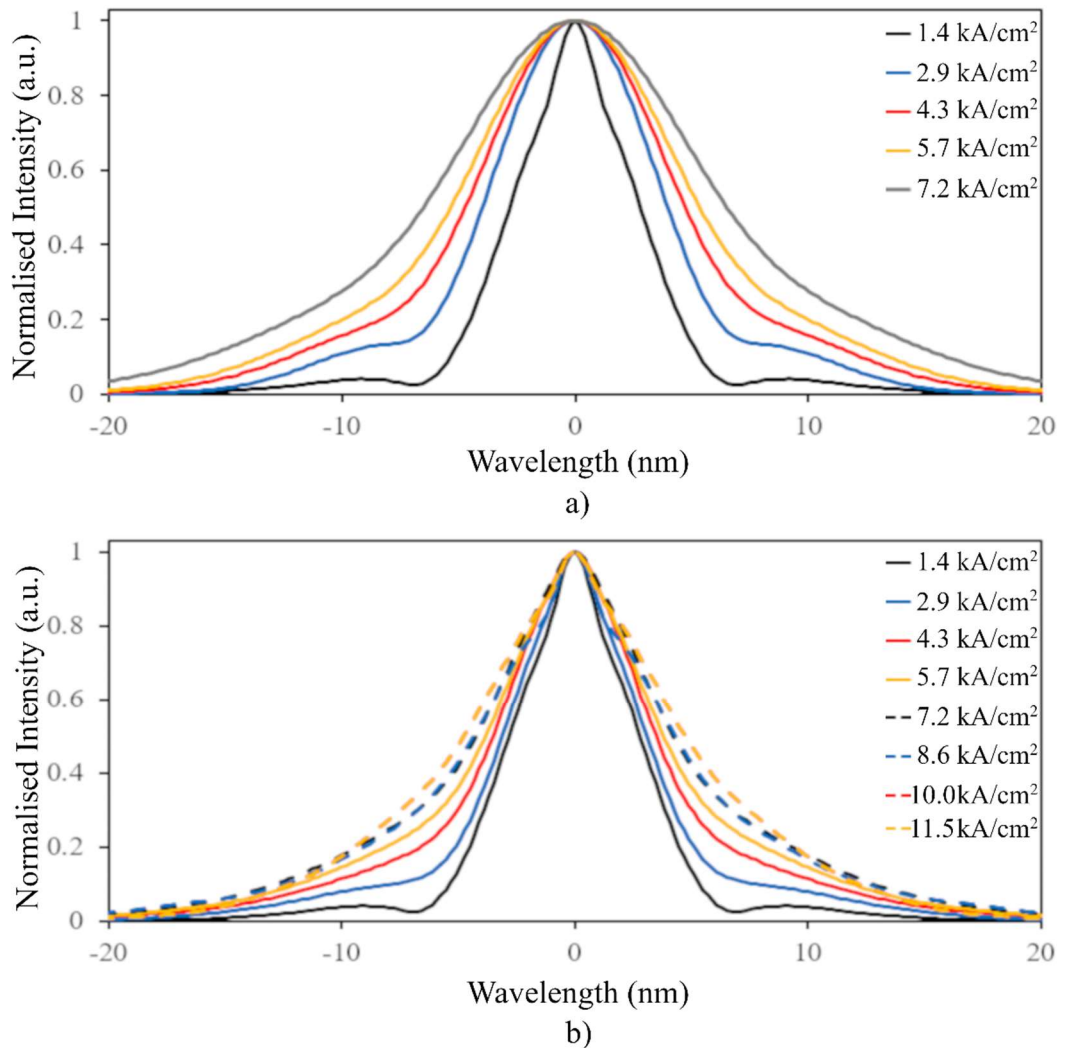


Figure 3-30 Point spread function calculated from the emission spectrum in the condition a) with the front 2/3 driven rear 1/3 O/C and b) with the front 2/3 driven rear 1/3 S/C

Figure 3-30a) plots the PSF calculated from the emission spectra as a function of displacement for the $10\mu\text{m}$ GaN SLED when only the front 2/3 are active and the rear 1/3 is O/C for different values of current density. The merits of the PSF measurement and the

method of its calculation are discussed in Chapter Two section 2.7. Figure 3-30b) plots the PSF calculated from the emission spectra as a function of displacement for the 10 μ m GaN SLED when only the front 2/3 are active and the rear 1/3 is S/C for different values of current density. As in Figure 2-10a) the half width at half maximum of the PSF gives the axial resolution of the system. For both cases, as the current density increases, predicted axial resolution decreases. The reduction in predicted axial resolution occurs more slowly when the rear 1/3 is S/C, and in a similar manner to the FWHM in Figure 3-27c) and Figure 3-28b), appears to saturate at $\sim 5.5\mu$ m.

Figures 3-31a-e) plot the PSF calculated from emission spectra as a function of displacement for the 10 μ m GaN SLED when the front 2/3 are active and the rear is O/C, and when the front 2/3 are active and the rear 1/3 is S/C for injected current densities between 1.4kA/cm² and 7.2kA/cm². Figure 3-31f) plots the axial resolution as a function of current density. Figure 3-31a) plots the PSF calculated from emission spectra as a function of displacement for the 10 μ m GaN SLED when the front 2/3 are active and the rear is O/C, and when the front 2/3 are active and the rear 1/3 is S/C with an injected current of 1.4kA/cm². Figure 3-31b) plots the PSF calculated from emission spectra as a function of displacement for the 10 μ m GaN SLED when the front 2/3 are active and the rear is O/C, and when the front 2/3 are active and the rear 1/3 is S/C with an injected current of 2.9kA/cm². Figure 3-31c) plots the PSF calculated from emission spectra as a function of displacement for the 10 μ m GaN SLED when the front 2/3 are active and the rear is O/C, and when the front 2/3 are active and the rear 1/3 is S/C with an injected current of 4.3kA/cm². Figure 3-31d) plots the PSF calculated from emission spectra as a function of displacement for the 10 μ m GaN SLED when the front 2/3 are active and the rear is O/C, and when the front 2/3 are active and the rear 1/3 is S/C with an injected current of 5.7kA/cm². Figure 3-31e) plots the PSF calculated from emission spectra as a function of displacement for the 10 μ m GaN SLED when the front 2/3 are active and the rear is O/C, and when the front 2/3 are active and the rear 1/3 is S/C with an injected current of 7.2kA/cm². Figure 3-31f) plots the axial resolution as a function of current density for the 10 μ m GaN SLED when only the front 2/3 are active and the rear 1/3 is O/C, and the front 2/3 are active and the rear 1/3 is S/C. At low current density (1.4kA/cm²), the axial resolution is the same for the O/C and S/C cases. However, as current density increases, there is a rapid diversion with a improved axial resolution maintained with the rear 1/3 S/C.

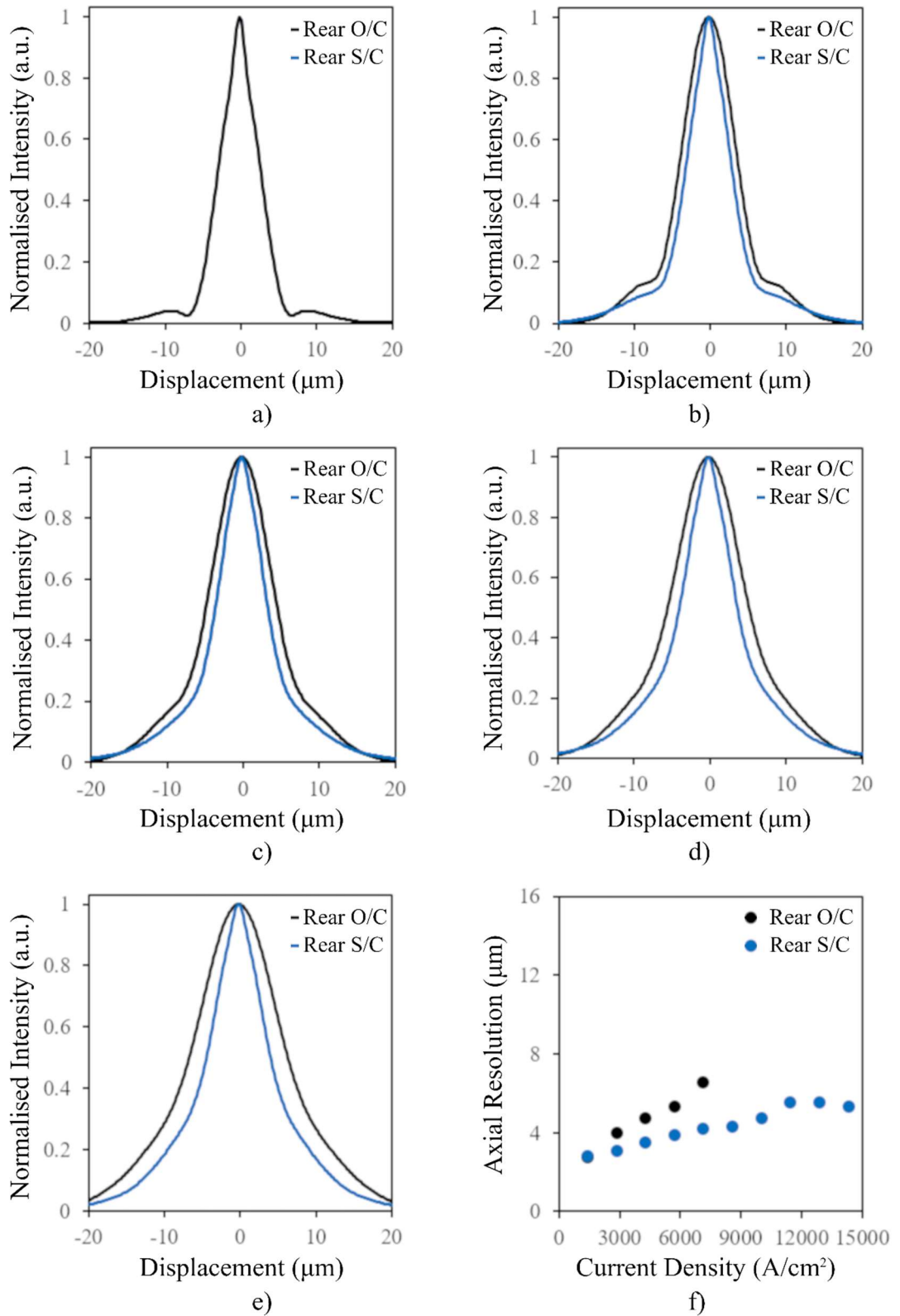


Figure 3-31 Point spread function calculated from the emission spectrum in the condition with the front 2/3 driven rear 1/3 O/C compared with the front 2/3 driven rear 1/3 S/C a) at 1.4kA/cm² b) at 2.9kA/cm² c) at 4.3kA/cm² d) at 5.7kA/cm² e) at 7.2kA/cm² and f) axial resolution for injected current density

3.9 Summary

In this chapter, the role of an absorber section within GaN SLEDs was explored further. A series of GaN laser diodes around three times longer than the commercially available laser diodes discussed in Chapter Two were fabricated in the University of Sheffield's National Centre for III-V Technologies. Producing bespoke devices allowed for control over the length and width of the waveguide, facet orientations, and accessibility of absorber sections. Once characterised, absorber sections were created using a FIB system, with an option to operate them O/C or short-circuit S/C.

Section 3.3 described the fabrication process performed to produce the GaN laser diodes and SLEDs from a 2 QW GaN substrate. Section 3.4 characterised GaN laser diodes and investigated the effect of increasing ridge width. Section 3.5 repeated elements of the characterisation carried out in section 3.4 following the use of a FIB system to convert the laser diodes into SLEDs, to ensure minimal damage was inflicted upon the devices. Section 3.6 examined the scenario when the absorber section of the SLED is operated in O/C, and section 3.7 when the absorber is operated in S/C. Section 3.8 reintroduced the PSF and extracted the predicted resolution of the devices.

3.10 Further Work

With the bias conditions of absorber sections now investigated for GaN, another area of interest is whether a multi-section SLED with three or more sections could be developed, and if the imposition of different magnitude current densities to the different sections of the SLED could help to engineer the device bandwidth. Such work has been successfully demonstrated using gallium arsenide and other material systems, but has yet to be conducted using GaN [28,29].

Throughout this chapter, devices with ridge widths of 5 μm and 10 μm were investigated, although an initial characterisation was carried out on a 15 μm wide ridge. This was due to the current source being unable to supply currents above 3A, equivalent to current densities above 7.6kA/cm² through the 15 μm wide ridge, or voltages above 10V [26]. As discussed and from Equation 3-2, as well as increasing the length of the waveguide, increasing its width should also give rise to SLEDs with higher powers [09] if the effect of self-heating can be overcome. With a larger active area, more absorption and spontaneous emission should take place, which could give rise to a wider bandwidth.

Described in section 3.3, which details the fabrication method used for the devices in Chapters Three and Four, the SLEDs were etched through the active region. Shallower etching which terminates above the active region offers lower loss, and therefore higher gain, but lowers the amount of spontaneous emission captured by the waveguide. As discussed in Chapter One sections 1.3, 1.4, and 1.9, SLED operation relies on amplified spontaneous emission, designed to have a high single, or at most a double, pass through the waveguide [30]. However, a shallow-etched SLED offers a lower reflectivity, thereby reducing the optical feedback, and making this approach worthy of examination.

References

- [01] T P Lee, C A Burrus Jr and B I Miller, "A Stripe Geometry Double-Heterostructure Amplified-Spontaneous-Emission (Superluminescent) Diode", *Journal of Quantum Electronics*, **9**, Number 8, pp820-828, August 1973.
- [02] E Feltn, A Castiglia, G Cosendey, L Sulmoni, J F Carlin, N Grandjean, Rossetti, J Dorsaz, V Laino, M Duelk and C Velez, "Broadband Blue Superluminescent Light-Emitting Diodes Based on GaN", *Applied Physics Letters*, **95**, pp081107-1-3, August 2009.
- [03] A Kafar, S Stanczyk, S Grzanka, R Czernecki, M Leszczynski, T Suski and P Perlin, "Cavity Suppression in Nitride Based Superluminescent Diodes", *Journal of Applied Physics*, **111**, pp083106-1-6, 2012.
- [04] K Bohm, P Marten, K Petermann, E Weidel and R Ulrich, "Low-Drift Fibre Gyro Using A Superluminescent Diode", *Electronics Letters*, **17**, Number 10, pp352-353, May 1981.
- [05] W K Burns, C L Chen and R P Moeller, "Fiber-Optic Gyroscopes with Broad-Band Sources", *Journal of Lightwave Technology*, **1**, Number 1, pp98-105, March 1983.
- [06] U T Schwarz, F Kopp, T Weig, C Eichler and U Strauss, "Superluminescent Light Emitting Diodes of 100mW Output Power for Pico-Projection", *Conference on Lasers and Electro-Optics Pacific Rim (CLEO-PR)*, pp1-2, June 2013.
- [07] F Kopp, "Superluminescent LED for Focus-Free Handheld Projection", *SPIE Newsroom*, 10.1117/2.1201302.004686, March 2013.
- [08] N S K Kwong, K Y Lau, N Bar-Chaim, I Ury and K J Lee, "High-Power, High Efficiency Window Buried Heterostructure GaAlAs Superluminescent Diode with Integrated Absorber", *Applied Physics Letters*, **51**, Number 23, pp1879-1881, December 1987.
- [09] G A Alphonse, D B Gilbert, M G Harvey and M Ettenberg, "High-Power Superluminescent Diodes", *Journal of Quantum Electronics*, **24**, Number 12, pp2454-2457, December 1988.

- [10] H Nagai, Y Noguchi, S Sudo, "High-Power, High-Efficiency 1.3 μ m Superluminescent Diode with a Buried Bent Absorbing Guide Structure", *Applied Physics Letters*, **54**, pp1719-1721, May 1989.
- [11] N S K Kwong, K Y Lau and N Bar-Chaim, "High-Power High-Efficiency GaAlAs Superluminescent Diodes with an Internal Absorber for Lasing Suppression", *Journal of Quantum Electronics*, **25**, Number 4, pp696-704, April 1989.
- [12] K Tateoka, H Naito, M Kume, K Hamada, H Shimizu, M Kazumura and I Teramoto, "A High-Power GaAlAs Superluminescent Diode with an Antireflective Window Structure", *Journal of Quantum Electronics*, **27**, Number 6, pp1568-1573, June 1991.
- [13] M Rossetti, J Dorsaz, R Rezzonico, M Duelk, C Velez, E Feltin, A Castiglia, G Cosendey, J F Carlin and N Grandjean, "High Power Blue-Violet Superluminescent Light Emitting Diodes with InGaN Quantum Wells", *Applied Physics Express*, **3**, pp061002-1-3, 2010.
- [14] K Holc, L Marona, R Czernecki, M Bockowski, T Suski, S Najda and P Perlin, "Temperature Dependence of Superluminescence in InGaN-Based Superluminescent Light Emitting Diode Structures", *Journal of Applied Physics*, **108**, pp013110-1-4, 2010.
- [15] F Kopp, T Lermer, C Eichler and U Strauss, "Cyan Superluminescent Light-Emitting Diode Based on InGaN Quantum Wells", *Applied Physics Express*, **5**, pp082105-1-3, 2012.
- [16] A Kafar, S Stanczyk, G Targowski, T Oto, I Makarowa, P Wisinieski, T Suski and P Perlin, "High-Optical-Power InGaN Superluminescent Diodes with "j-shape" Waveguide", *Applied Physics Express*, **6**, pp092102-1-4, 2013.
- [17] F Kopp, C Eichler, A Lell, S Tautz, J Ristic, B Stojetz, C Hoss, T Weig, U T Schwarz and U Strauss, "Blue Superluminescent Light-Emitting Diodes with Output Power Above 100mW for Picoprojection", *Japanese Journal of Applied Physics*, **52**, pp08JH07-1-5, 2013.
- [18] M Rossetti, J Napierala, N Matuschek, U Achattz, M Duelk, C Velez, A Castiglia, N Grandjean, A Dorsaz and E Feltin, "Superluminescent Light Emitting Diodes – The Best Out of Two Worlds", *Proceedings of SPIE*, Volume 8252, February 2012.
- [19] H Ohno, K Orita, M Kawaguchi, K Yamanaka and S Takigawa, "200mW GaN-Based Superluminescent Diode with a Novel Waveguide Structure", *IEEE Photonics Conference*, pp505-506, October 2011.
- [20] C Shen, T K Ng, J T Leonard, A Pourhashemi, S Nakamura, S P Denbaars, J S Speck, A Y Alyamani, M M El-Desouki and B S Ooi, "High-brightness Semipolar (2021) Blue

- InGaN/GaN Superluminescent Diodes for Droop-free Solid State Lighting and Visible-light Communications”, *Optics Letters*, **41**, Number 11, pp2608-2611, June 2016.
- [21] A Castiglia, M Rossetti, N Matuschek, R Rezzonico, M Duelk, C Velez, J-F Carlin and N Grandjean, “GaN-based Superluminescent Diodes with Long Lifetime”, *Proceedings of SPIE*, Volume 9748, February 2016.
- [22] A Kafar, S Stanczyk, P Wisniewski, T Oto, I Makarowa, G Targowski, T Suski and P Perlin, “Design and Optimization of InGaN Superluminescent Diodes”, *Physica Status Solidi A*, **212**, Number 5, pp997-1004, September 2014.
- [23] A Kafar, S Stanczyk, M Sarzynski, S Grzanka, J Goss, G Targowski, A Nowakowska-Siwinska, T Suski and P Perlin, “Nitride Superluminescent Diodes with Broadened Emission Spectrum Fabricated using Laterally Patterned Substrate”, *Optics Express*, **24**, Number 9, pp9673-9682, April 2016.
- [24] L A Coldren, S W Corzine and M L Masanovic, "Diode Lasers and Photonic Integrated Circuits", 2nd Edition, Wiley, 2012.
- [25] J Müller, M Scheubeck, M Sabathil, G Brüderl, D Dini, S Tautz, T Lerner, A Breidenassel and S Lutgen, “Gain Analysis of Blue Nitride-based Lasers by Small Signal Modulation”, *Applied Physics Letters*, **96**, Issue 13, March 2010.
- [26] ILX Lightwave, "User's Guide - Pulsed Current Source LDP - 3840B", June 2015.
- [27] A T Semenov, V R Shidlovski, S A Safin, V P Konyaev and M V Zverkov, "Superluminescent Diodes for Visible (670nm) Spectral Range Based on AlGaInP/GaInP Heterostructures with Tapered Grounded Absorber", *Electronics Letters*, **29**, Number 6, pp530-532, March 1993.
- [28] P D L Judson, K M Groom, D T D Childs, M Hopkinson and R A Hogg, "Multi-Section Quantum Dot Superluminescent Diodes for Spectral Shape Engineering", *IET Optoelectronics*, **3**, Number 2, pp100-104, November 2008.
- [29] R A Hogg, P D L Greenwood, D T D Childs, N Krstajic, K Kennedy, K M Groom, M Hugues, M Hopkinson, L E Smith, S J Matcher, M Bonesi, S Macneil and R Smallwood, "GaAs Based Quantum Dot Superluminescent Diodes for Optical Coherence Tomography of Skin Tissue", *International Conference on Computers and Devices for Communication*, pp1-6, December 2009.
- [30] M Rossetti, J Napierala, N Matuschek, U Achatz, M Duelk, C Velez, A Castiglia, N Grandjean, J Dorsaz and E Feltn, “Superluminescent Light Emitting Diodes – the Best Out of Two Worlds”, *Proceedings of SPIE*, Volume 8252, February 2012.

Chapter Four - Multi-Contact GaN SLEDs for Bandwidth Enhancement

4.1 Introduction to Chapter

Multi-section gallium arsenide (GaAs) [01-03] and indium phosphide (InP) [04,05] superluminescent light emitting diodes (SLEDs) have been shown to exhibit enhanced performance in lower power, broader bandwidth applications, such as optical coherence tomography (OCT) [06-08] and optical coherence microscopy (OCM) [09-11], compared to single contact devices [12,13]. Often, the term multi-section is used to refer to when the active section is coupled to a single absorber section, or a window, for the purpose of increasing the SLED lasing threshold, J_{th} , by reducing feedback within the device [01-05]. Chapter One introduced the concept of optical feedback and discussed various techniques that can be used to reduce it.

However, it has been demonstrated that by fabricating a multi-section device consisting of many independently driven sections, it is possible to control the spectral shape of the emission. Figure 4-1a) shows a schematic of the multi-section quantum dot (QD) SLED based on GaAs reported by Judson *et al.*, [14,15]. It features a 10mm long, 7 μ m wide ridge where the top contact has been segmented into ten, 1mm long isolated sections, S_1 - S_{10} . This was achieved by carrying out a 50 μ m etch of the p+ layer, resulting in isolation of \sim 2k Ω between sections whilst maintaining optical connectivity along the ridge. The front section, S_1 , was fabricated such that the waveguide was curved. This increases loss slightly within this section of the waveguide and reduces the amount of light reflected from the front facet that can be recoupled into the waveguide, whilst attempting to minimise the chip real estate allocated to it. The rear section, S_{10} , was designed as an absorber section, fabricated such that the waveguide gradually broadened from 7 μ m to 300 μ m and featured a tilted, deep-etched rear facet to prevent any backward propagating light from being reflected and making a double-pass through the waveguide [16]. This was left open-circuit (O/C).

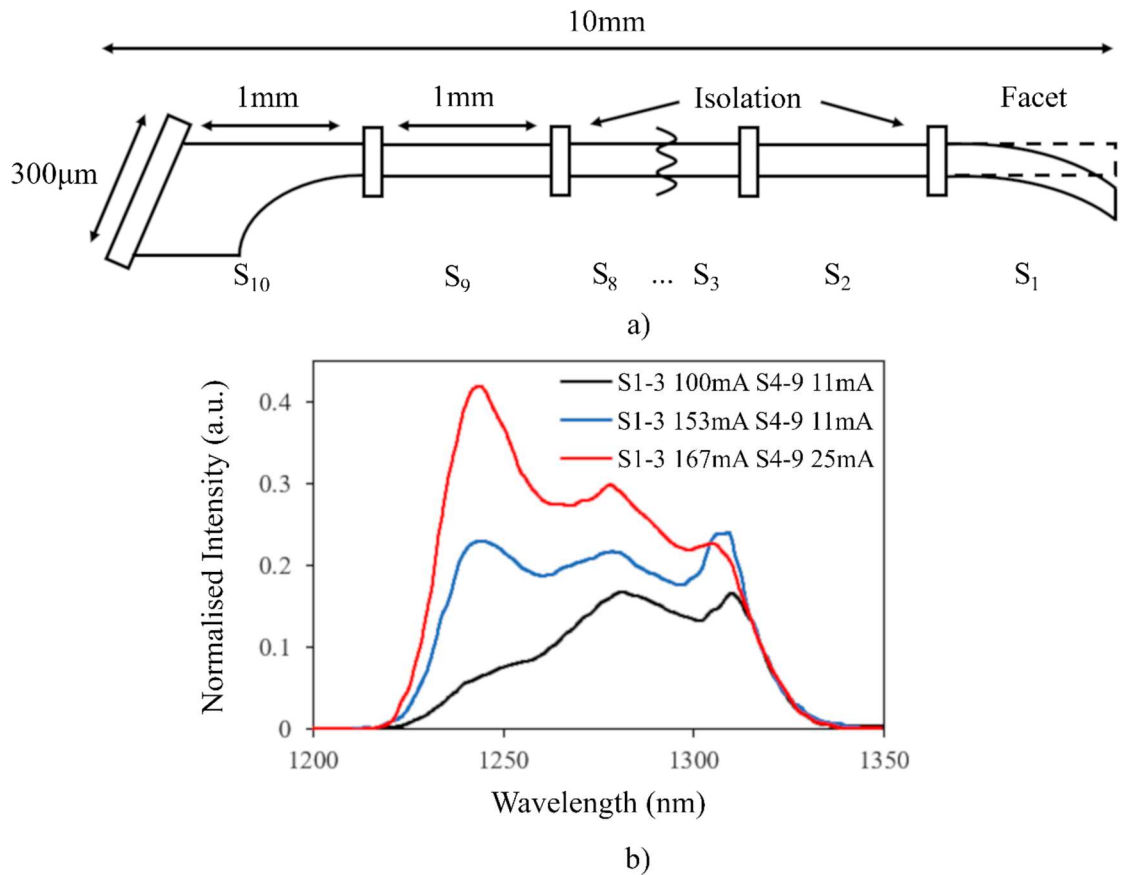


Figure 4-1 GaAs multi-section quantum dot SLED a) schematic and b) emission spectra for various applied current densities – Adapted from [14]

Figure 4-1b) plots normalised emission spectra as a function of wavelength for different levels of injected current applied to each of the sections in the GaAs QD SLED shown in Figure 4-1a). Increasing the current density increases the optical output power of the device and the emission spectrum is increasingly dominated by the excited states of the QDs. If the current density is decreased, the optical output power decreases and the emission spectrum becomes dominated by the ground states of the QDs. Figure 4-1b) demonstrates that for a multi-section SLED it is possible to manipulate the shape of the device emission spectra through the selection of appropriate current densities and where they are applied along the device. This is particularly advantageous when designing a device for OCT applications, as non-uniform emission spectra, with shapes similar to those given by the black or red lines in Figure 4-1b), could give rise to ghost images [17]. Thus far, development of gallium nitride (GaN) SLEDs has included angled facets [18-20], curved, or j shape, waveguides [21-24], and simple multi-section designs with O/C absorbers [25,26]; with limited work towards GaN multi-section SLEDs similar to the design depicted in Figure 4-1a).

Unlike GaAs and InP devices, c-plane (0001) GaN-based devices exhibit spontaneous and piezoelectric polarisation effects at internal interfaces causing strong electric fields in quantum wells (QWs), even at zero bias [27]. Additionally, for p-i-n structures, a forward bias increases the electric field in QWs due to field-sharing [28-30]. The calculated band diagrams of 2 indium gallium nitride (InGaN) InGaN/GaN-based QWs under zero and forward bias are plotted in Figure 4-2.

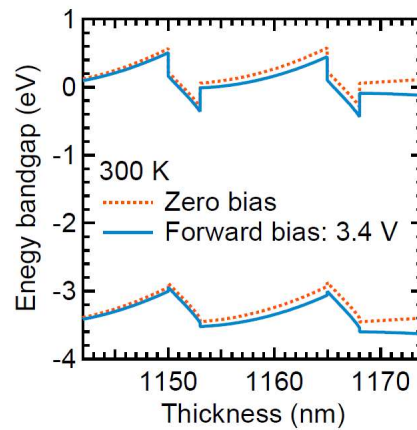


Figure 4-2 Schematic band diagrams of InGaN/GaN-based quantum wells under zero and forward bias at 300K – Courtesy of Professor Yukihiro Harada, University of Kobe [31]

Energy levels were calculated using the single-band Schrödinger equation for the conduction band and six-band k.p theory for the valence band. Fundamental transition energies of the InGaN-based QWs are 2.97eV (n-side QW₁) and 2.94eV (p-side QW₂), respectively, at zero bias. These transition energies blueshift by ~0.01eV at a forward bias of 3.4V due to the reduction in the electric field.

4.2 Outline of Chapter

In this chapter, the effect of operating three section GaN SLEDs is investigated for what is believed to be for the first time, with a particular focus on the impact three sections have the spectral shape. The 5 μ m GaN SLED with the angled rear facet characterised throughout Chapter Three was further modified using a focused ion beam (FIB) system; producing three

equal length, optically connected but electrically isolated, sections which could be driven independently of one another, and with an option to operate them O/C or short-circuit (S/C).

Section 4.3 repeats the characterisation of the 5 μm GaN SLED after the use of a FIB system to modify the device to produce three sections, with the front 1/3 driven and the rear 2/3 O/C. Section 4.4 repeats elements of the characterisation carried out in section 4.3 with the front 2/3 driven and the rear 1/3 O/C. Section 4.5 repeats elements of the characterisation carried out in sections 4.3 and 4.4 with the front 2/3 driven and the rear 1/3 S/C. Section 4.6 investigates the effect each case has on the central wavelength of the emission spectra and the associated bandwidth. Section 4.7 examines the effect varying the current density to each section has on the SLED bandwidth. Section 4.8 introduces the Rayleigh criterion and discusses the resolution limit of the SLED tested.

This forms the work published in my Applied Physics Letter.

4.3 Multi-Section GaN SLED

Figure 4-3a) (inset) shows a schematic of the 5 μm GaN SLED discussed in Chapter Three and fabricated using the process described in Chapter Three section 3.3, following the use of the FIB system to segment the contact for a second time. Now separated into three sections each $\sim 850\mu\text{m}$ long, an isolation of $1.25\text{k}\Omega$ was achieved between the middle 1/3 and rear 1/3 sections; with an isolation of $5\text{M}\Omega$ between the front 1/3 and middle 1/3 sections, as disclosed in Chapter Three. The FIB system and contact segmentation details are described in Chapter Two section 2.5. As shown in Figure 4-3a), only the front 1/3 was driven, with the middle 1/3 and rear 1/3 remaining O/C. Figure 4-3b) plots voltage as a function of current density for each section and the device before the contact was segmented with the FIB system. Concerns regarding whether the device would undergo too much self-heating following the FIB process meant these measurements were conducted to $\sim 200\text{A}/\text{cm}^2$, $\sim 1/2$ of the level than before segmentation. However, for the range in which the measurements

overlap with those obtained before segmentation they demonstrate a good fit, as they do amongst themselves, suggesting that each section has similar electrical characteristics.

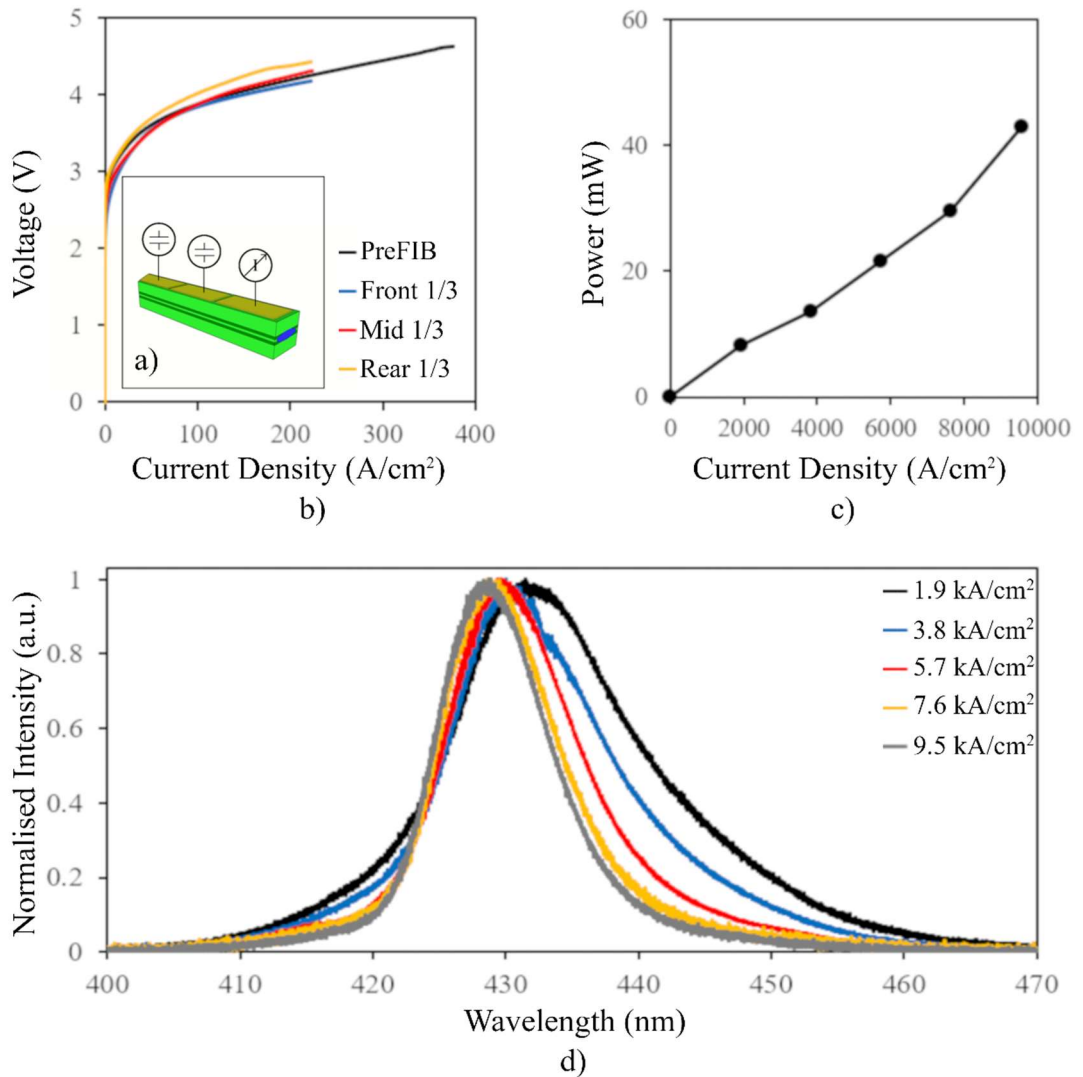


Figure 4-3 $5\mu\text{m}$ GaN SLED following the second segmentation of the top contact with the front 1/3 driven and the rear 2/3 O/C a) schematic b) voltage for injected current density c) optical output power for injected current density and d) emission spectra for various applied current densities

Figure 4-3c) plots optical output power as a function of current density, with super-linearity observed confirming that the device is still a SLED. Figure 4-3d) plots emission spectra as a function of wavelength for different levels of injected current applied to the device. For the full range of current densities, 1.9, 3.8, 5.7, 7.6, and 9.6 kA/cm^2 , the observed emission

spectra are broad, smooth, and continuous, with no visible lasing peak; but spectral ripple can be seen at the peak of the spectra, indicating the presence of optical gain, confirming the assertion that the device is superluminescent. This result is expected, as even with the application of higher current densities, 2/3 of the device is now in loss, and lasing was not observed after the first segmentation of the top contact when the full length of the device was driven as one.

4.4 Open-Circuit Multi-Section GaN SLED

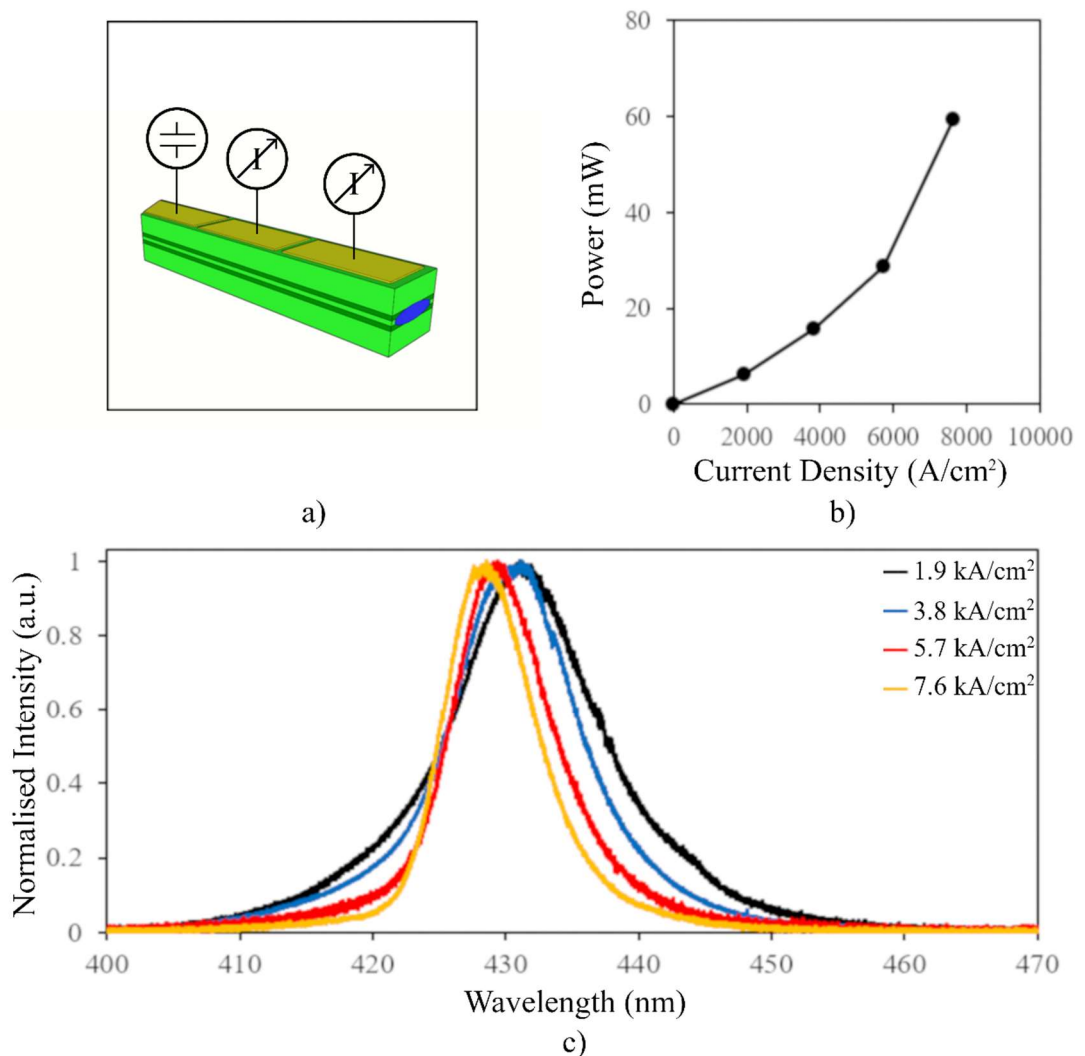


Figure 4-4 5μm GaN SLED following the second segmentation of the top contact with the front 2/3 driven and the rear 1/3 O/C a) schematic b) optical output power for injected current density and c) emission spectra for various applied current densities

Figure 4-4a) shows a schematic of the 5 μ m GaN SLED following the second segmentation of the top contact using the FIB system. The front 2/3 was driven from the same current source, with the rear 1/3 remaining O/C. Figure 4-4b) plots optical output power as a function of current density. Super-linearity is observed as in Figure 4-3c) but is more pronounced for the current densities applied. The higher powers, and enhanced super-linearity are attributed to the doubling of length of the gain region, confirming that which was discussed with the introduction of Equations 3-1 and 3-2 [02,32]. Figure 4-4c) plots emission spectra as a function of wavelength for different levels of injected current applied to the device. For the full range of current densities, 1.9, 3.8, 5.7, 7.6, and 9.6kA/cm², the observed emission spectra are broad, smooth, and continuous, with no visible lasing peak; but spectral ripple can be seen at the peak of the spectra confirming the assertion that the device is superluminescent.

4.5 Short-Circuit Multi-Section GaN SLED

Figure 4-5a) shows a schematic of the 5 μ m GaN SLED following the second segmentation of the top contact using the FIB system. The front 2/3 was driven using the same current source, with the rear 1/3 operated S/C via a connection to ground. Figure 4-5b) plots optical output power as a function of current density. Although super-linearity is still observed as seen in Figure 4-4b), it is much less pronounced and the magnitude of the optical output power of the device has also reduced. This is because by providing a path to ground, carriers are prevented from accumulating in the absorber section and contributing to gain [05,33,34]. Figure 4-5c) plots emission spectra as a function of wavelength for different levels of injected current applied to the device. Although the emission spectra are still broad, smooth, and continuous, such as those in Figures 4-3d) and 4-4c), operating the absorber in S/C has a noticeable effect on the longer wavelength portion of the spectrum. In Figures 4-3d) and 4-4c), as the current density increases, the central wavelength, λ_0 , undergoes a prominent blue-shift, with the wavelengths longer than λ_0 blue-shifting by a similar amount, whilst the wavelengths shorter than λ_0 remained fixed. As can be seen in Figure 4-5c), as the current density increases, λ_0 and the wavelengths greater than λ_0 remain largely fixed. This is attributed to backward propagating light being absorbed in the absorber before spontaneous

emission into the amplifier section, termed “recycling”, resulting in a broader spectrum of light being amplified.

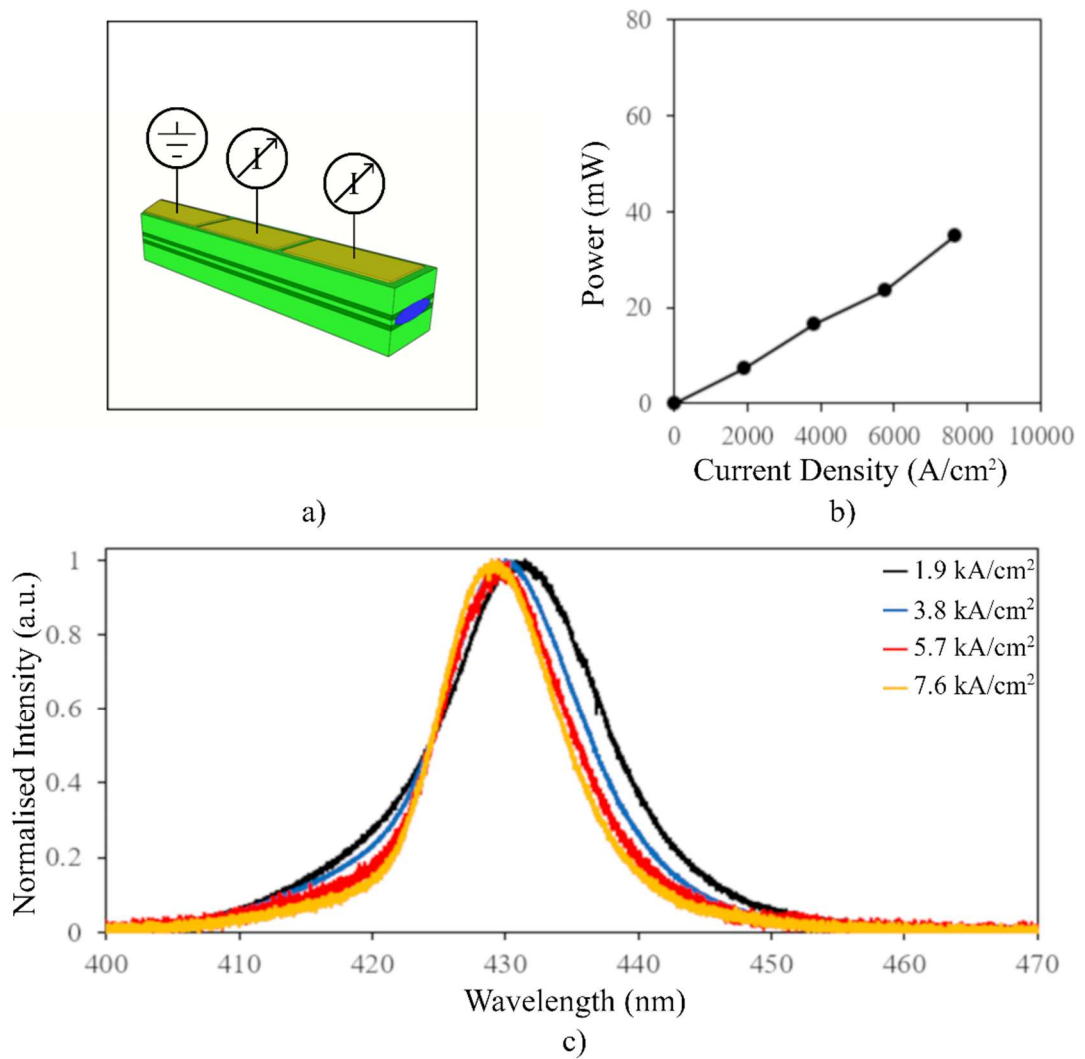


Figure 4-5 5μm GaN SLED following the second segmentation of the top contact with the front 2/3 driven and the rear 1/3 S/C a) schematic b) optical output power for injected current density and c) emission spectra for various applied current densities

4.6 Bandwidth Discussion

Figure 4-6a) plots the central wavelength of the emission spectra as a function of injected current density for the 5μm GaN SLED when only the front 1/3 is active and the rear 2/3 are

O/C, when only the front 2/3 are active and the rear 1/3 is O/C, and when only the front 2/3 are active and the rear 1/3 is S/C. When the front 2/3 are active, the behaviours of the central wavelength of the emission are in good agreement with those in Figure 3-29a) in Chapter Three between 2kA/cm^2 and 6kA/cm^2 , with the same $\sim 4\text{nm}$ blueshift observed. Between 6kA/cm^2 and 8kA/cm^2 the relatively large $\sim 4\text{nm}$ blueshift exhibited in Figure 3-29a) is now a more moderate $\sim 1\text{nm}$. This is attributed to minor damage inflicted on the waveguide during the second modification using the FIB system preventing some light being coupled between the two sections.

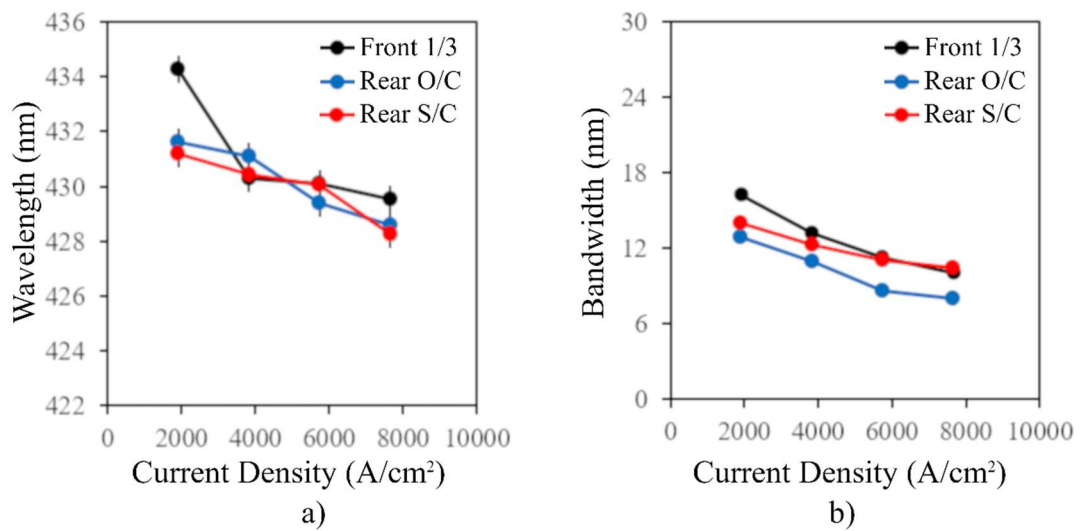


Figure 4-6 $5\mu\text{m}$ GaN SLED when the front 1/3 is driven with rear 2/3 O/C, the front 2/3 is driven with rear 1/3 O/C, and the front 2/3 is driven with rear 1/3 S/C a) central wavelength for injected current density and b) full width at half maximum for injected current density

When the front 1/3 is active and the rear 2/3 are O/C, at 2kA/cm^2 , the central wavelength is at a comparatively long wavelength, 434nm , before reducing to 430nm as the current density is increased. Although the mechanism behind the shift in the central wavelength is due to a combination of state filling [20,26], and the spontaneous and piezoelectric polarisation effects at internal interfaces discussed in section 4.1 [27-30], this behaviour highlights one of the advantages of a multi-section GaN device – the ability to vary the central wavelength of the emission spectra from section to section. Figure 4-6b) plots the bandwidth of the emission spectra as a function of injected current density for the $5\mu\text{m}$ GaN SLED when only

the front 1/3 is active and the rear 2/3 are O/C, when only the front 2/3 are active and the rear 1/3 is O/C, and when only the front 2/3 are active and the rear 1/3 is S/C. For all the applied current densities, the trends of the three bandwidth curves are in good agreement with one another, but there is an enhancement in the cases where the rear 1/3 is S/C, and when only the front 1/3 is active.

When the rear 1/3 is S/C, at low current densities the FWHM is a similar magnitude to when the rear 1/3 is O/C, but as the current density increases the magnitude reduces at a slower rate. This is because with the absorber operated in S/C the accumulation of carriers in the absorber occurs at a slower rate, as is discussed in Chapter One section 1.4. When only the front 1/3 is active, at low current densities it offers the greatest bandwidth, approaching 18nm; but as current density increases, this quickly reduces to the same magnitude as when the rear 1/3 is S/C and at 8kA/cm² offers a smaller FWHM.

4.7 Varying Current in Sections

Figure 4-7a) shows a schematic of the 5 μ m GaN SLED following the second segmentation of the top contact using the FIB system. The front 1/3 was driven with current density 'a' and the middle 1/3 was driven with current density 'b', with the rear 1/3 O/C. Figure 4-7b) plots the FWHM as a function of optical output power. Figure 4-7c) plots emission spectra as a function of wavelength for different levels of injected current applied to the device. The values of 'a' and 'b' are multiples of $\sim 1.9\text{kA/cm}^2$, with the sum of the coefficients of 'a' and 'b' equal to 4. If the condition where the coefficients of 'a' and 'b' are both equal to 2 is considered, an emission bandwidth of $\sim 11\text{nm}$ and optical output power of $\sim 4.2\text{mW}$ is observed. As the coefficient of 'b' is increased, the emission bandwidth narrows to $\sim 10\text{nm}$ while the optical output power increases to $\sim 11.9\text{mW}$. As the coefficient of 'a' is increased, the emission bandwidth broadens to $\sim 15.8\text{nm}$ while the optical output power decreases to $\sim 0.9\text{mW}$. This suggests that for enhanced emission bandwidth the coefficient of 'a' is the dominant factor, and the coefficient of 'b' should remain comparatively low. This is contrary to the work of Judson *et al.*, where the sections closest to the emission facet were at highest current densities [14,15].

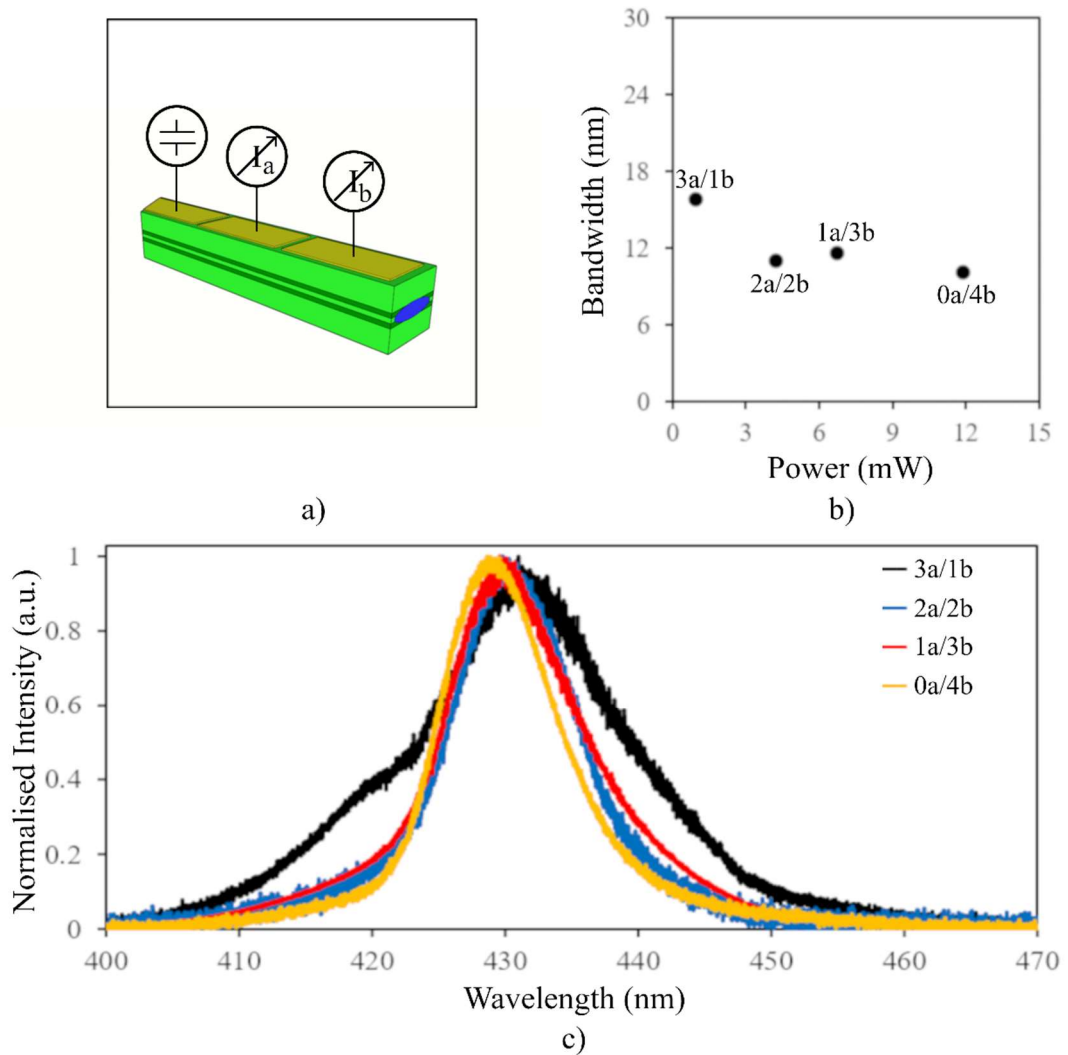


Figure 4-7 5μm GaN SLED following the second segmentation of the top contact with the front 2/3 driven at current densities ‘a’ and ‘b’, respectively, and the rear 1/3 O/C a) schematic b) full width at half maximum values for optical output power and c) emission spectra for various applied current densities

Figure 4-8a) shows a schematic of the 5μm GaN SLED following the second segmentation of the top contact using the FIB system. The front 1/3 was driven with current density ‘a’ and the middle 1/3 was driven with current density ‘b’, with the rear 1/3 S/C. Figure 4-8b) plots the FWHM as a function of optical output power. Figure 4-8c) plots emission spectra as a function of wavelength for different levels of injected current applied to the device, from which the bandwidth values were extracted. As in Figure 4-7b) and Figure 4-7c), the values of ‘a’ and ‘b’ are multiples of $\sim 1.9\text{kA/cm}^2$; however, the sum of their coefficients is no longer 4, and the coefficient of ‘b’ is kept at 1.

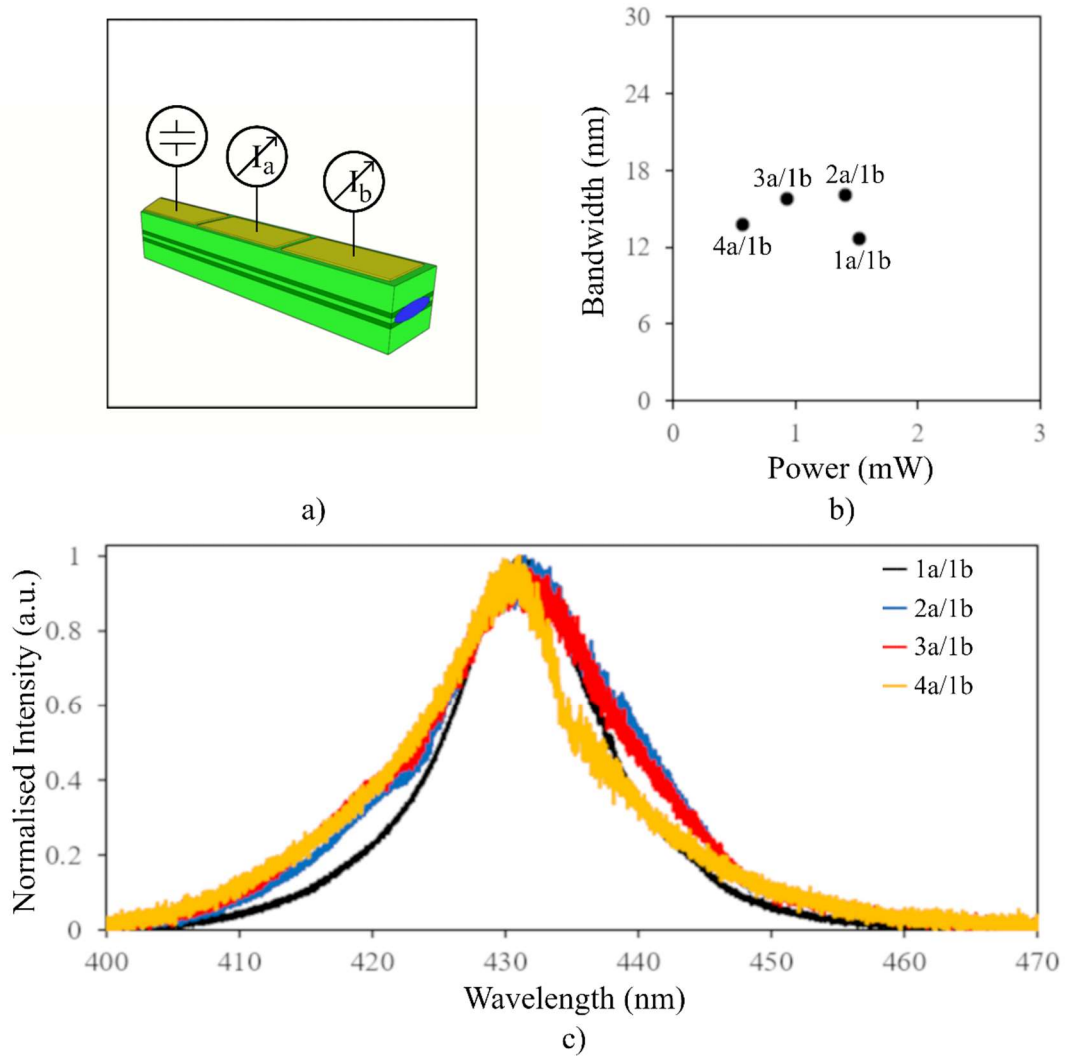


Figure 4-8 5μm GaN SLED following the second segmentation of the top contact with the front 2/3 driven at current densities 'a' and 'b', respectively, and the rear 1/3 O/C a) schematic b) full width at half maximum values for optical output power and c) emission spectra for various applied current densities

If the condition where the coefficients of 'a' and 'b' are both equal to 1 is considered, an emission bandwidth of ~12.6nm and optical output power of ~1.5mW is observed. If the coefficient of 'a' is increased to 2, the emission bandwidth broadens to ~16nm while the optical output power decreases to ~1.4mW. If the coefficient of 'a' is increased to 3, the emission bandwidth narrows slightly to ~15.8nm while the optical output power decreases to ~0.9mW. If the coefficient of 'a' is further increased to 4, the emission bandwidth narrows to ~13.7nm while the optical output power decreases to ~0.6mW.

Having now determined an optimal drive scheme for the active elements, the beneficial effects of S/C over S/C absorbers described in Chapter Three section 3.6 are employed.

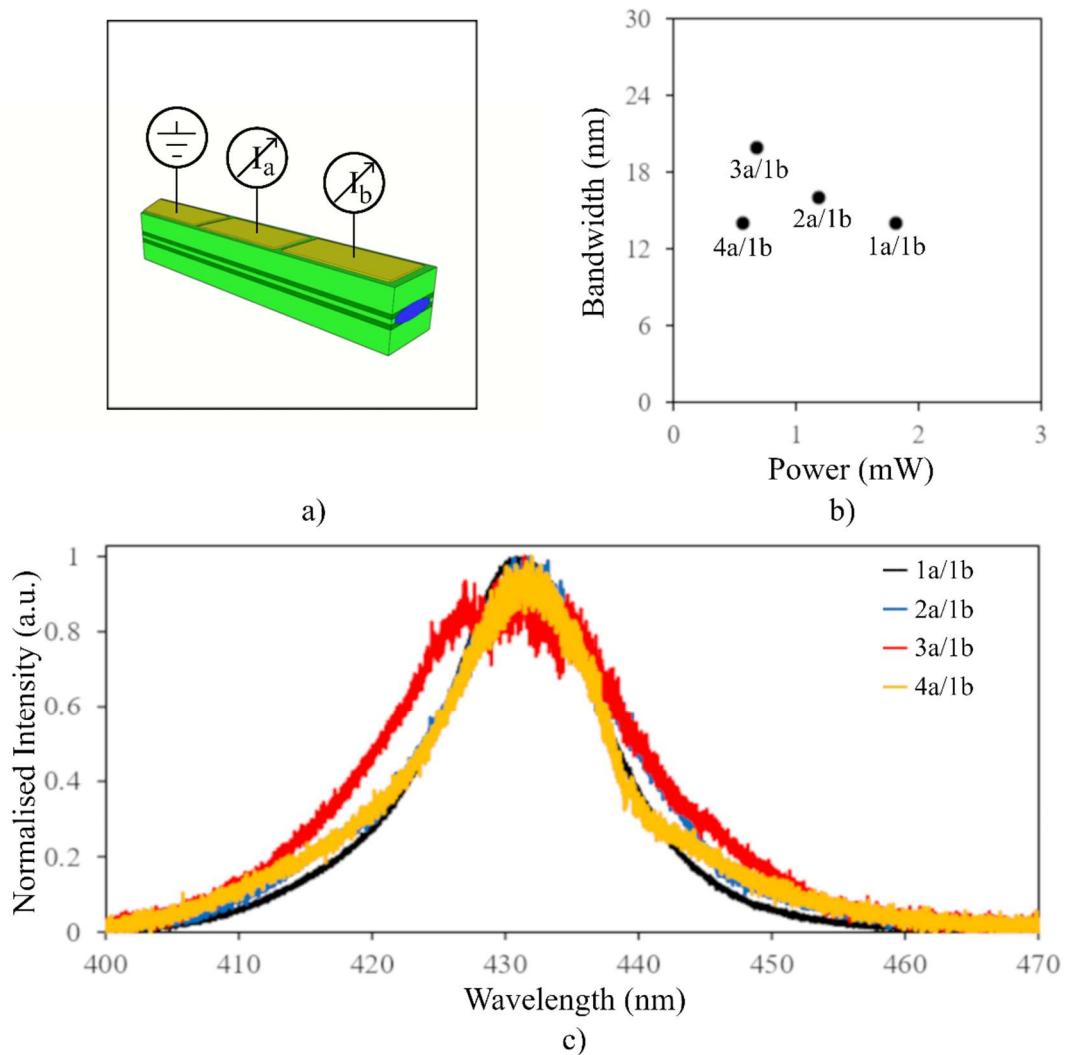


Figure 4-9 5μm GaN SLED following the second segmentation of the top contact with the front 2/3 driven at current densities ‘a’ and ‘b’, respectively, and the rear 1/3 S/C a) schematic b) full width at half maximum values for optical output power and c) emission spectra for various applied current densities

Figure 4-9a) shows a schematic of the 5μm GaN SLED following the second segmentation of the top contact using the FIB system. Following the same experimental procedures as described for Figure 4-8a)-c), but with a S/C absorber, Figures 4-9a)-c) are obtained. If the condition where the coefficients of ‘a’ and ‘b’ are both equal to 1 is considered, an emission

bandwidth of $\sim 14\text{nm}$ and optical output power of $\sim 1.8\text{mW}$ is observed. If the coefficient of 'a' is increased to 2, the emission bandwidth broadens to $\sim 16\text{nm}$ while the optical output power decreases to $\sim 1.2\text{mW}$. If the coefficient of 'a' is increased to 3, the emission bandwidth broadens further to $\sim 20\text{nm}$ while the optical output power decreases to $\sim 0.7\text{mW}$. If the coefficient of 'a' is further increased to 4, the emission bandwidth returns to $\sim 14\text{nm}$ while the optical output power decreases further to $\sim 0.6\text{mW}$.

For OCT imaging, a broad emission bandwidth is essential for high resolution images with only a moderate optical output power required [06-09,35], as discussed in Chapter One sections 1.5 and 1.6. As such, the condition where the coefficient of 'a' is equal to 3 could be used to conduct measurements.

4.8 Rayleigh Criterion

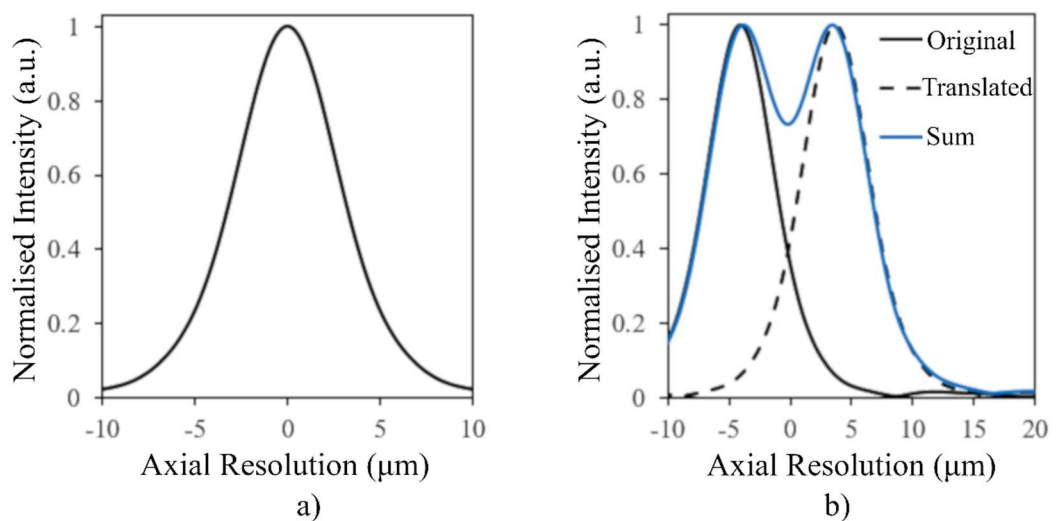


Figure 4-10 Point spread function a) calculated from the emission spectrum in the 3a/1b condition with the rear 1/3 S/C and b) translated to incorporate the Rayleigh criterion

Figure 4-10a) plots the PSF calculated from the emission spectrum shown in Figure 4-9c) for the condition 3a/1b. As discussed in Chapter Two section 2.5, the PSF is a widely

accepted method of determining the resolution of an optical emitter [28,35-38], with the axial resolution equal to value of the half width at half maximum of the PSF. For the PSF shown in Figure 4-10a) this is $\sim 3.3\mu\text{m}$. However, this value of gives the maximum axial resolution a specific optical emitter can achieve, not the maximum axial resolution that can be expected within an OCT system. To discern this value, the Rayleigh criterion must be considered [36]. Figure 4-10b) plots the PSF from Figure 4-10a) twice, translating the duplicate (dashed) along the x-axis until the sum of the duplicate and the original displays a dip of 26.3% between the two peaks. For Figure 4-10b) the axial resolution once the Rayleigh criterion is satisfied is $\sim 6.7\mu\text{m}$.

4.9 Summary

In this chapter, the effect of operating a GaN SLED with three sections was investigated, with a particular focus on the impact three sections have on the spectral shape. The $5\mu\text{m}$ GaN SLED with the angled rear facet characterised throughout Chapter Three was further modified using a FIB system; producing three equal length, optically connected but electrically isolated, sections which were driven independently of one another, and with an option to operate them O/C or S/C if no current is injected into them.

Section 4.3 repeated the characterisation of the $5\mu\text{m}$ GaN SLED after the use of a FIB system to modify the device to produce three sections, with the front 1/3 driven and the rear 2/3 O/C. Section 4.4 repeated elements of the characterisation carried out in section 4.3 with the front 2/3 driven and the rear 1/3 O/C. Section 4.5 repeated elements of the characterisation carried out in sections 4.3 and 4.4 with the front 2/3 driven and the rear 1/3 S/C. Section 4.6 investigated the effect each case has on the central wavelength of the emission spectra and the associated bandwidth. This is carried out using the same current density, and so is akin to changing the active length of a single-contact SLED. Section 4.7 examined the effect varying the current density applied to each section had on the SLED bandwidth. A $\sim 2\text{nm}$ enhancement of the FWHM was obtained using asymmetric drive currents to the active elements, with a further $\sim 4\text{nm}$ enhancement when using a S/C absorber section as compared

to O/C, demonstrating a ~6nm total bandwidth enhancement. Section 4.8 introduced the Rayleigh criterion and discussed the resolution limit of the SLED tested.

4.10 Further Work

Simulation of a SLED output power and spectrum requires a knowledge and understanding of a broad range of material and device parameters, such as the gain and spontaneous emission spectra as a function of current, both as a function of temperature. For III-nitride materials like GaN, the effect of the in-built piezoelectric fields [27,28,30], also needs to be considered. Although some simulation of GaN SLEDs has been reported by Matuschek *et al.*, their model was seemingly produced alongside experimentation of well-understood devices, which informed their model of some of the aforementioned parameters [39]. The devices analysed in Chapter Two section 2.3 could be used to provide some of these parameters, for example the optical output power as a function of current density, as those devices tested were all shown to have a similar performance in good agreement with their datasheet [40].

However, some parameters required for the simulation are not as easily measured. As the aim would be to accurately model a multi-section GaN SLED, the self-heating effects with drive current would need to be known, both within each section and longitudinally along the waveguide. With the inhomogeneity of the QW needing to be accommodated this cannot be done *ab initio* and could not be simply extracted from the model. If the adopted approach was to measure the self-heating effects experimentally and then use the results to inform the simulation, as the number of sections increases the setup becomes ever more complex. Each section of the SLED would need access for a temperature probe, while also providing enough isolation from the adjacent temperature probes to prevent any influence on the reading.

One possible simplification is that the Hakki-Paoli method of gain measurement allows the cavity temperature change to be calculated [41], but this cannot be applied longitudinally to determine the temperature of sections when they are being independently driven at different

current densities. Additionally, with the wide span of current densities required to perform these measurements, the Hakki-Paoli method would be unlikely to be appropriate across the whole range. For low current densities, the segmented contact method of gain measurement should be considered [42]; however, at higher current densities, Hakki-Paoli would be the preferred method to use [41]. The divergent device types required for characterisation, and additional spatial thermal characterisation of the device makes the collection of a suitable dataset time consuming.

All these factors make simulation of the multi-section SLED highly challenging, and almost require an experimental approach in tandem with simulation for success [39].

If an empirical approach is required, a finer set of drive conditions is essential, with more active contacts allowing for greater tunability. Machine learning could then be adopted to discover the optimal drive conditions for the device. An aspect not explored to date is the effect of using a reverse bias on the absorber section, and this is worthy of further work.

References

- [01] H Nagai, Y Noguchi, S Sudo, "High-Power, High-Efficiency 1.3 μ m Superluminescent Diode with a Buried Bent Absorbing Guide Structure", *Applied Physics Letters*, **54**, pp1719-1721, May 1989.
- [02] N S K Kwong, K Y Lau and N Bar-Chaim, "High-Power High-Efficiency GaAlAs Superluminescent Diodes with an Internal Absorber for Lasing Suppression", *Journal of Quantum Electronics*, **25**, Number 4, pp696-704, April 1989.
- [03] K Tateoka, H Naito, M Kume, K Hamada, H Shimizu, M Kazumura and I Teramoto, "A High-Power GaAlAs Superluminescent Diode with an Antireflective Window Structure", *Journal of Quantum Electronics*, **27**, Number 6, pp1568-1573, June 1991.
- [04] B D Patterson, J E Epler, B Graf, H W Lehmann and H C Sigg, "A Superluminescent Diode at 1.3 μ m with Very Low Spectral Modulation", *Journal of Quantum Electronics*, **30**, Number 3, pp703-712, March 1994.
- [05] A T Semenov, V R Shidlovski, S A Safin, V P Konyaev and M V Zverkov, "Superluminescent Diodes for Visible (670nm) Spectral Range Based on AlGaInP/GaInP Heterostructures with Tapered Grounded Absorber", *Electronics Letters*, **29**, Number 6, pp530-532, March 1993.
- [06] D Huang, E A Swanson, C P Lin, J S Schuman, W G Stinson, W Chang, M R Hee, T Flotte, K Gregory, C A Puliafito and J G Fujimoto, "Optical Coherence Tomography", *Science*, **254**, Number 5035, pp1178-1181, November 1991.
- [07] A F Fercher, W Drexler, C K Hitzenberger and T Lasser, "Optical Coherence Tomography - Principles and Applications", *Reports on Progress in Physics*, **66**, Number 2, pp 239-303, February 2003.
- [08] J M Schmitt, "Optical Coherence Tomography (OCT) - A Review", *IEEE Journal of Selected Topics in Quantum Electronics*, **5**, Number 4, pp1205-1215, August 1999.
- [09] A D Aguirre, P Hsiung, T H Ko, I Hartl and J G Fujimoto, "High-Resolution Optical Coherence Microscopy for High-Speed, in vivo Cellular Imaging," *Optics Letters*, **28**, Number 21, pp2064-2066, November 2003.

- [10] J A Izatt, M D Kulkarni, H S Wang, K Kobayashi and M V Sivak Jr., "Optical Coherence Tomography and Microscopy in Gastrointestinal Tissues", *Journal of Selected Topics in Quantum Electronics*, **2**, Number 4, pp1017-1028, December 1996.
- [11] S Maliszewska and M Wojtkowski, "Broadband Blue Light for Optical Coherence Microscopy", *Photonics Letters of Poland*, **3**, Number 4, pp138-140, December 2011.
- [12] T P Lee, C A Burrus Jr and B I Miller, "A Stripe Geometry Double-Heterostructure Amplified-Spontaneous-Emission (Superluminescent) Diode", *Journal of Quantum Electronics*, **9**, Number 8, pp820-828, August 1973.
- [13] G A Alphonse, D B Gilbert, M G Harvey and M Ettenberg, "High-Power Superluminescent Diodes", *Journal of Quantum Electronics*, **24**, Number 12, pp2454-2457, December 1988.
- [14] P D L Judson, K M Groom, D T D Childs, M Hopkinson and R A Hogg, "Multi-Section Quantum Dot Superluminescent Diodes for Spectral Shape Engineering", *IET Optoelectronics*, **3**, Number 2, pp100-104, November 2008.
- [15] R A Hogg, P D L Greenwood, D T D Childs, N Krstajic, K Kennedy, K M Groom, M Hugues, M Hopkinson, L E Smith, S J Matcher, M Bonesi, S Macneil and R Smallwood, "GaAs Based Quantum Dot Superluminescent Diodes for Optical Coherence Tomography of Skin Tissue", *International Conference on Computers and Devices for Communication*, pp1-6, December 2009.
- [16] I Middlemast, J Sarma and S Yunus, "High Power Tapered Superluminescent Diodes Using Novel Etched Deflectors", *Electronics Letters*, **33**, Number 10, pp903-990, March 1997.
- [17] H Shibata, N Ozaki, T Yasuda, S Ohkouchi, N Ikeda, H Ohsato, E Watanabe, Y Sugimoto, K Furuki, K Miyaji and R A Hogg, "Imaging of Spectral-domain Optical Coherence Tomography Using a Superluminescent Diode Based on InAs Quantum Dots Emitting a Broadband Spectrum with a Gaussian-like Shape", *Japanese Journal of Applied Physics*, **54**, pp04DG07-1-5, March 2015.
- [18] E Feltin, A Castiglia, G Cosendey, L Sulmoni, J F Carlin, N Grandjean, Rossetti, J Dorsaz, V Laino, M Duelk and C Velez, "Broadband Blue Superluminescent Light-Emitting Diodes Based on GaN", *Applied Physics Letters*, **95**, pp081107-1-3, August 2009.
- [19] M Rossetti, J Dorsaz, R Rezzonico, M Duelk, C Velez, E Feltin, A Castiglia, G Cosendey, J F Carlin and N Grandjean, "High Power Blue-Violet Superluminescent

- Light Emitting Diodes with InGaN Quantum Wells", *Applied Physics Express*, **3**, pp061002-1-3, 2010.
- [20] K Holc, L Marona, R Czernecki, M Bockowski, T Suski, S Najda and P Perlin, "Temperature Dependence of Superluminescence in InGaN-Based Superluminescent Light Emitting Diode Structures", *Journal of Applied Physics*, **108**, pp013110-1-4, 2010.
- [21] F Kopp, T Lermer, C Eichler and U Strauss, "Cyan Superluminescent Light-Emitting Diode Based on InGaN Quantum Wells", *Applied Physics Express*, **5**, pp082105, 2012.
- [22] U T Schwarz, F Kopp, T Weig, C Eichler and U Strauss, "Superluminescent Light Emitting Diodes of 100mW Output Power for Pico-Projection", *Conference on Lasers and Electro-Optics Pacific Rim (CLEO-PR)*, pp1-2, June 2013.
- [23] F Kopp, "Superluminescent LED for Focus-Free Handheld Projection", *SPIE Newsroom*, 10.1117/2.1201302.004686, March 2013.
- [24] F Kopp, C Eichler, A Lell, S Tautz, J Ristic, B Stojetz, C Hoss, T Weig, U T Schwarz and U Strauss, "Blue Superluminescent Light-Emitting Diodes with Output Power Above 100mW for Picoprojection", *Japanese Journal of Applied Physics*, **52**, pp08JH07-1-5, 2013.
- [25] A Kafar, S Stanczyk, S Grzanka, R Czernecki, M Leszczynski, T Suski and P Perlin, "Cavity Suppression in Nitride Based Superluminescent Diodes", *Journal of Applied Physics*, **111**, pp083106-1-6, 2012.
- [26] A Kafar, S Stanczyk, G Targowski, T Oto, I Makarowa, P Wisniewski, T Suski and P Perlin, "High-Optical-Power InGaN Superluminescent Diodes with "j-shape" Waveguide", *Applied Physics Express*, **6**, pp092102-1-4, 2013.
- [27] T Takeuchi, S Sota, M Katsuragawa, M Komori, H Takeuchi, H Amano and I Akasaki, "Quantum-Confined Stark Effect due to Piezoelectric Fields in GaInN Strained Quantum Wells", *Japanese Journal of Applied Physics*, **36**, pp382-385, February 1997.
- [28] A S Pabla, J Woodhead, E A Khoo, R Grey, J P R David and G J Rees, "Partial Screening of Internal Electric Fields in Strained Piezoelectric Quantum Well Lasers: Implications for Optoelectronic Integration", *Applied Physics Letters*, Volume 68, pp1595-1597, January 1996.
- [29] R A Hogg, T A Fisher, A R K Wilcox, D M Whittaker, M S Skolnick, D J Mowbray, J P R David, A S Pabla, G J Rees, R Grey, J Woodhead, J L Sanchez-Rojas, G Hill, M A Pate and P N Robson, "Piezoelectric-field Effects on Transition Energies, Oscillator Strengths, and Level Widths in (111)B-grown (In,Ga)As/GaAs Multiple Quantum Wells", *Physical Review B*, **48**, pp8491, September 1993.

- [30] T Takeuchi, C Wetzel, S Yamaguchi, H Sakai, H Amano and I Akasaki, "Determination of Piezoelectric Fields in Strained GaInN Quantum Wells Using the Quantum-Confined Stark Effect", *Applied Physics Letters*, 73, Number 12, pp1691-1693, September 1998.
- [31] G R Goldberg, D-H Kim, R J E Taylor, D T D Childs, P Ivanov, N Ozaki, K L Kennedy, K Groom, Y Harada and R A Hogg, "Bandwidth Enhancement in an InGaN/GaN three-section superluminescent diode for optical coherence tomography", *Applied Physics Letters*, **117**, pp061106-1-5, August 2020.
- [32] N S K Kwong, K Y Lau, N Bar-Chaim, I Ury and K J Lee, "High-Power, High Efficiency Window Buried Heterostructure GaAlAs Superluminescent Diode with Integrated Absorber", *Applied Physics Letters*, **51**, Number 23, pp1879-1881, December 1987.
- [33] A T Semenov, V K Batovrin, I A Garmash, V R Shidlovsky, M V Shramenko and S D Yakubovich, "(GaAl)As SQW Superluminescent Diodes with Extremely Low Coherence Length", *Electronics Letters*, **31**, Number 4, pp314-315, February 1995.
- [34] A T Semenov, V R Shidlovski, D A Jackson, R Willsch and W Ecke, "Spectral Control in Multisection AlGaAs SQW Superluminescent Diodes at 800nm", *Electronics Letters*, **32**, Number 3, pp255-256, February, 1996.
- [35] J A Izatt and M A Choma, "*Optical Coherence Tomography*," 2nd Edition. W Drexler and J G Fujimoto, Editors., Springer International Publishing, 2008, pp47-72
- [36] C Akcay, P Parrein and J P Rolland, "Estimation of Longitudinal Resolution in Optical Coherence Imaging," *Applied Optics*, Vol. 41, No. 25, pp5256-5262, Sep. 2002.
- [37] A C Akcay, J P Rolland and J M Eichenholz, "Spectral Shaping to Improve the Point Spread Function in Optical Coherence Tomography," *Optics Letters*, Vol. 28, No. 20, pp1921-1923, Oct. 2003.
- [38] S W Lee, H W Jeong, B M Kim, Y C Ahn, W Jung and Z Chen, "Optimization for Axial Resolution, Depth Range, and Sensitivity of Spectral Domain Optical Coherence Tomography at 1.3 μ m", *Journal of the Korean Physical Society*, Vol. 55, No.6, pp2354-2360, December 2009.
- [39] N Matuschek, M Rossetti, J Napierala, M Duell and C Velez, "Numerical Simulations of Blue and Green SLEDs", *IEEE Numerical Simulation of Optoelectronic Devices*, pp189-190, October 2011.
- [40] Nichia, "Violet Laser Diode", NDV4316 datasheet, January 2013.

- [41] B W Hakki and T L Paoli, "Gain Spectra in GaAs Double-Heterostructure Injection Lasers", *Journal of Applied Physics*, **46**, Number 3, pp1299-1306, March 1975.
- [42] P Blood, G M Lewis, P M Snowton, H Summers, J Thomson and J Lutti, "Characterization of Semiconductor Laser Gain Media by the Segmented Contact Method", *Journal of Selected Topics in Quantum Electronics*, **9**, Number 5, pp1275-1282, October 2003.

Chapter Five - Summary and Further Work

5.1 Summary

As discussed in Chapter Three section 3.10, devices with ridge widths of $5\mu\text{m}$ and $10\mu\text{m}$ were investigated throughout Chapter Three, although an initial characterisation was carried out on a $15\mu\text{m}$ wide ridge. This was due to the current source being unable to supply currents above 3A , equivalent to current densities above $7.6\text{kA}/\text{cm}^2$ through the $15\mu\text{m}$ wide ridge, or voltages above 10V [01]. As discussed and from Equation 3-2, as well as increasing the length of the waveguide, increasing its width should also give rise to superluminescent light emitting diodes (SLEDs) with higher powers [02] if the effect of self-heating can be overcome. With a larger active area, more absorption and spontaneous emission should take place, which could give rise to a wider bandwidth.

Described further in Chapter Three section 3.3, which details the fabrication method used for the devices in Chapters Three and Four, the SLEDs were etched through the active region. Shallower etching which terminates above the active region offers lower loss, and therefore higher gain, but lowers the amount of spontaneous emission captured by the waveguide. As discussed in Chapter One sections 1.3, 1.4, and 1.9, SLED operation relies on amplified spontaneous emission, designed to have a high single, or at most a double, pass through the waveguide [03]. However, a shallow-etched SLED offers a lower reflectivity, thereby reducing the optical feedback, and making this approach worthy of examination.

As discussed in Chapter Four section 4.10, simulation of a SLED output power and spectrum requires a knowledge and understanding of a broad range of material and device parameters, such as the gain and spontaneous emission spectra as a function of current, both as a function of temperature. For III-nitride materials like gallium nitride (GaN), the effect of the in-built piezoelectric fields [04-06], also needs to be considered. Although some simulation of GaN

SLEDs has been reported by Matuschek *et al.*, their model was seemingly produced alongside experimentation of well-understood devices, which informed their model of some of the aforementioned parameters [07]. The devices analysed in Chapter Two section 2.3 could be used to provide some of these parameters, for example the optical output power as a function of current density, as those devices tested were all shown to have a similar performance in good agreement with their datasheet [08].

However, some parameters required for the simulation are not as easily measured. As the aim would be to accurately model a multi-section GaN SLED, the self-heating effects with drive current would need to be known, both within each section and longitudinally along the waveguide. With the inhomogeneity of the quantum well (QW) needing to be accommodated this cannot be done *ab initio* and could not be simply extracted from the model. If the adopted approach was to measure the self-heating effects experimentally and then use the results to inform the simulation, as the number of sections increases the setup becomes ever more complex. Each section of the SLED would need access for a temperature probe, while also providing enough isolation from the adjacent temperature probes to prevent any influence on the reading.

One possible simplification is that the Hakki-Paoli method of gain measurement allows the cavity temperature change to be calculated [09], but this cannot be applied longitudinally to determine the temperature of sections when they are being independently driven at different current densities. Additionally, with the wide span of current densities required to perform these measurements, the Hakki-Paoli method would be unlikely to be appropriate across the whole range. For low current densities, the segmented contact method of gain measurement should be considered [10]; however, at higher current densities, Hakki-Paoli would be the preferred method to use [09]. The divergent device types required for characterisation, and additional spatial thermal characterisation of the device makes the collection of a suitable dataset time consuming.

All these factors make simulation of the multi-section SLED highly challenging, and almost require an experimental approach in tandem with simulation for success [07].

If an empirical approach is required, a finer set of drive conditions is essential, with more active contacts allowing for greater tunability. Machine learning could then be adopted to discover the optimal drive conditions for the device. An aspect not explored to date is the effect of using a reverse bias on the absorber section, and this is worthy of further work.

5.2 Further Work

With the vision of achieving a 1 μm axial resolution, a $\sim 50\text{nm}$ spectral bandwidth is required. Throughout this thesis, research has been deliberately limited to device design alone. This means there has not been any modification of, or considerable investigation into, changes to the epitaxy. Implementing understanding gained through this work – biased absorber, ridge width and depth modifications, more contacts, finer tuning of contacts *etc.*, – is not expected to make a further two-fold increase in spectral bandwidth. At the conclusion of my work, I feel it now timely to consider including such development work in future research.

Dorsaz *et al.*, disclose the merits of removing the aluminium gallium nitride (AlGaN) layers [11], and Lee *et al.*, report on the deposition of metal nanoparticles which create localised surface plasmons, leading to enhanced device performance [12]. For blue devices both approaches have been shown to increase efficiency. The doping process during the growth stage could also be examined, with a view to producing QWs that operate at different wavelengths [13]. Continuing this line of inquiry, quantum dots (QDs) could be incorporated, either in place of the QWs or in conjunction with them [14] – doing so could help to broaden device bandwidths if the emission originating from each QW was optimally selected so as to encourage constructive interference on the overall emission from the SLED. Sarzynski *et al.*, have demonstrated promising results by varying the indium content in devices in the growth plane, in addition to the growth direction as is more well-known. This was achieved through adjusting the substrate angle during deposition and selective patterning and a $\sim 5\text{nm}$ shift in central wavelength was observed. Selective area growth, where QW thickness and composition can be modulated, for example indium and/or aluminium content, should allow $\sim 100\text{nm}$ of tuning [15].

One or more of these techniques could be used in tandem with the continued development and improvement of SLED device designs to enhance the bandwidth. Chapter Four discussed the prospective advantages for GaN SLEDs if multi-section device designs demonstrated on gallium arsenide can be realised [16,17]. For example, Ohno *et al.*, has shown the benefit of using a flared, or trumpet, waveguide as a way of reducing gain saturation and increasing optical output power at the front of the GaN SLED [18], but another application could be towards the rear of the SLED to collect spontaneous emission for it to be amplified along the waveguide [19]. GaN SLEDs with curved waveguides have been previously reported, but this design is typically employed to reduce optical feedback for higher power applications [20-25], as are tilted waveguides [24,26,27]. Use of curved or tilted waveguides, either along the entire waveguide or at the front of SLEDs, angles the emission and increases the difficulty coupling to devices and optical fibres. However, inclusion midway along the waveguide or in the penultimate section could overcome this disadvantage while preventing the establishment of optical modes [28].

That device temperature fluctuates as a function of current density has been discussed in Chapter Four section 4.10 and reiterated in this chapter in section 5.1, however this poses difficulties in the thermal management of the device. Another option is to integrate heaters along the SLED, that can be tuned in a similar manner to the current densities of each section to optimise bandwidth.

References

- [01] ILX Lightwave, "User's Guide - Pulsed Current Source LDP - 3840B", June 2015.
- [02] G A Alphonse, D B Gilbert, M G Harvey and M Ettenberg, "High-Power Superluminescent Diodes", *Journal of Quantum Electronics*, **24**, Number 12, pp2454-2457, December 1988.
- [03] M Rossetti, J Napierala, N Matuschek, U Achatz, M Duelk, C Velez, A Castiglia, N Grandjean, J Dorsaz and E Feltn, "Superluminescent Light Emitting Diodes – the Best Out of Two Worlds", *Proceedings of SPIE*, Volume 8252, February 2012.
- [04] A S Pabla, J Woodhead, E A Khoo, R Grey, J P R David and G J Rees, "Partial Screening of Internal Electric Fields in Strained Piezoelectric Quantum Well Lasers: Implications for Optoelectronic Integration", *Applied Physics Letters*, Volume 68, pp1595-1597, January 1996.
- [05] T Takeuchi, S Sota, M Katsuragawa, M Komori, H Takeuchi, H Amano and I Akasaki, "Quantum-Confined Stark Effect due to Piezoelectric Fields in GaInN Strained Quantum Wells", *Japanese Journal of Applied Physics*, **36**, pp382-385, February 1997.
- [06] T Takeuchi, C Wetzel, S Yamaguchi, H Sakai, H Amano and I Akasaki, "Determination of Piezoelectric Fields in Strained GaInN Quantum Wells Using the Quantum-Confined Stark Effect", *Applied Physics Letters*, **73**, Number 12, pp1691-1693, September 1998.
- [07] N Matuschek, M Rossetti, J Napierala, M Duelk and C Velez, "Numerical Simulations of Blue and Green SLEDs", *IEEE Numerical Simulation of Optoelectronic Devices*, pp189-190, October 2011.
- [08] Nichia, "Violet Laser Diode", NDV4316 datasheet, January 2013.
- [09] B W Hakki and T L Paoli, "Gain Spectra in GaAs Double-Heterostructure Injection Lasers", *Journal of Applied Physics*, **46**, Number 3, pp1299-1306, March 1975.
- [10] P Blood, G M Lewis, P M Snowton, H Summers, J Thomson and J Lutti, "Characterization of Semiconductor Laser Gain Media by the Segmented Contact Method", *Journal of Selected Topics in Quantum Electronics*, **9**, Number 5, pp1275-1282, October 2003.

- [11] J Dorsaz, A Castiglia, G Cosendey, E Feltin, M Rossetti, M Duellk, C Velez, J-F Carlin and N Grandjean, "AlGaIn-Free Blue III-Nitride Laser Diodes Grown on c-Plane GaN Substrates", *Applied Physics Express*, **3**, pp092101-1-092102-3, September 2010.
- [12] I-H Lee, L-W Jang and A Y Polyakov, "Performance Enhancement of GaN-based Light Emitting Diodes by the Interaction with Localized Surface Plasmons", *Nano Energy*, **13**, pp140-173, February 2015.
- [13] J K Sheu and G C Chi, "The Doping Process and Dopant Characteristics of GaN", *Journal of Physics: Condensed Matter*, **14**, ppR657-R702, May 2002.
- [14] K Tachibana, T Someya and Y Arakawa, "Nanometer-scale InGaIn Self-Assembled Quantum Dots Grown by Metalorganic Chemical Vapor Deposition", *Applied Physics Letters*, **74**, Number 3, pp383-385, January 1999.
- [15] M Sarzynski, T Suski, G Staszczak, A Khachapuridze, J Z Domagala, R Czernecki, J Plesiewicz, J Pawlowska, S P Najda, M Bockowski, P Perlin and M Leszczynski, "Lateral Control of Indium Content and Wavelength of III-Nitride Diode Lasers by Means of GaN Substrate Patterning", *Applied Physics Express*, **5**, pp021001-1-021001-3, January 2012.
- [16] P D L Judson, K M Groom, D T D Childs, M Hopkinson and R A Hogg, "Multi-Section Quantum Dot Superluminescent Diodes for Spectral Shape Engineering", *IET Optoelectronics*, **3**, Number 2, pp100-104, November 2008.
- [17] R A Hogg, P D L Greenwood, D T D Childs, N Krstajic, K Kennedy, K M Groom, M Hugues, M Hopkinson, L E Smith, S J Matcher, M Bonesi, S Macneil and R Smallwood, "GaAs Based Quantum Dot Superluminescent Diodes for Optical Coherence Tomography of Skin Tissue", *International Conference on Computers and Devices for Communication*, pp1-6, December 2009.
- [18] H Ohno, K Orita, M Kawaguchi, K Yamanaka and S Takigawa, "200mW GaN-Based Superluminescent Diode with a Novel Waveguide Structure", *IEEE Photonics Conference*, pp505-506, October 2011.
- [19] A T Semenov, V R Shidlovski, S A Safin, V P Konyaev and M V Zverkov, "Superluminescent Diodes for Visible (670nm) Spectral Range Based on AlGaInP/GaInP Heterostructures with Tapered Grounded Absorber", *Electronics Letters*, **29**, Number 6, pp530-532, March 1993.
- [20] F Kopp, T Lerner, C Eichler and U Strauss, "Cyan Superluminescent Light-Emitting Diode Based on InGaIn Quantum Wells", *Applied Physics Express*, **5**, pp082105-1-3, 2012.

- [21] U T Schwarz, F Kopp, T Weig, C Eichler and U Strauss, "Superluminescent Light Emitting Diodes of 100mW Output Power for Pico-Projection", Conference on Lasers and Electro-Optics Pacific Rim (CLEO-PR), pp1-2, June 2013.
- [22] F Kopp, "Superluminescent LED for Focus-Free Handheld Projection", SPIE Newsroom, 10.1117/2.1201302.004686, March 2013.
- [23] F Kopp, C Eichler, A Lell, S Tautz, J Ristic, B Stojetz, C Hoss, T Weig, U T Schwarz and U Strauss, "Blue Superluminescent Light-Emitting Diodes with Output Power Above 100mW for Picoprojection", Japanese Journal of Applied Physics, **52**, pp08JH07-1-5, 2013.
- [24] A Kafar, S Stanczyk, S Grzanka, R Czernecki, M Leszczynski, T Suski and P Perlin, "Cavity Suppression in Nitride Based Superluminescent Diodes", Journal of Applied Physics, **111**, pp083106-1-6, 2012.
- [25] A Kafar, S Stanczyk, G Targowski, T Oto, I Makarowa, P Wisinieski, T Suski and P Perlin, "High-Optical-Power InGaN Superluminescent Diodes with "j-shape" Waveguide", Applied Physics Express, **6**, pp092102-1-4, 2013.
- [26] E Feltin, A Castiglia, G Cosendey, L Sulmoni, J F Carlin, N Grandjean, Rossetti, J Dorsaz, V Laino, M Duelk and C Velez, "Broadband Blue Superluminescent Light-Emitting Diodes Based on GaN", Applied Physics Letters, **95**, pp081107-1-3, August 2009.
- [27] K Holc, L Marona, R Czernecki, M Bockowski, T Suski, S Najda and P Perlin, "Temperature Dependence of Superluminescence in InGaN-Based Superluminescent Light Emitting Diode Structures", Journal of Applied Physics, **108**, pp013110-1-4, 2010.
- [28] H Nagai, Y Noguchi, S Sudo, "High-Power, High-Efficiency 1.3 μ m Superluminescent Diode with a Buried Bent Absorbing Guide Structure", Applied Physics Letters, **54**, pp1719-1721, May 1989.